Static structure and dynamical structural changes of nanoparticles using XFEL pulses

Dissertation

Department of Physics, Graduate School of Science
Kyoto University

Toshiyuki Nishiyama

March 2020

Abstract

The advent of light sources has realized the availability of intense and ultrashort (∼10 femtoseconds) laser pulses in the wide wavelength regime ranging from THz to hard X-ray. Femtosecond laser pulses have opened up new research fields of ultrafast electronic and structural dynamics in light–matter interaction. Noble gas clusters are model systems for investigating light–matter interaction due to their characteristics of an isolated many-body system. It has been reported that a cluster exposed to intense laser pulses is highly ionized and can form a nanoscale high-dense plasma, nanoplasma. Elucidation of the mechanism of nanoplasma formation and corruption is important for the understanding of light–matter interaction, and numerous researches of nanoplasma have been conducted. Structure is a fundamental property of a matter and the static structure and structural changes of a sample under light fields give insight into light–matter interaction. In the preceding works, almost all information on nanoplasma has been deduced from ion and electron spectroscopy, and the structural dynamic in nanoplasma is discussed indirectly with information on those measurements.

X-ray free-electron laser (XFEL) sources recently developed provide intense and ultrashort X-ray pulses, which enable investigation of the structure of nanoscale samples in the particle-by-particle regime. XFEL pulses also allow imaging of the structural dynamics with high spatial and temporal resolutions. The combination of the shot-by-shot imaging technique and other spectroscopies is expected to realize the study of light–matter interaction where characteristics of single targets and the intensity of the incident pulses are controlled/specified. Recent studies using this scheme have revealed unexpected structural dynamics in nanoplasma, however available information on structural changes in nanoplasma is still limited. In this work, two experiments were carried out at the SPring-8 Ångstrom Compact free-electron LAser (SACLA) to establish the size- and structure-selective evaluation scheme at SACLA and to investigate atomic-scale structural changes in nanoplasma.

In the first experiment, sub-micron xenon (Xe) clusters were irradiated by XFEL pulses (5.5 keV) with the peak fluence of 16 μJ/μm^2 and diffraction images from the clusters were recorded in coincidence with fluorescence and ion signals for each FEL shot. The FEL fluence and cluster radii extracted from each diffraction image had a clear correlation with the fluorescence and ion spectra, which showed the validity of the size- and structure-selective evaluation scheme by using the pre-

sented experimental setup.

In the second experiment, an intense near-infrared (NIR, 1.55 eV) pump laser pulse with the intensity of 4×10^{16} W/cm^2 heated a single nanoscale Xe cluster and a XFEL pulse (11 keV) with the intensity of 4×10^{17} W/cm^2 probed the state of the resulting nanoplasma. The time-resolved signals of Bragg reflection from the nanoclusters showed that the crystalline order in a Xe cluster disappears from its surface with maintaining the crystalline order of its inner core in nanoplasma transition driven by the irradiation of a NIR pulse within a few hundred femtoseconds and that the observed local disordering in nanoplasma is governed by plasma sound speed.

Contents

List of Figures

List of Tables

Chapter 1

Introduction

Since the discovery of X-rays at the end of the 19th-century [1], the fundamental organization of matter has been explored much more profoundly by using the X-ray diffraction techniques. By Laue's and Bragg's contributions, X-rays have also enabled us to understand the fundamental aspects of atoms and crystals [2, 3]. On the other hand, the progressive development of laser technology over the last decades has enabled to explore the characteristics and timescales of dynamics in various chemical/physical processes. Recent progress in free-electron lasers (FELs) and high-order harmonic generation (HHG) lasers allows us to study with shorter wavelength lasers up to the X-ray spectral regime. For the sake of the pulse duration getting shorter and the intensity higher, recent laser pulses allow for coincident analyses of structure and properties which combine diffraction and spectroscopies, and new research fields such as femtochemistry [4] and attosecond science [5] have opened up.

The advent of short-wavelength FELs has enabled to study the structure and dynamics of various forms of matter ranging from atoms [6–9] and molecules [10–13] to condensed matter [14–16]. FELs deliver highly intense and ultrashort pulses in the wide spectral regime from ultraviolet (UV) to hard X-ray [17–19]. Especially, X-ray free-electron laser (XFEL) sources have provided new opportunities to study the structure of single particles with the femtosecond (fs) time resolution and the atomic spatial resolution, based on the diffraction-before-destruction scheme [20]. Fig. 1.1 shows the results of a simulation on the temporal development of the structure of a protein induced by a single X-ray (12 keV) pulse. The internal structure of the sample remains during the irradiation of the X-ray pulse when a single X-ray pulse with a duration of a few fs is introduced. This simulation shows the validity of the diffraction-before-destruction scheme by the ultrashort X-ray pulses. Intense and short X-ray pulses delivered from XFEL sources, therefore, enable investigations of the structure of nanoscale samples and biomolecules [21–25] in the particle-by-particle scheme. The diffraction-before-destruction scheme also allows for observation of transient changes in the structure of a sample in its highly excited state, and the study of ultrafast dynamics in laser–matter interaction by using this scheme has become an active field.

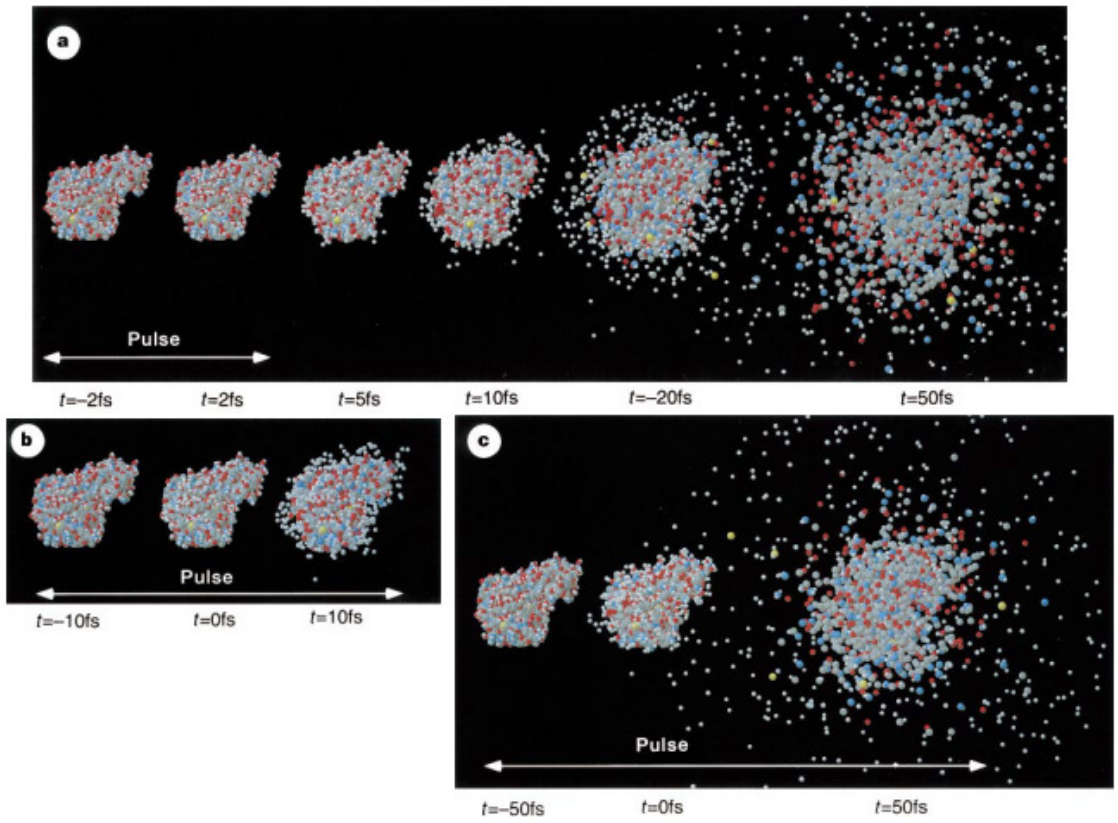

Figure 1.1: Simulative snapshots of the atomic-scale corruption of a protein sample under a single hard X-ray laser pulse. The components of the target protein quickly start to disintegrate each other under the X-ray irradiation but the structure remains in a case where the incident X-ray pulse has a duration of a few femtoseconds. This result shows that the pristine structure of the target can be taken by using ultrashort X-ray pulses before destruction. From [20]. Reprinted with permission from Nature Publishing Group.

While XFEL pulses opened the opportunities for taking snapshots of single particles, chemical/physical processes in a matter under an intense laser field in the X-ray spectral regime have also been investigated. For the study of the fundamental aspects of laser–matter interaction, atomic clusters have been regarded as simple models. Especially rare gas clusters are often used due to their characteristics. First, they can be easily generated by adiabatic expansion through a nozzle. Second, their size is tunable by changing the pressure and temperature. Third, they are isolated systems with bulk density. Today, the properties and responses of clusters in intense laser fields have been widely studied experimentally by using methods including charged-particle spectroscopy [26–40], fluorescence spectroscopy [41, 42], and X-ray diffraction [43–50], as well as theoretically [51–56].

Early experimental studies of laser–cluster interaction using FELs started with ion spectrometry. In the first study carried out at the Free-Electron Laser in Hamburg (FLASH) [28], unexpected energetic ion emissions were observed from xenon (Xe) clusters exposed to the vacuum ultraviolet (VUV) laser pulses (12.7 eV) with the intensity up to 7×10^{13} W/cm^2. This was interpreted as that a Xe cluster got highly excited via ionization and the following heating under irradiation of the

VUV pulses and finally became a nanoscale plasma with the bulk-like electron density, often called nanoplasma, which has been intensely studied in the research field using the intense near-infrared (NIR) laser [26, 27]. This study invoked a discussion regarding the dynamics in clusters. Many works have been carried out using the ion [9, 29–32, 35] and electron [33, 34, 36, 37, 40] spectra obtained by averaging over the ensemble of FEL shots. However, recent works [57, 58] revealed that the properties of individual clusters are smeared out by the accumulation of spectra. It is because of the laser profile as well as the size distribution and structural isomers of clusters originating from the generation methods. So experimental techniques allowing for studies without such averaging are necessary for deeper insights into the laser–matter interaction.

A combination of single-shot imaging with spectroscopies has a possibility of the study of the laser–matter interaction. Single-shot imaging technique gives information on sample such as size and shape as well as the intensity of the irradiated laser pulses [43–49, 59]. This selective multispectroscopy has recently been demonstrated at the Linac Coherent Light Source (LCLS) [46] using soft X-ray FEL pulses (800 eV). Fig. 1.2(a) shows a schematic of the experimental setup and some single-shot small-angle X-ray scattering (SAXS) images from single Xe clusters and Fig. 1.2(b) shows a result of the multispectroscopic measurement with diffractive imaging. This study succeeded in observing the non-linear increase of the dominant charge state of Xe ions generated after the irradiation of a single X-ray pulse by sorting and filtering the dataset with the cluster size and the field intensity at the actual reaction point extracted from the single SAXS images. They demonstrated the effectiveness of the combination of spectroscopies with the single-shot diffractive imaging. Development of the multispectroscopic experimental apparatus in the hard X-ray spectral regime is the first topic of this thesis.

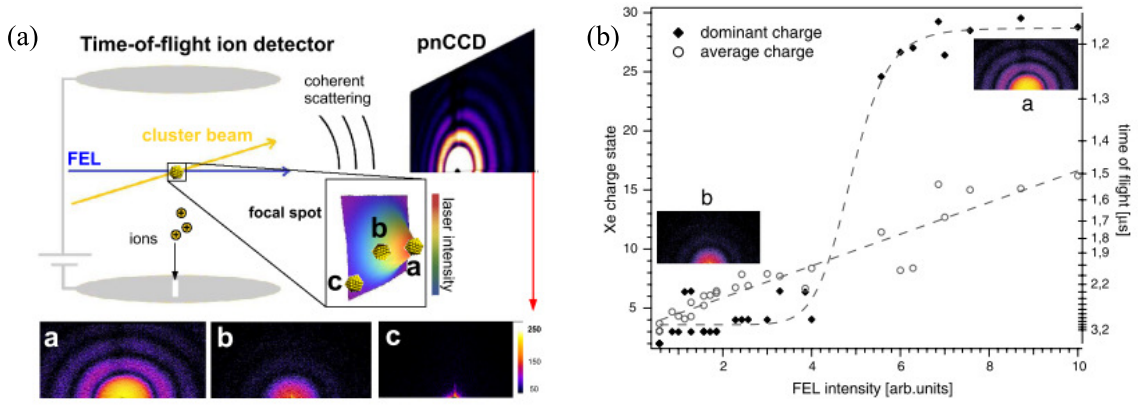

Figure 1.2: Small-angle X-ray scattering experiments on individual xenon clusters at 800-eV photon energy. (a) A schematic of the experimental setup and characteristic scattering images. From the scattering images, the cluster size and the FEL intensity at the actual reaction point could be determined. (b) FEL intensity dependence of the dominant and average charge states. The dashed lines are the guide for the eyes. From [46]. Reprinted with permission from the American Physical Society (APS).

Pump-and-probe techniques with FELs allow one to investigate the temporal development of the nanoplasma with high temporal resolution down to a few tens of fs. The firstly reported experiment pursuing the structural changes in nanoplasma expansion with diffractive imaging was conducted at LCLS [48]. Xe clusters with the radii of 15–20 nm were irradiated by single NIR laser pulses (1.55 eV) with the intensity of 2×10^{15} W/cm^2, and the diffraction patterns from the irradiated clusters were collected with soft X-ray FELs (1.55 keV). Fig. 1.3 shows the temporal evolution of the electron density of Xe clusters obtained from the collected diffraction patterns. Within a few hundred fs, the intensity of the diffraction patterns decreased from the larger momentum transfer q and the local minima of the radial profiles shifted to larger q. The loss and shift could be explained by a surface softening of the electron density of the clusters, which is predicted by a theoretical calculation with hydrogen clusters [55] in the NIR regime and that with nanoscale carbon spheres [60] in the hard X-ray regime. From these studies, one can infer that a nanoplasma generated from a Xe cluster under irradiation of the NIR laser pulses starts to expand initially from its outer layer and its inner core shrinks. The SAXS studies introduced above give an insight into nanoplasma development in terms of the changes of the electron density, but how the local structure, or the local order, in the target is changed under irradiation of intense laser pulses is unclear. To figure out this point, a pioneering work of an X-ray pump–X-ray probe study with a wide-angle X-ray scattering (WAXS) technique was carried out at LCLS [61, 62] and the authors insisted on a sudden lattice contraction in Xe nanocrystals after the XFEL irradiation. These studies have shown the effectiveness of the pump-and-probe diffractive imaging as well as the ultrafast structural changes in highly excited atomic clusters, but following questions are unsolved: how is the local order in a crystal changed under irradiation of intense laser pulses and how can it be understood?

In this work, experimental approaches combining imaging and spectroscopies were developed and the static structure and dynamic structural changes in clusters under the NIR laser field were investigated. In the first experiment, analysis of the scattering patterns determines the cluster radius and the actual XFEL fluence for each shot, with which one can select ideal data sets. The structural information on the single clusters extracted from the diffraction images gives an insight into the growth process of rare gas clusters in adiabatic expansion. By sorting the signals from the ion and fluorescence spectroscopies by the cluster size and the XFEL fluence, this work succeeded in finding clear correlations between these signals. In the second experiment, Bragg spots from single Xe clusters were collected and the ultrafast structural dynamics in nanoplasma development was discussed based on the observables obtained from the Bragg spots and ion signals. The intensity and width of the Bragg spots show a clear correlation with the delay time after the NIR irradiation, from which a non-uniform loss of the crystalline order in a Xe cluster was made clear. Including the above-described findings, this work explores answers for the following questions:

- How effective the multispectroscopy using single-shot diffractive imaging is for investigation of the structure and dynamics of nanoscale samples under intense laser pulses?

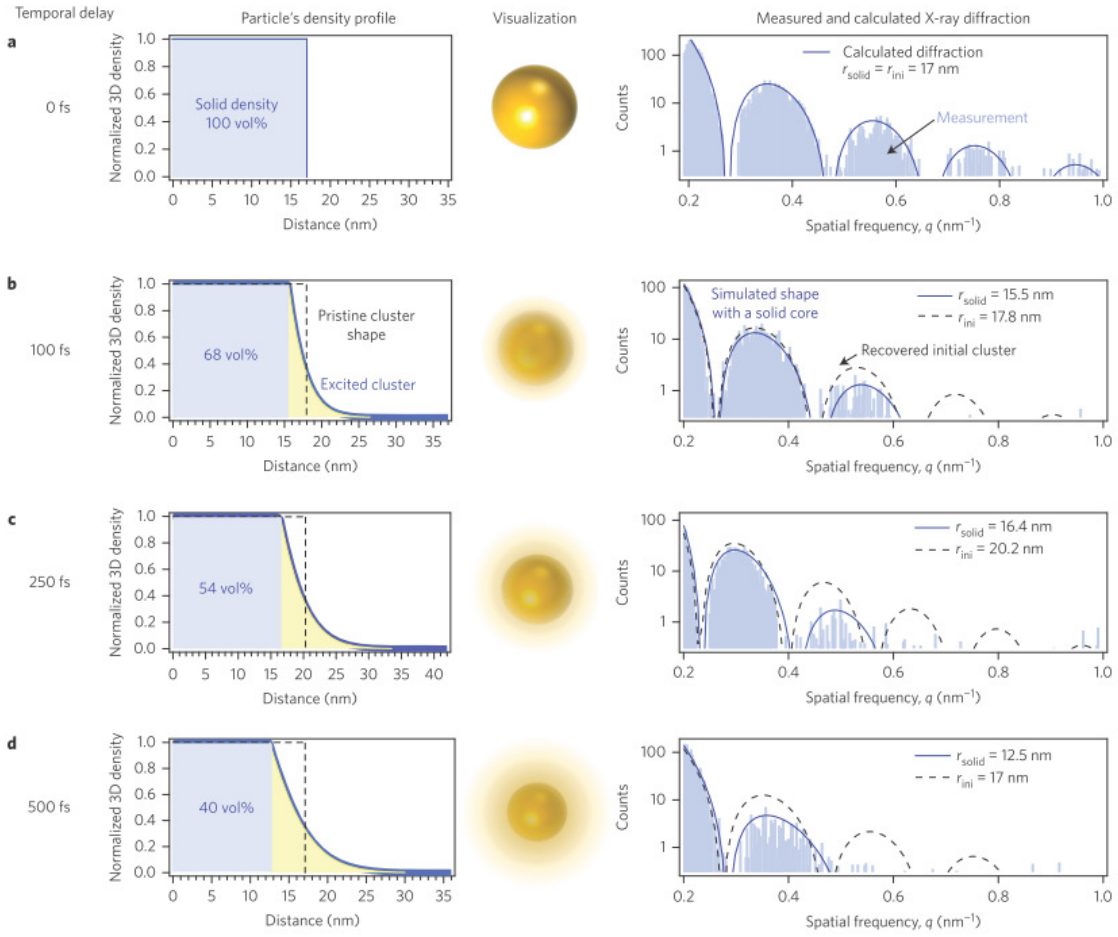

Figure 1.3: Temporal evolution of the electron density in nanoplasmas generated from Xe clusters irradiated by NIR laser pulses. The decrease of the intensity and the shift of their local minima of diffractive images shown in the right panel are well explained by a surface softening model shown in the left and center panels. From [48]. Reprinted with permission from Nature Publishing Group.

- How is the local structure of nanoscale crystals changed after the irradiation of NIR laser pulses?
- What are the time scales of the changes in the local structure of crystals induced under the NIR irradiation?

This thesis is organized as follows. Chapter 2 summarizes fundamental processes in light–matter interaction that are used throughout this work. Chapter 3 describes fundamentals in experimental aspects especially focusing on FELs and rare gas clusters. Chapter 4 presents the results of multi-spectroscopic study using single-particle coherent diffractive imaging (CDI) at SACLA. Chapter 5 presents an application of the experimental scheme developed on the basis of the knowledge from the first experiment, where the structural dynamics in nanoplasma on the atomic scale was investigated by the time-resolved diffractive imaging at SACLA. Chapter 6 finally summarizes the present work and future perspectives.

Chapter 2

Fundamental processes in light–matter interaction

This chapter summarizes the fundamental concepts of the light–matter interaction. We will focus on the processes in the optical regime and overview those in the X-ray regime. Firstly, photon scattering, absorption, and following processes by an electron and an atom are introduced. Secondly, the discussion is developed to extended objects, especially nanoscale particles and clusters. The line of the discussion in this chapter follows the books of Thompson, *X-ray data booklet* [63], Bohren and Huffman, *Absorption and scattering of light by small particles* [64], and Als-Neilsen and McMorrow, *Elements of Modern X-ray Physics* [65].

2.1 Light-electron and light-atom interaction

When a photon interacts with an atom, the photon is absorbed or scattered by one of the electrons bound to the atom. The processes after/on absorption are categorized into the followings:

- Photoexcitation: the electron goes up to the upper level of the energy state of the atom.
- Photoionization: the electron is ejected into the continuum
- Pair production: an elementary particle and its antiparticle are created (e.g. electron and positron).
- Photonuclear absorption: the nucleus of the atom absorbs the photon and another photon or neutron is emitted.

The scattering of a photon can be classified into two types in terms of the change of photon energy after interaction:

- Elastic/Coherent scattering: the photon is scattered without energy transfer to the electron.
- Inelastic/Compton scattering: the photon transfers its energy to the electron, resulting in the loss of energy of the scattered photon.

The frequency (probability) of these processes is often described as the cross section [63]. Fig. 2.1 shows photon cross sections in carbon and xenon (Xe) as functions of photon energy. As shown in both carbon and Xe, pair production and photonuclear absorption are important typically in the photon-energy range over 1 MeV [63]. Therefore, the dominant effects for the interaction with photons with a few keV energy are photoexcitation, photoionization and scattering. The following subsections describe three processes related to the main experiments of this thesis on the following order: elastic scattering, photoexcitation, and photoionization.

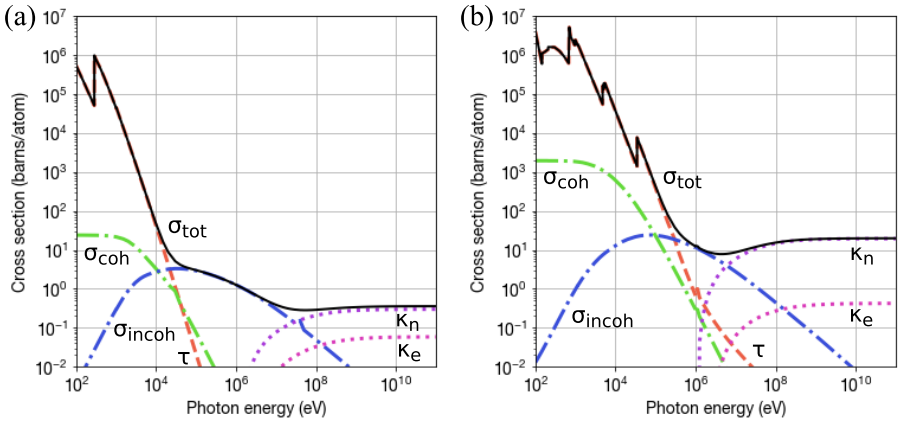

Figure 2.1: Photon cross sections in carbon (a) and xenon (b) as functions of photon energy $h\nu$. In each figure, σ_{tot}: total cross section, τ: photoeffect (photoionization + photoexcitation), σ_{coh}: coherent scattering, σ_{incoh}: incoherent scattering, κ_n, κ_e: pair production. The data set is obtained from [66] (0.1 keV $\leq h\nu \leq$ 1 MeV; used with permission from Elsevier) and [67] (1 MeV $\leq h\nu \leq$ 100 GeV; used with permission from AIP Publishing).

2.1.1 Elastic scattering

Elastic scattering by an electron/atom has been discussed not only in the classical-mechanical picture but also in the quantum-mechanical picture. Though it can be treated accurately in the quantum-mechanical picture, the elastic scattering of photon will be discussed in the classical-mechanical picture in this section because the classical approach gains a fundamental and intuitive insight into the elastic scattering by an electron or an atom.

Propagation of an electromagnetic field: starting from Maxwell's equations

It is reasonable and usual that the discussion of the propagation of an electromagnetic field starts from Maxwell's equations. Maxwell's equations consist of four fundamental laws, which are given

by the following (in MKS units) [64]:

$$\nabla \cdot \mathbf{D}(\mathbf{r},t) = \rho(\mathbf{r},t), \tag{2-1}$$

$$\nabla \cdot \mathbf{B}(\mathbf{r},t) = 0, \tag{2-2}$$

$$\nabla \times \mathbf{E}(\mathbf{r},t) = -\frac{\partial \mathbf{B}}{\partial t}(\mathbf{r},t), \tag{2-3}$$

$$\nabla \times \mathbf{H}(\mathbf{r},t) = \frac{\partial \mathbf{D}}{\partial t}(\mathbf{r},t) + \mathbf{J}(\mathbf{r},t), \tag{2-4}$$

where $\mathbf{E}$ is the electric field vector, $\mathbf{D}$ is the electric displacement vector, $\mathbf{H}$ is the magnetic field vector, $\mathbf{B}$ is the magnetic induction, $\mathbf{J}$ is the current density, and ρ is the charge density. The electric displacement $\mathbf{D}$ and the magnetic induction $\mathbf{B}$ in a material can be described as follows:

$$\mathbf{D} = \epsilon_0 \mathbf{E} + \mathbf{P}, \tag{2-5}$$

$$\mathbf{B} = \mu_0(\mathbf{H} + \mathbf{M}), \tag{2-6}$$

where $\mathbf{P}$ is the electric polarization and $\mathbf{M}$ is the magnetic polarization of a material induced by the external electromagnetic field.

No sources: planer wavefield: Consider firstly the situation where the wavefield propagates in vacuum. $\mathbf{P} \equiv \mathbf{0}$ and $\mathbf{M} \equiv \mathbf{0}$ in this situation. By combining Maxwell's equations and using the mathematical relation $\nabla \times \nabla \times \mathbf{A} = \nabla(\nabla \cdot \mathbf{A}) - \nabla^2 \mathbf{A}$ ($\mathbf{A}$ is an arbitrary vector), one can derive an extensive form of the vector wave equation for the electric field:

$$\left(\frac{\partial^2}{\partial t^2} - c^2 \nabla^2 \right) \mathbf{E}(\mathbf{r},t) = 0, \tag{2-7}$$

where c is the speed of light in vacuum and given by the following expression:

$$c = 1/\sqrt{\mu_0 \epsilon_0}.$$

In this expression, ϵ_0 and μ_0 are the permittivity and permeability in vacuum, respectively. The solution of Eq. 2-7 can be given by a planer field:

$$\mathbf{E}(\mathbf{r},t) = \mathbf{E}_0 e^{-\mathrm{i}(\mathbf{k}\cdot\mathbf{r} - \omega t)}, \tag{2-8}$$

where $\mathbf{k}$ and ω satisfy a dispersion relation $c|\mathbf{k}| = \omega$. This result simply shows that the electromagnetic field propagates in vacuum with the phase velocity $v_p = c$.

One can infer the propagation of the electromagnetic wave in a matter from the above result. When an electromagnetic field propagates in the material, its v_p is given by $1/\sqrt{\epsilon\mu}$, where ϵ and μ are the permittivity and permeability of the material, respectively. Using the ordinal expression of the refractive index $n = \sqrt{\epsilon\mu}/\sqrt{\mu_0\epsilon_0}$, v_p is equal to c/n.

The refractive index can be treated as the complex, n can be written as $n = n_1 + \mathrm{i}n_2$. Its real part (n_1) and imaginary part (n_2) are related to the phase shift and attenuation, respectively. One can see these relationships by simple consideration like the below. Consider the situation that the planar wavefield propagates through the material in the z-direction. Then the wavefield can be written by

$$\mathbf{E}(z,t) = \mathbf{E}_0 e^{-\mathrm{i}\omega(t-z/c)} e^{\mathrm{i}\omega(n_1-1)z/c} e^{-\omega n_2 z/c},$$

where the dispersion relation in the material $\omega = kv_p = kc/n$ was used. The above result shows that the wavefield after propagating the distance z is phase-shifted by $\omega(n_1 - 1)z/c$ and attenuated by $e^{-\omega n_2 z/c}$. Especially in the X-ray regime, the refractive index is slightly different from 1, so the refractive index is usually expressed as follows:

$$n = 1 - \delta + \mathrm{i}\beta. \tag{2-9}$$

Using this expression and the relation between the frequency and the wavelength, $\omega = 2\pi c/\lambda$, the wavefield discussed above is rewritten by

$$\mathbf{E}(z,t) = \mathbf{E}_0 e^{-\mathrm{i}\omega(t-z/c)} e^{-\mathrm{i}\frac{2\pi\delta}{\lambda}z} e^{-\frac{2\pi\beta}{\lambda}z}. \tag{2-10}$$

Scattering field by a moving charged particle: Secondly, consider the situation where the planer wavefields propagate in the existence of a moving particle with the charge Q. In this situation, the particle oscillates in the field and makes another electric field, which is equivalent to the scattering field of the incident planar wave. An extension of this situation is exactly one of the scattering experiments, where the incident photon pulses can be taken as planer wave pulses at the reaction points and scattered by the multi-electron system. Like the case of vacuum, the corresponding wave equation can be deduced from Maxwell's equations by using and leaving the source $\mathbf{J}$ and ρ, resulting in the following equation:

$$\left(\frac{\partial^2}{\partial t^2} - c^2\nabla^2\right)\mathbf{E}(\mathbf{r},t) = -\frac{1}{\epsilon_0}\left[\frac{\partial \mathbf{J}(\mathbf{r},t)}{\partial t} + c^2\nabla\rho(\mathbf{r},t)\right]. \tag{2-11}$$

From Eq. 2-11, the electric field by a moving charged particle can be derived as the following form:

$$\mathbf{E}(\mathbf{r},t) = \frac{Q}{4\pi\epsilon_0 c^2}\frac{\mathbf{n}\times\{\mathbf{n}\times\dot{\mathbf{v}}(\mathbf{r},t-r/c)\}}{r}, \tag{2-12}$$

where $\mathbf{n} \equiv \mathbf{r}/|\mathbf{r}|$ is the normal vector of $\mathbf{r}$ and $\dot{\mathbf{v}}$ is the acceleration of the particle. Eq. 2-12 shows that the scattered field by a moving charged particle depends on its acceleration, which can be obtained from the equation of motion.

Scattering field by a free electron

A free electron under an electromagnetic field feels the Lorentz force:

$$\mathbf{F}_{Lorentz}(\mathbf{r},t) = -e\left(\mathbf{E}(\mathbf{r},t) + \mathbf{v}(\mathbf{r},t) \times \mathbf{B}(\mathbf{r},t)\right), \tag{2-13}$$

where $\mathbf{v}$ is the velocity if the free electron. The second term of the Lorentz force is negligible under the non-relativistic condition ($|\mathbf{v}| \ll c$). Using the equation of motion $m_e\dot{\mathbf{v}} = \mathbf{F}_{Lorentz}$ (m_e is the mass of an electron), the scattering field by an electron at $\mathbf{r} = \mathbf{0}$ can be given by

$$\mathbf{E}_{free}(\mathbf{r},t) = -|\mathbf{E}| \sin\Theta \frac{e^2}{4\pi\epsilon_0 m_e c^2} \frac{e^{-i\omega\left(t-\frac{r}{c}\right)}}{r} \frac{\mathbf{k}}{|\mathbf{k}|}, \tag{2-14}$$

where Θ is the angle between the polarization direction of $\mathbf{E}$ and the scattering direction $\mathbf{k}/|\mathbf{k}|$. The first fraction part of the right side of Eq. 2-14 above is well known as the classical electron radius:

$$r_e = \frac{e^2}{4\pi\epsilon_0 m_e c^2}. \tag{2-15}$$

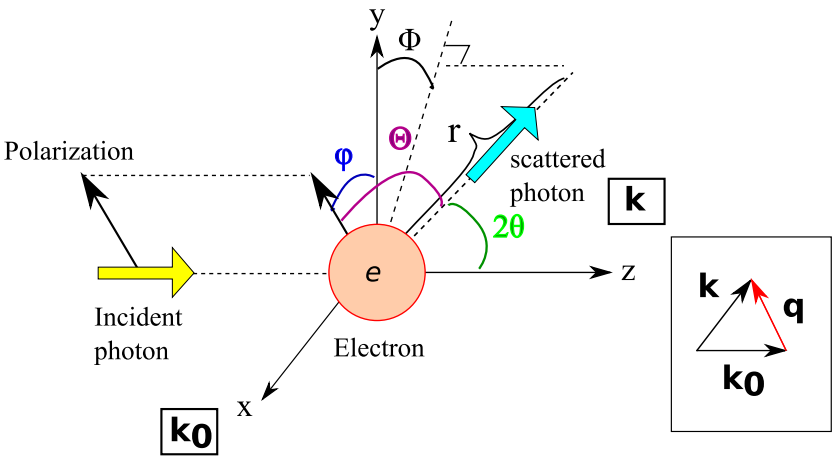

Figure 2.2: A schematic of scattering by a free electron. θ and ϕ are the azimuthal and polar angles in the polar coordinate, respectively.

Scattering field by a bound electron

An electron bound to an atom is often modeled by an oscillator, the electron oscillates around the atom with a frequency. This model is called the Lorentz oscillator model and the combination of the model and Eq. 2-12 gives insight into the scattering by an electron bound to an atom in the semi-classical picture. Assuming the atom is located on the origin of the real space, the equation of motion by the Lorentz model can be described as

$$m_e\dot{\mathbf{v}} = \mathbf{F}_{Lorentz} - m_e\gamma_{damp}\mathbf{v} - m_e\omega_{res}^2\mathbf{r}, \tag{2-16}$$

where γ_{damp} is a damping rate and ω_{res} is the oscillation frequency of the bound electron. Assuming that the external field is a plane wave $\mathbf{E} = \mathbf{E}_0 e^{-\mathrm{i}\omega t}$, the solution of Eq. 2-16 has the form $\mathbf{r} = \mathbf{r}_0 e^{-\mathrm{i}\omega t}$ and $\mathbf{r}_0$ is given by the following:

$$\mathbf{r}_0 = \frac{e\mathbf{E}_0}{m_e} \frac{1}{\omega^2 - \omega_{res}^2 + \mathrm{i}\gamma_{damp}\omega}. \tag{2-17}$$

The acceleration can be easily calculated:

$$\dot{\mathbf{v}} = -\frac{\omega^2}{\omega^2 - \omega_{res}^2 + \mathrm{i}\gamma_{damp}\omega} \mathbf{E}_0 e^{-\mathrm{i}\omega t}, \tag{2-18}$$

and the scattered field can be written as

$$\mathbf{E}_{bound}(\mathbf{r}, t) = -|\mathbf{E}_i| \sin\Theta \frac{\omega^2}{\omega^2 - \omega_{res}^2 + \mathrm{i}\gamma_{damp}\omega} \frac{r_e}{r} e^{-\mathrm{i}\omega\left(t - \frac{r}{c}\right)} \frac{\mathbf{k}}{|\mathbf{k}|}. \tag{2-19}$$

Scattering field by an atom, the atomic form factor

Scattering by an atom can be simply modeled by an extension of the Lorentz oscillator model. From this simple approximation, one can see the basic properties of scattering by an atom. In the semi-classical-mechanical picture, the electron density of an electron can be expressed as $\rho(\mathbf{r}) = \delta(\mathbf{r} - \mathbf{r}_0)$, where $\mathbf{r}_0$ is the coordinate of the electron. Then the electron density of an atom can be given by the summation:

$$\rho(\mathbf{r}, t) = \sum_{j=1}^{Z} \delta(\mathbf{r} - \mathbf{r}_j(t)), \tag{2-20}$$

where Z is the total number of electrons bound to the atom and $\mathbf{r}_j$ is the coordinate of the j-th electron. The scattered field can be expressed as the superposition of scattered fields by each electron bound to the nucleus. Scattered fields by electrons have different phases due to the different scattering points (coordinates) of each electron. The phase difference of the j-th electron can be expressed as $-\mathbf{q} \cdot \Delta\mathbf{r}_j$, where $\mathbf{q} \equiv \mathbf{k} - \mathbf{k}_0$ is the difference of the wave vector of scattered field from that of the incident field, called the scattering vector (the momentum transfer), and $\Delta\mathbf{r}_j = \mathbf{r}_j - \mathbf{r}_{atom}$ is the relative coordinate of the j-th electron to the nucleus. Including the phase difference, the scattered field by an atom is given in the following form:

$$\mathbf{E}(\mathbf{r}, t) = -|\mathbf{E}_i| \sin\Theta \left(\sum_{j=1}^{Z} \frac{\omega^2 e^{-\mathrm{i}\mathbf{q}\cdot\Delta\mathbf{r}_j}}{\omega^2 - \omega_{res,j}^2 + \mathrm{i}\gamma_{damp,j}\omega} \right) \frac{r_e}{r} e^{-\mathrm{i}\omega\left(t - \frac{r}{c}\right)} \frac{\mathbf{k}}{|\mathbf{k}|}. \tag{2-21}$$

Atomic form factor: From Eq. 2-21, one can obtain the so-called atomic form factor[1] [68]:

$$f(\mathbf{q}, \omega) = \sum_{j=1}^{Z} \frac{\omega^2 e^{-\mathrm{i}\mathbf{q}\cdot\Delta\mathbf{r}_j}}{\omega^2 - \omega_{res,j}^2 + \mathrm{i}\gamma_{damp,j}\omega}. \tag{2-22}$$

[1] Atomic form factor is often referred to as atomic scattering factor.

Using the atomic form factor, the scattered field by an atom can be also expressed as follows:

$$\mathbf{E}(\mathbf{r},t) = -|\mathbf{E}_i|\sin\Theta f(\mathbf{q},\omega)\frac{r_e}{r}e^{-\mathrm{i}\omega\left(t-\frac{r}{c}\right)}\frac{\mathbf{k}}{|\mathbf{k}|}. \tag{2-23}$$

The atomic form factor can be separated into the real and imaginary parts [65, 68]: $f(\mathbf{q},\omega) = f'(\mathbf{q},\omega) + \mathrm{i}f"(\mathbf{q},\omega)$. The atomic form factor is related to the refractive index of materials. If a material is composed of N atoms whose atomic form factors are $f_j(\mathbf{q},\omega)$, then its refractive index n can be expressed by using the forward atomic form factor $f_j(\mathbf{0},\omega)$:

$$n = 1 - \delta + \mathrm{i}\beta = 1 - \frac{r_e}{2\pi}\sum_{j=1}^{N} f_j(\mathbf{0},\omega). \tag{2-24}$$

This relation shows that the real part of the atomic form factor is related to the phase shift δ and the imaginary part is related to attenuation β.

Differential scattering cross section

The differential scattering cross section is defined by the following [65]:

$$\frac{\mathrm{d}\sigma}{\mathrm{d}\Omega}(\Omega) \equiv \frac{\text{The power of field scattered to the direction } \Omega}{\text{The power of the incident field}} = \frac{P_{scat}r^2}{P_{inc}} \tag{2-25}$$

The Poynting vector, $\mathbf{S} \equiv \mathbf{E}\times\mathbf{H}$, represents the energy flow by an electromagnetic field [64], and is useful to calculate the power of the electromagnetic field. The power of the electromagnetic field P is given by the inner product of its direction and Poynting vector: $P = \mathbf{S}\cdot\mathbf{k}/|\mathbf{k}|$. Assuming that a planer wavefield $\mathbf{E}_{inc} = |\mathbf{E}_0|e^{\mathrm{i}\mathbf{k}_0\cdot\mathbf{r}-\omega t}\mathbf{k}_0/|\mathbf{k}_0|$ is used as the incident field, which is the most popular case of the experiments using electromagnetic beam, the differential scattering cross section of a free electron is obtained by using Eq. 2-14 and has the following form:

$$\frac{\mathrm{d}\sigma}{\mathrm{d}\Omega}(\Omega) = r_e^2\sin^2\Theta. \tag{2-26}$$

Using Eq. 2-19, the differential scattering cross section of a bound electron is expressed as

$$\frac{\mathrm{d}\sigma}{\mathrm{d}\Omega}(\Omega) = r_e^2\sin^2\Theta\frac{\omega^4}{(\omega^2-\omega_{res}^2)^2+\gamma_{damp}^2\omega^2}. \tag{2-27}$$

$\sin^2\Theta$ is often called the polarization factor and can be expressed by using the polar angle and azimuthal angle (defined in Fig. 2.2):

$$\sin^2\Theta = 1 - \sin^2 2\theta\cos^2(\phi-\varphi). \tag{2-28}$$

Similarly, the differential cross section of an atom can be given by the following:

$$\frac{\mathrm{d}\sigma}{\mathrm{d}\Omega}(\Omega) = r_e^2|f(\mathbf{q},\omega)|^2\sin^2\Theta \tag{2-29}$$

The total cross section of a free electron is given by the integral of Eq. 2-26:

$$\sigma_{free} = \frac{8\pi}{3} r_e^2 \equiv \sigma_{Thomson} \tag{2-30}$$

This cross section is well known as the Thomson cross section and does not depend on the frequency of the incident field. Similarly, the total cross section of a bound electron is

$$\sigma_{bound} = \sigma_{Thomson} \frac{\omega^4}{(\omega^2 - \omega_{res}^2)^2 + \gamma_{damp}^2 \omega^2} \tag{2-31}$$

$$\rightarrow \begin{cases} \sigma_{Thomson} & (\omega \gg \omega_{res}) \\ \sigma_{Thomson} \left(\frac{\omega}{\omega_{res}}\right)^4 & (\omega \ll \omega_{res} \text{ and } \omega_{res} \gg \gamma_{damp}) \end{cases} . \tag{2-32}$$

Eq. 2-31 is strongly dependent on the frequency of the incident field. Fig. 2.3 shows the profile of Eq. 2-31. One can interpret the behavior of the cross section of a bound electron as follows:

- The cross section has its maximum peak at $\omega = \omega_{res}$ and the width of the peak is given by $\gamma_{damp}/2$.
- The cross section approaches the cross section of Thomson scattering for $\omega \gg \omega_{res}$, which suggests that electrons under a high-frequency field can be treated as free electrons.
- The cross section reduces to the cross section for Rayleigh scattering for $\omega \ll \omega_{res}$ under the condition of $\omega_{res} \gg \gamma_{damp}$.

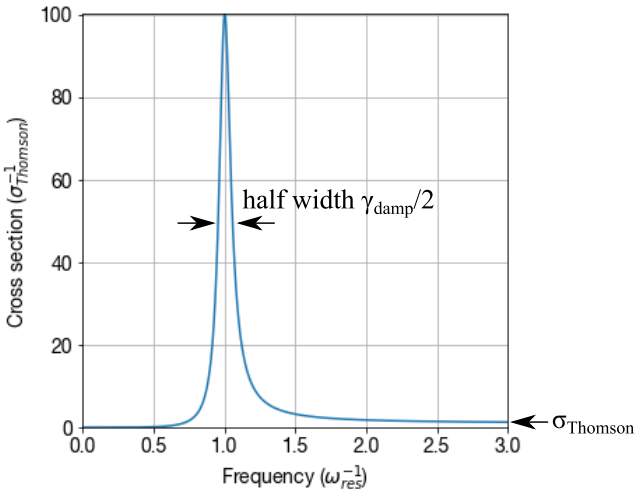

Figure 2.3: Frequency dependence of the cross section of a bound electron. The formula of the plotted curve is given by Eq. 2-31. Here γ_{damp} is assumed to be $0.1\omega_{res}$.

2.1.2 Photoexcitation, photoionization and following processes

Photoexcitation or photoionization occurs when a photon is absorbed by an atom. Photoexcitation is the phenomenon where one electron in a certain energy state goes up to the higher energy state after absorbing a photon. Photoionization is the phenomenon where one electron gain energy by absorbing a photon and goes up to the continuum state, that is, the electron is released from the bind of the atom. As shown in Fig. 2.1, the cross section of photoionization is strongly dependent on the photon energy of the absorbed photon, and this is also true of photoexcitation. In most elements, the ionization energy of the valence electrons is on the order of ten electron volts (eV), that is, a single photon in the VUV regime can ionize valence electrons. On the other hand, the ionization energy of the core electrons is on the order of a hundred eV, and the photons in the X-ray regime can ionize electrons in the core electronic shell of the atom.

When a core electron is ionized, the resulting ion has core vacancy and is not in the minimal energy state. So certain relaxation occurs in the core-vacancy ion. There are the following relaxation processes: Auger decay, Coster-Kronig decay, and fluorescence emission. These three processes of relaxation are depicted in Fig. 2.4. The energy relaxation sequentially occurs until the core-ionized ion reaches the final state (the energetically favorable state). The possibility of the occurrence of the above processes depends on elements and vacancy shells. Tab. 2.1 shows the relative yields of Coster-Kronig decay and fluorescence emission for a L-shell-vacant Xe atom [69].

Table 2.1: The relative yields of Coster-Kronig decay ($f_{i,j}$) and fluorescence emission (ω_i) for a L-shell-vacant Xe atom. Xe atom has three levels for the L shell (L_1, L_2, L_3). $f_{i,j}$ corresponds to the Coster-Kronig yield for radiationless transitions between L_i and L_j levels. Note that the sum of the relative yields for all decay processes including Auger decay is unity. From [69]. Reprinted with permission from AIP Publishing.

Type	Fluorescence			Coster-Kronig		
Symbol	ω_1	ω_2	ω_3	$f_{1,2}$	$f_{2,3}$	$f_{2,3}$
Relative yield	0.046	0.083	0.085	0.19	0.28	0.154

2.1.3 Ionization under an intense field

The recent development of laser source has given the opportunity to use laser pulses with intensities over 10^{15} W/cm^2 in experiments. These intense lasers have opened up the study of other mechanisms of ionization: field ionization and multi-photon ionization. These mechanisms are depicted in Fig. 2.6. Field ionization is a process where the atomic potential is modulated and a bound electron can escape the modulated potential via tunneling of the potential barrier or *overcomes* the barrier. The former is often called tunnel ionization (TI) and the latter barrier-suppressed ionization (BSI). An intense field causing BSI can be inferred from a simple model of the atomic potential modulated by the electric field of the laser. Consider an electron under the potential of a Q-charged ion and an

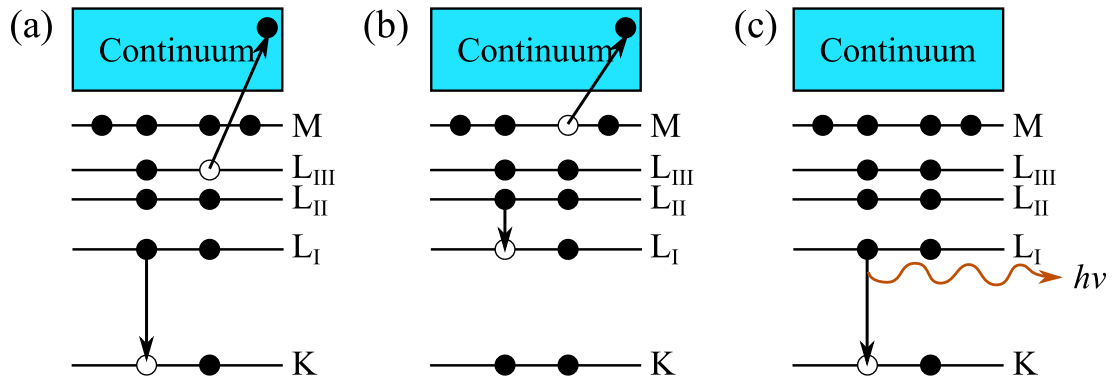

Figure 2.4: Schematics of Auger decay (a), Coster-Kronig decay (b) and fluorescence emission (c) of a core-ionized atom. In Auger decay, a core hole is filled by an electron in an upper shell and another electron in an upper shell is emitted from the ion. In Coster-Kronig decay, a core hole (e.g. L_{I}) is filled by an electron in an upper shell of the same level (e.g. L_{II}) and another electron in the further higher shell is emitted. In fluorescence emission, a core hole is filled by an electron in an upper shell and a photon (fluorescence) with the energy equivalent to the difference of energy level is emitted. After [65].

electrostatic field directed to the z-direction. The effective potential can be written by

$$U(z) = -\frac{qe^2}{4\pi\epsilon_0}\frac{1}{|z|} - eEz. \tag{2-33}$$

This potential has the local maximum as a "barrier" with the energy $U_b = -2\sqrt{qe^3E/4\pi\epsilon_0}$ at the position $z = \sqrt{qe/4\pi\epsilon_0 E}$. When this barrier gets below the binding energy, the electron can escape from the ion. A typical value of the first ionization potential is on the order of 10 eV. Hence, the threshold intensity is on the order of 10^{16} W/cm^2.

Multi-photon ionization (MPI) is a process where some photons with the photon energy below certain binding energy of an electron bound to an atom are absorbed simultaneously and the bound electron is released from the atom. The kinetic energy of the released electron can be written as

$$E_{kin} = nh\nu - E_{IP}, \tag{2-34}$$

where n and $h\nu$ are the number and the energy of the absorbed photons, respectively, and E_{IP} is the binding energy (ionization potential) of the electron. The probability of ν-photons MPI is strongly dependent on the laser intensity I and can be written by $\Gamma_\nu = \sigma_\nu I^\nu$, where σ_ν is the cross section of ν-photons MPI. Furthermore, high energy photon can ionize electrons in the inner core of an atom directly. The wavelength dependence of the dominant ionization mechanism by intense laser pulses is well summarized in Fig. 2.5.

The dominant process depends on the wavelength and the strength of the incident laser field. There is

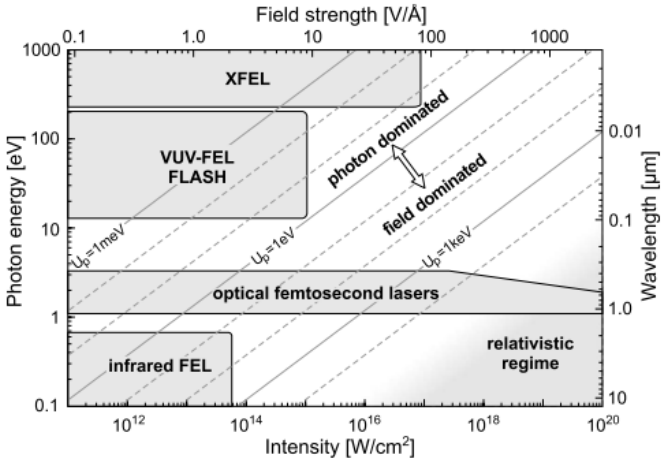

Figure 2.5: The wavelength dependence of the dominant ionization mechanism. From [70]. Reprinted with permission from APS.

a measure called the Keldysh parameter [71] often used for judging the significance of field ionization over single- or multi-photon ionization [70, 72, 73]. The Keldysh parameter γ is defined by

$$\gamma \equiv \frac{E_{IP}}{2U_p}, \tag{2-35}$$

where E_{IP} is the first ionization energy and U_p is the ponderomotive energy of the laser field defined by

$$U_p = \frac{e^2 E_0^2}{4m_e\omega^2}. \tag{2-36}$$

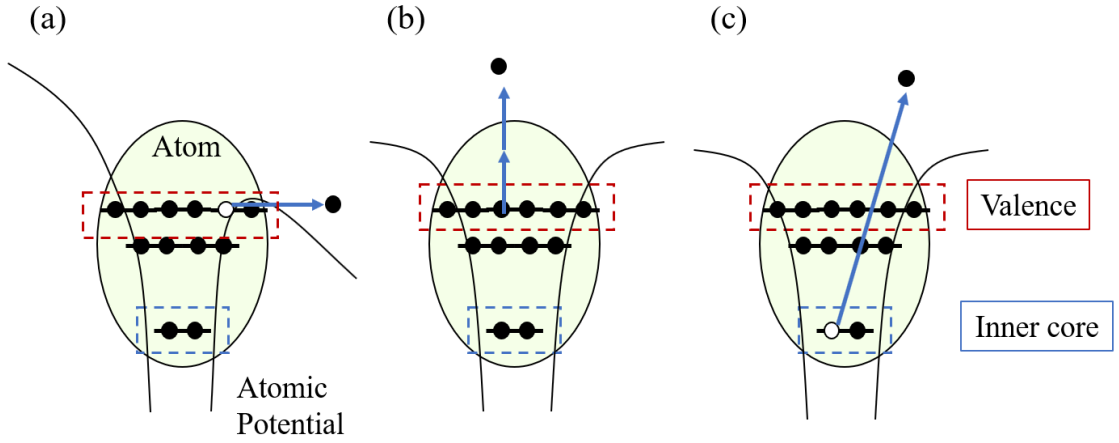

Figure 2.6: Schematics of field ionization (a), multi-photon ionization (b), and inner-core ionization (c).

2.2 Interaction of light in the X-ray regime with extended objects

Since the absorption cross section of atoms in the X-ray spectral regime is low, the absorption and multiple scattering by atoms are negligible. Under these circumstances, a simple kinetic consideration can be applied. This section focuses on X-ray scattering by extended objects, i.e. ensembles of atoms.

2.2.1 Scattering by extended objects

Photon scattering by objects can be expressed by an extensive picture of scattering by atoms. Consider the situation where a polarized photon beam with a wavelength of λ and the number density of J_0 propagates to a target composed of N atoms. The scattering wave by the target can be expressed by the superposition of scattering waves by each atom. Hence, the scattering amplitude of the target, which is an analogy of the atomic form factor, can be defined by using atomic form factors of each atom:

$$S(\mathbf{q},\omega) = \sum_j f_j(\mathbf{q},\omega)\exp(-\mathrm{i}\mathbf{q}\cdot\mathbf{r}_j), \tag{2-37}$$

where $\mathbf{r}_j$ is the relative position of the j-th atom to the center of the target. Using the scattering amplitude, the differential cross section of the target is given by

$$\frac{\mathrm{d}\sigma}{\mathrm{d}\Omega}(\Omega) = r_e^2|S(\mathbf{q},\omega)|^2\{1-\sin^2 2\theta\cos^2(\phi-\varphi)\} \tag{2-38}$$

Therefore, the number of photons scattered to the solid angle Ω can be formulated as follows:

$$N_s(\Omega) = J_0\sigma(\Omega)\mathrm{d}\Omega = J_0 r_e^2|S(\mathbf{q},\omega)|^2\{1-\sin^2 2\theta\cos^2(\phi-\varphi)\}\mathrm{d}\Omega \tag{2-39}$$

2.2.2 Small-angle X-ray scattering

In this subsection, the basic equations for small-angle X-ray scattering (SAXS) will be summarized. Fig. 2.7 shows a schematic of a SAXS experiment. An incident X-ray beam is scattered by a sample and the scattered photons are detected by a position-sensitive detector such as an imaging plate. The scattered photons construct an image reflecting on the characteristics of the sample. Typically the radial profile of the image is extracted and plotted as a function of the momentum transfer so that one can infer the overall feature of the sample from the profile.

When an incident beam with the wavelength of λ and the number density of J_0 propagates to a target, the number of scattering photons can be described by the following:

$$\begin{aligned} N_s(\Omega) &= J_0\sigma(\Omega)|S(\mathbf{q})|^2\mathrm{d}\Omega \\ &= J_0 r_e^2\{1-\sin^2 2\theta\cos^2(\phi-\varphi)\}\left|\int_{\text{target}}\mathrm{d}^3 r\rho(\mathbf{r})\exp(-\mathrm{i}\mathbf{q}\cdot\mathbf{r})\right|^2\mathrm{d}\Omega, \end{aligned} \tag{2-40}$$

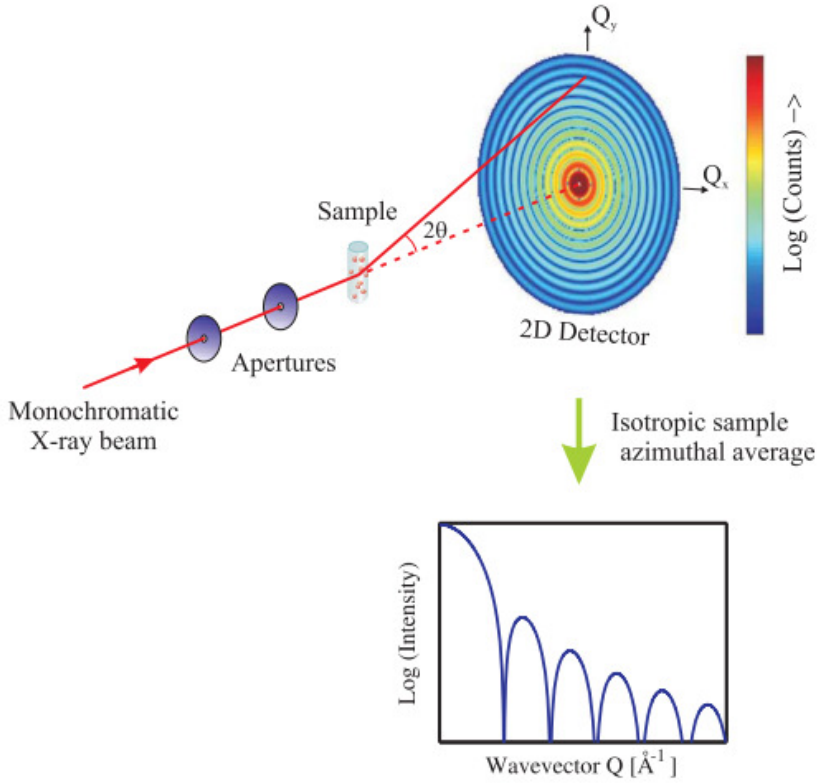

Figure 2.7: A schematic layout of a SAXS measurement. A monochromatic X-ray beam is introduced to the reaction point and photons scattered by a sample are detected by a set of detectors. Usually, a position-sensitive detector is used. The scattered photons from isotropic samples have the tendency to show a concentric pattern, and the profile obtained by azimuthal averaging shows peaks depending on the structure of the samples. From [65]. Reprinted with permission of John Wiley and Sons.

where $\rho(\mathbf{r})$ is the electron density of the target. In particular, the integral term in Eq. 2-40 can be calculated for spherical targets having the uniform electron density. Here targets are assumed to be spherical (radius r_0) and to have the uniform electron density:

$$\rho(\mathbf{r}) = \begin{cases} \rho_0 & (|\mathbf{r}| \leq r_0) \\ 0 & (\text{otherwise}) \end{cases} \tag{2-41}$$

When the target sphere is composed of N single elements with the atomic number Z, the number of electrons in the target can be connected with there parameters:

$$\frac{4\pi\rho_0 r_0^3}{3} = NZ \tag{2-42}$$

Using these factors, Eq. 2-40 can be reduced to the below formula:

$$N_s(\Omega) = J_0 r_e^2 (4\pi\rho_0 r_0^3)^2 \{1 - \sin^2 2\theta \cos^2(\phi - \varphi)\} \left[\frac{\sin qr_0 - qr_0 \cos qr_0}{(r_0)^3}\right]^2 \mathrm{d}\Omega \tag{2-43}$$

$$= J_0 r_e^2 (3NZ)^2 \{1 - \sin^2 2\theta \cos^2(\phi - \varphi)\} \left[\frac{\sin qr_0 - qr_0 \cos qr_0}{(qr_0)^3}\right]^2 \mathrm{d}\Omega, \tag{2-44}$$

where the magnitude of the momentum transfer can be related to the scattering angle θ:

$$q = |\mathbf{q}| = \frac{4\pi}{\lambda} \sin\theta. \tag{2-45}$$

2.2.3 Bragg scattering: coherent scattering by a crystal

It is called that a sample has a crystalline structure if the atoms or molecules constructing the sample make a lattice in some periodic manner. Photons scattered from a crystalline sample have been also proven to show periodic intense spots in certain scattering angles on a detector. These bright spots are well known as Bragg spots and their profiles reflect the crystalline properties of the sample such as the distance between an atom and one of the neighborhood, i.e. the lattice constant. Each Bragg spot corresponds to a plane consisting of some of the components, which is identified with the so-called Miller indices. This subsection will introduce some concepts on crystals and two ways of treatment of reflection from a crystal: Bragg's law and Laue's condition. The Bragg law and the Laue condition are proven to be exactly equivalent to each other in mathematics.

Conceptualization of crystals

Coordinates of the components of a crystal: For simplicity, assume that the components of the target crystal are atoms. Due to its periodicity, the coordinates of atoms in the crystal can be defined by three fundamental vectors, $\mathbf{a}_1, \mathbf{a}_2, \mathbf{a}_3$:

$$\mathbf{x}(p, q, r) = p\mathbf{a}_1 + q\mathbf{a}_2 + r\mathbf{a}_3, \tag{2-46}$$

where p, q, r is integers. The lattice can be described by a series of the delta functions:

$$z(\mathbf{r}) = \sum_p \sum_q \sum_r \delta(\mathbf{r} - \mathbf{x}(p, q, r)). \tag{2-47}$$

The reciprocal lattice: The Fourier transform of the lattice $z(\mathbf{r})$ also constructs another series of delta functions, which is often called the reciprocal lattice [74]. Mathematically the reciprocal lattice can be expressed as

$$\begin{aligned} Z(\mathbf{q}) &= \int \mathrm{d}\mathbf{r} z(\mathbf{r}) e^{-\mathbf{i}\mathbf{q}\cdot\mathbf{r}} & (2\text{-}48) \\ &= \frac{1}{V_c} \sum_h \sum_k \sum_l \delta(\mathbf{q} - \mathbf{x}^*(h, k, l)), & (2\text{-}49) \end{aligned}$$

where $V_c = \mathbf{a}_1 \cdot (\mathbf{a}_2 \times \mathbf{a}_3)$ is the volume of the unit cell of the real lattice. The center of the delta

functions, $\mathbf{x}^*(h,k,l)$, can be expressed by using three fundamental vectors in the reciprocal space:

$$\begin{aligned} \mathbf{x}^*(h,k,l) &= h\mathbf{a}_1^* + k\mathbf{a}_2^* + l\mathbf{a}_3^*, \\ \mathbf{a}_1^* &= \frac{2\pi}{V_c}(\mathbf{a}_2 \times \mathbf{a}_3), \\ \mathbf{a}_2^* &= \frac{2\pi}{V_c}(\mathbf{a}_3 \times \mathbf{a}_1), \\ \mathbf{a}_3^* &= \frac{2\pi}{V_c}(\mathbf{a}_1 \times \mathbf{a}_2). \end{aligned} \tag{2-50}$$

The fundamental vectors in the reciprocal space satisfy the orthogonal relation with the fundamental vectors in the real space:

$$\mathbf{a}_i \cdot \mathbf{a}_j^* = 2\pi\delta_{ij}, \tag{2-51}$$

where $\delta_{ij} = 1\ (i = j),\ 0\ (i \neq j)$. Fig. 2.8 shows the construction of the real lattice and its reciprocal lattice.

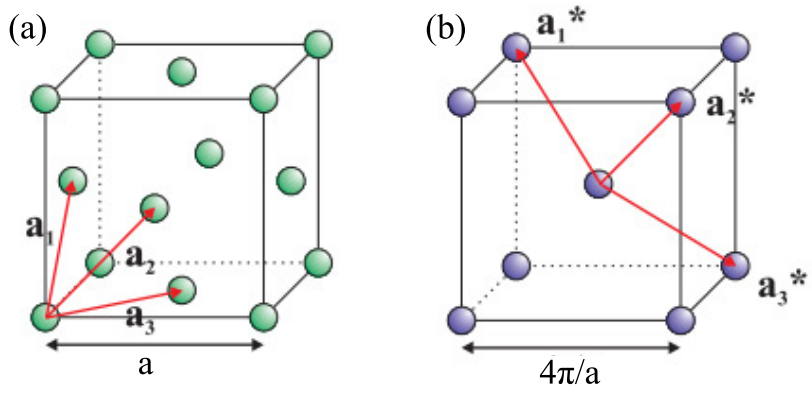

Figure 2.8: Schematics of a real lattice (a) and its reciprocal lattice (b). Adopted from [65]. Reprinted with permission of John Wiley and Sons.

Miller indices: For each group of (h,k,l), there is a series of lattice planes to which the reciprocal vector $\mathbf{x}^*(h,k,l)$ is perpendicular. This means all the lattice planes in a crystal can be uniquely identified with a corresponding group of indices (h,k,l). The indices characterizing reciprocal vectors are called Miller indices and the corresponding plane is often referred to as the (hkl) plane. The distance between a (hkl) plane and the adjacent (hkl) plane is given with the magnitude of the corresponding reciprocal vector:

$$d_{hkl} = \frac{2\pi}{|\mathbf{x}^*(h,k,l)|}. \tag{2-52}$$

For a crystal whose lattice belongs to the cubic space group in crystallography, d_{hkl} can be expressed as

$$d_{hkl} = \frac{a}{\sqrt{h^2+k^2+l^2}}. \tag{2-53}$$

Bragg's law

Consider a situation where a photon field with a wavelength λ and the strength E_0 propagates to planes composed of atoms and reflect, as shown in Fig. 2.9. The photon field reflecting from the bottom plane, E_{bottom}, travels a distance longer than the photon field reflecting from the top plane, E_{top}, and the difference of the travel length is given by $L = 2d\sin\theta$, where d is the distance between the two planes and θ is defined in Fig. 2.9. Then the superposed field of E_{top} and E_{bottom} is detected by a detector. The strength of the detected field can be given as

$$E_{detect} = E_{top} + E_{bottom} = E_0(1 + e^{\mathrm{i}\frac{2\pi}{\lambda}\times 2d\sin\theta}) \times e^{\mathrm{i}\phi},$$

where ϕ is a phase shift common to E_{top} and E_{bottom} coming from the propagation. From the above expression of E_{detect}, one can see that the two fields strengthen each other when the difference of the travel length satisfies the following relationship:

$$2d\sin\theta = n\lambda, \tag{2-54}$$

where n is an arbitrary integer. On the contrary, the two fields weaken each other if $2d\sin\theta = (n + 1/2)\lambda$. These relations show that the superposed field of photons scattered in the angle θ satisfying Eq. 2-54 has high intensity. The equation 2-54 is well known as the Bragg law. Actually the number of the planes is dependent on the size of the target crystal, and the Bragg law is well valid under a condition where the distance of the detector from the interaction point of the incident photons and the target is enough far from the size of the target and the focal size of the incident beam.

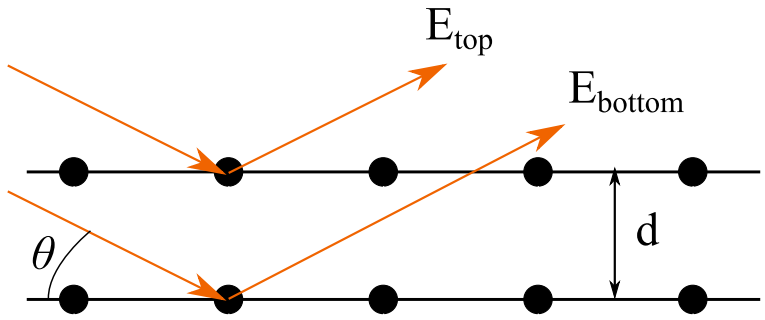

Figure 2.9: A schematic of the reflection of incident photon field by a pair of planes composed of atoms. The two planes are distant from each other by d. The incident field reflects in the direction characterized by a scattering angle θ.

Laue's condition

The electron density of the crystal can be expressed by combining the lattice function (Eq.2-47) and the electron density of each component atom. Similar to the derivation of Eq. 2-37, the scattering

amplitude of the crystal can be expressed as

$$S_{crystal}(\mathbf{q},\omega) = \sum_p \sum_q \sum_r f_j(\mathbf{q},\omega) \exp(-\mathrm{i}\mathbf{q}\cdot\mathbf{x}(p,q,r)) \tag{2-55}$$

The intensity of the scattered field from the crystal is proportional to $|S_{crystal}(\mathbf{q},\omega)|^2$, and $|S_{crystal}(\mathbf{q},\omega)|^2$ has the maximum value when $\mathbf{q}\cdot\mathbf{x}(p,q,r) = 2\pi \times n$ (n is an arbitrary integer). Considering the orthogonal relationship between the fundamental vectors, any $\mathbf{x}^*(h,k,l)$ satisfies this condition. This is known as Laue's condition.

Ewald sphere

The concept of the Ewald sphere is useful for visualizing diffraction in the reciprocal space. Consider the situation depicted in Fig. 2.10: an incident X-ray beam with the wavenumber vector $\mathbf{k}_0$ is scattered in the direction with an angle θ. In the Ewald sphere construction, a circle with a radius of $|\mathbf{k}_0|$, called an Ewald sphere, is drawn so that the terminal point of $\mathbf{k}_0$ is on a reciprocal lattice point (denoted by O in Fig. 2.10), and the starting point of the wavenumber vector of the elastically scattered beam, $\mathbf{k}$, is on the center of the circle. Then the terminal point of $\mathbf{k}$ (denoted by T in Fig. 2.10) is on the circle. The Laue condition satisfies only when the point T is on a reciprocal lattice point. In other words, one can observe the Bragg diffraction only when some reciprocal lattice points are on the circle. When the target crystal is rotated, then the reciprocal lattice of the crystal is also rotated, and this rotation can be reflected on the Ewald sphere construction by rotating the reciprocal lattice around the point O.

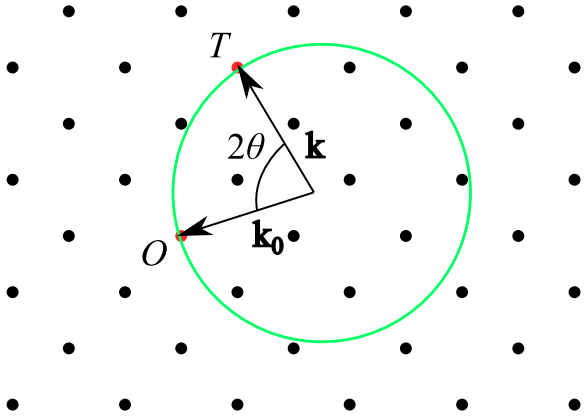

Figure 2.10: A schematic of the Ewald sphere construction in 2D. The Ewald sphere has a radius $|\mathbf{k}_0| = \frac{2\pi}{\lambda}$ and one of the reciprocal lattice points (usually $\mathbf{x}^*(0,0,0)$) is on the same point as the terminal point of the wavenumber vector of the incident beam, as denoted by O. The wavenumber vector of the scattered beam is drawn as its starting point is on the center of the Ewald sphere and its terminal point on the Ewald sphere, as denoted by T.

Scherrer's equation

Effects of crystal size on the profile of a Bragg spot has been investigated by Paul Scherrer [75]. He showed that the width of a Bragg spot contains information on the crystal size and derived a simple

relationship given by

$$\beta = \frac{K\lambda}{\tau \cos\theta}, \tag{2-56}$$

where K is a dimensionless value depending on the shape of the crystal, λ is the wavelength of the incident X-ray beam, τ is a characteristic size of crystal, and θ is the Bragg angle. For a spherical crystal, K is given as $(4/3)(\pi/6)^{1/3}$ [76].

2.3 Laser–cluster interaction: nanoplasma formation in the intense laser field

Plasma is often called the fourth state of matter and positively charged particles and negatively charged particles (often electrons) coexist in the matter in the plasma state. Nanoparticles have been reported to become a nanoscale plasma with a bulk-like density of electrons, so-called nanoplasmas, immediately in the irradiation of intense laser pulses[2]. The mechanisms of nanoplasma formation and corruption have been studied widely by using clusters [70]. A simple description of nanoplasma formation and its development deduced from the preceding studies is as follows [54]:

1. A single laser pulse ionizes a sample and the electrons are emitted, which develops the positive Coulomb potential of the sample.
2. When the Coulomb potential becomes deep enough, then electrons ionized from the components of the target are trapped by the potential and can move freely in the target. These electrons are often called quasifree electrons. At this stage, the ionization to the outside of the target becomes frustrated and nanoplasma formation begins.
3. Electrons in the nanoplasma gain kinetic energy from the laser field or exchange their kinetic energy with the components and electrons.
4. The nanoplasma expands by the internal pressure of the electron gas or by the Coulombic force, and finally the component ions and electrons are disintegrated.

Fig. 2.11 describes the above processes of nanoplasma dynamics. The expansion mechanism of nanoplasma depends on the properties of the irradiation field and the sample size. The following subsections will discuss each dependence.

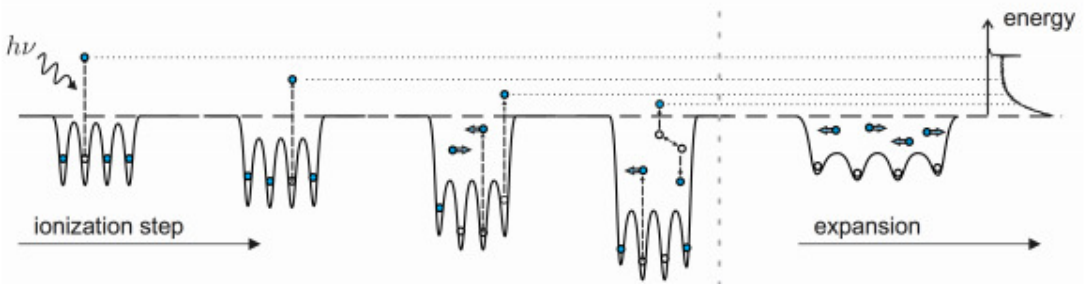

Figure 2.11: A schematic of nanoplasma formation and its development. From [54], licensed under CC BY-NC-SA 3.0.

2.3.1 Wavelength dependence of nanoplasma formation

The nanoplasma formation is dependent on the wavelength, or the photon energy, of the excitation laser field. As mentioned in subsection 2.1.3, the intense NIR[3] laser field can lead field ionization

[2] Any matter has been thought to become plasma under intense laser pulses.
[3] λ =760–1,400 nm [77].

of samples and subsequently transfer their energy to ionized electrons via inverse Bremsstrahlung heating, finally resulting in the nanoplasma formation/expansion. As the wavelength is shorter, the electric field effect is suppressed and MPI mechanisms possible. In the VUV[4] regime, MPI and inverse Bremsstrahlung heating are dominant processes of sample heating, and the ionization is further driven by collisions of electrons and ions inside the strongly coupled plasma [28]. In the extreme ultraviolet[5] (EUV) to hard X-ray[6] regime, direct photoionization and subsequent multistep ionization become the dominant ionization mechanisms.

2.3.2 Size dependence of nanoplasma formation

Studies using small clusters have suggested that small samples irradiated by a laser field tend to explode via Coulomb repulsion [26, 78, 79]. Small samples cannot trap electrons efficiently and the heating of the samples is suppressed due to their little frequency of electron-ion collisions. As a result, the irradiated samples become an ensemble of positively charged ions and explodes by Coulomb repulsion. On the other hand, large clusters tend to efficiently trap electrons in their deep Coulomb potentials coming from their size and therefore thermalize efficiently. Consequently, the resulting nanoplasma expands rather hydrodynamically due to comparably high electron temperatures [26, 79].

2.3.3 Structural and electronic damage under laser field

Intense laser fields make samples highly excited and the configuration inside the samples could be strongly changed. The changes in the configuration, often referred to as "sample damage," is classified with regards to two aspects [20, 80, 81]:

- Electronic damage: changes in the electronic configuration (e.g. the energy level of atoms, the whole potential in a sample).
- Structural damage: changes in the structure of samples.

The electronic damage is inevitable under irradiation of intense laser field and could lead to bond breaking and changes in the scattering factor, which limits the achievable spatial resolution of the structure retrieved from diffraction images. The structural damage follows the electronic damage and could make it difficult to investigate the structure of samples in their non-damaged state.

A molecular dynamics simulation conducted by Neutze et al. [20] indicates that X-ray pulses with a few to tens fs duration have the possibility of investigating the morphology and macroscopic structure of samples before structural damage starts. This finding gives a concept "diffract-before-destroy" to the diffractive imaging using FEL pulses. While diffractive imaging methods with FEL pulses have been applied to various types of samples, it has been also an active field to investigate these damage

[4] λ =10–200 nm [77].
[5] λ =10–121 nm [77].
[6] λ =1–100 pm [77].

processes. Determining their timescales, effects on the measured signals and the structural changes in the samples is important to accurately retrieve the structure from the diffraction patterns and understand laser–matter interaction, and recently the actual correlations between diffraction images and other spectroscopic have been studied by combining diffractive imaging and spectroscopies [44, 46, 49].

2.3.4 Exploration of structural dynamics of nanoplasma using coherent X-ray scattering

While electronic property and underlying processes of nanoplasma and its formation have been investigated by using charged-particle and fluorescence spectroscopies for a long time, it is very recent that the direct visualization of the structure and structural changes in nanoplasma was realized. As introduced in chapter 1, the first experiment investigating the structural changes in nanoplasma expansion by using CDI was performed at LCLS [48]. The results are summarized in Fig. 1.3 and indicate gradient changes in the electron density propagating from the surface of the nanoplasma generated from a Xe cluster irradiated by an intense NIR laser pulse. This phenomenon is called surface softening. Surprisingly, the speed of the observed surface softening estimated from the experimental/theoretical results is on the same order of the plasma sound speed well defined in the equilibrium state, even while non-equilibrium processes proceed in the nanoplasma development. Here the plasma sound speed is given by [26]

$$v_{plasma} = \sqrt{\frac{Zk_BT_e}{m}}, \tag{2-57}$$

where Z is the average charge of plasma, k_B is the Boltzmann constant, T_e is the temperature of the electron gas in the plasma, the so-called electron temperature, and m is the mass of the component ions in the plasma[7]. The similarity of the core shrinking speed to the plasma sound speed remains a question to reveal.

The surface softening of nanoplasma is also observed in an experiment using soft X-ray FELs, which was conducted at LCLS [82]. In this experiment, Xe clusters with the average radius of 61 nm were irradiated by 1.5-nm (826 eV) single X-ray pulses with the intensity of 2×10^{16} W/cm^2, and the SAXS intensity was collected in the long time scale from 0 to 800 fs after X-ray pumping. Fig. 2.12(a) shows the temporal change of diffraction intensity from pure Xe nanoclusters, which exhibits a decrease of the diffraction intensity at the larger q and a shift of its local minima to larger q. This behavior is very similar to that of the NIR-heated Xe clusters.

The SAXS studies introduced above give an insight into nanoplasma development in terms of the changes in the electron density. On the other hand, an X-ray pump–X-ray probe study with a WAXS technique carried out at LCLS [61, 62] gives some clues for understanding atomic-scale structural

[7]Here a plasma consisting of electrons and single-species ions is assumed.

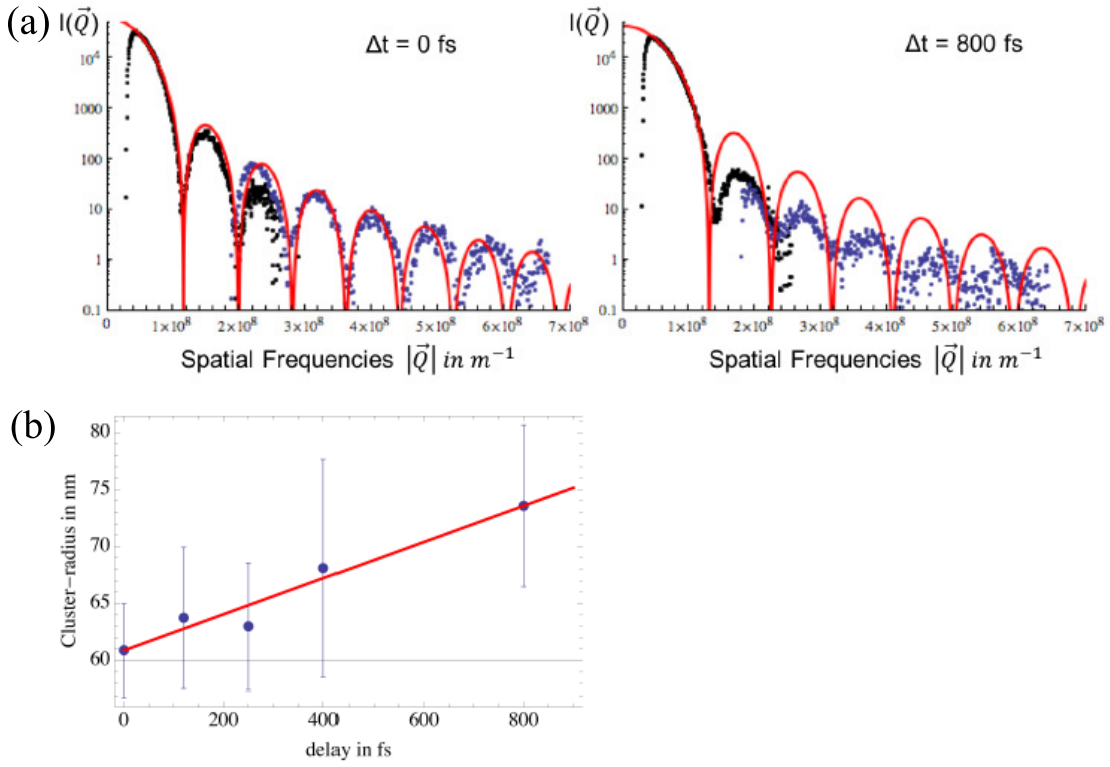

Figure 2.12: X-ray pump–X-ray probe SAXS experiment on Xe clusters at LCLS that shows surface softening of X-ray excited nanoplasma. (a) The temporal development of the diffraction intensity from 0 and 800 fs. (b) The temporal evolution of the cluster radius induced by 1.5-nm XFELs. From [82], licensed under CC BY 4.0.

changes in the nanoplasma formation. In this study, Bragg reflection signals from Xe clusters excited by single hard X-ray FEL pulses were collected in coincidence with ion spectroscopy. Fig. 2.13(a) shows the temporal shift of the position of the observed spots from fcc (220) Bragg reflection, and Fig. 2.13(b) shows the temporal evolution of the lattice constant and the apparent lattice disorder of Xe crystals induced by the XFEL irradiation. After excitation, the lattice constant shrinks within 80 fs, which means that a Xe cluster undergoes a transient lattice contraction in solid-to-nanoplasma transition before it expands, while the ion time-of-flight spectra suggest a rapid expansion of the nanoplasma, as the authors mentioned. According to the authors, this paradoxical situation is interpreted as ultrafast changes in electronic configuration upon ionization as follows. Quasifree electrons in a highly excited Xe cluster have increased mobility and behave like delocalized valence electrons, which converts the van der Waals bonds of the Xe cluster into a more “metallic-like” state. As a result, the change in the bond character leads to the shrinkage of the lattice constant.

These groundbreaking investigations have shown the effectiveness of the pump-and-probe diffractive imaging as well as the ultrafast structural changes in highly excited atomic clusters. However, the way of changes in the local order in a crystal and the underlying processes are still unclear. This is a theme of the second experiment of this thesis.

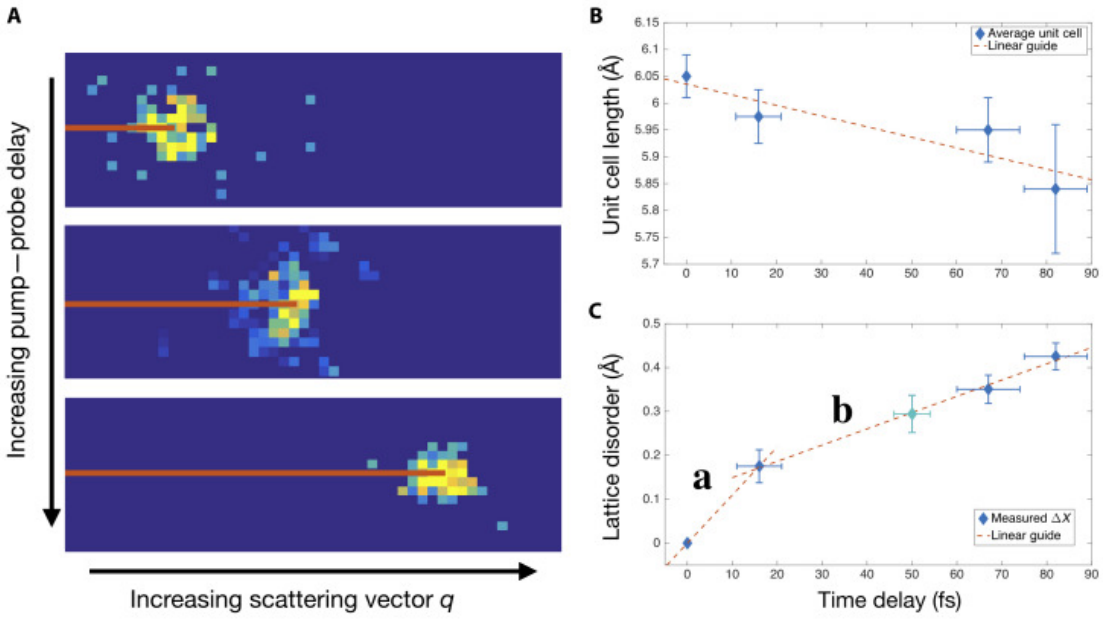

Figure 2.13: An X-ray pump–X-ray probe WAXS experiment on Xe clusters at LCLS that shows an early evolution of the nanoplasma transition. From [61], licensed under CC BY-NC 4.0.

Chapter 3

Concepts of experimental apparatus

The principle and design concept of the experimental apparatus are described in this chapter. We constructed experimental setups for the multispectroscopy of free-flying nanoclusters at SACLA. The interaction of xenon clusters with the intense laser pulses was studied by using a combination of X-ray scattering methods, fluorescence and ion spectroscopies in this work. The components of the experimental setups are described in the following sections: 3.1 XFEL source, 3.2 optical laser system, 3.3 cluster source, 3.4 ion time-of-flight detector, 3.5 X-ray detector, and 3.6 signal and data processing. The specific setups for each experiment will be described in chapters 4 and 5.

3.1 Free-electron laser source

From the discovery of X-rays by Röntgen, X-rays have been used to study the structure of any material and various types of X-ray sources have been developed. Today, intense laser pulses with a duration of a few tens femtoseconds can be provided by FEL sources in wide spectral regimes [83] since the first development of FEL source in the 1970s [84].

3.1.1 Brilliance: an indicator of light sources

While several aspects of light sources determine the quality of the beam they produce, FEL and synchrotron light sources are often characterized by a spectral brightness, or peak spectral brilliance. Brilliance B is defined as [65]

$$B = \frac{n}{\Delta t \times A \times \Omega \times \Delta E}, \tag{3-1}$$

where n is the number of emitted photons, Δt is the period of the emission, A is the cross section of the source, Ω is the solid angle defined as the product of the horizontal divergence and the vertical one of the beam, and ΔE is 0.1% of the bandwidth of the center of the energy spectrum. Fig. 3.1 shows the peak spectral brilliance of some synchrotron and FEL sources. Most of the synchrotron

sources currently operated are classified as the third generation. FEL sources are classified as the fourth generation and have linear accelerators (linacs) of the initial electron beam.

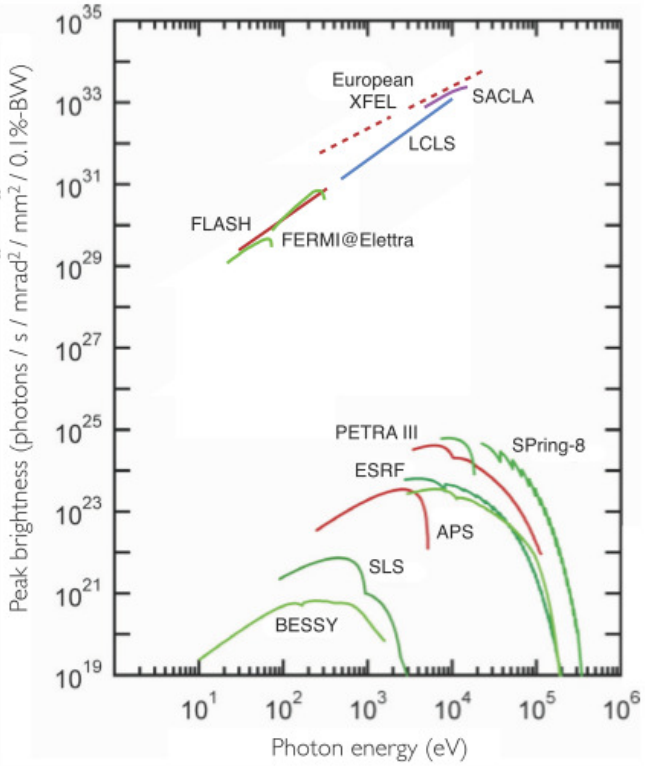

Figure 3.1: The peak brilliance vs the photon energy plots of some current and future synchrotron and SASE light sources. From [85], licensed under CC BY 3.0.

3.1.2 X-ray emission in an undulator

FELs are often characterized by peak brilliance. The principle of laser emission is the same over all of the linac-based light sources shown in Fig. 3.1. The linacs are composed of a set of alternating magnets, which is called "undulator." When a group of electrons (called an electron bunch) passes in an undulator, electrons in the bunch are accelerated in an undulator so that their kinetic energy gets relativistic. Simultaneously the electrons are periodically deflected due to the alternating magnetic fields and electrons in the bunch move on a wiggling path. Bremsstrahlung radiation occurs at timings when the direction of the electron bunch is changed. Fig. 3.2 shows a schematic of radiative emission in the X-ray generation methods using magnet arrays.

Each magnet in an undulator is spatially small and the magnetic fields between each pair of magnets are set to low. Under these configurations, the deflection of electrons is small and therefore the radiation angle is small, which realizes that the radiated photons from the electrons can overlap and interact with the electrons in every undulator period [65]. When the phase of electron wiggling matches that of the undulator period, the interference of the radiation and the electron bunch is constructive, that is, the superposition of the early emitted radiation waves and the late emission

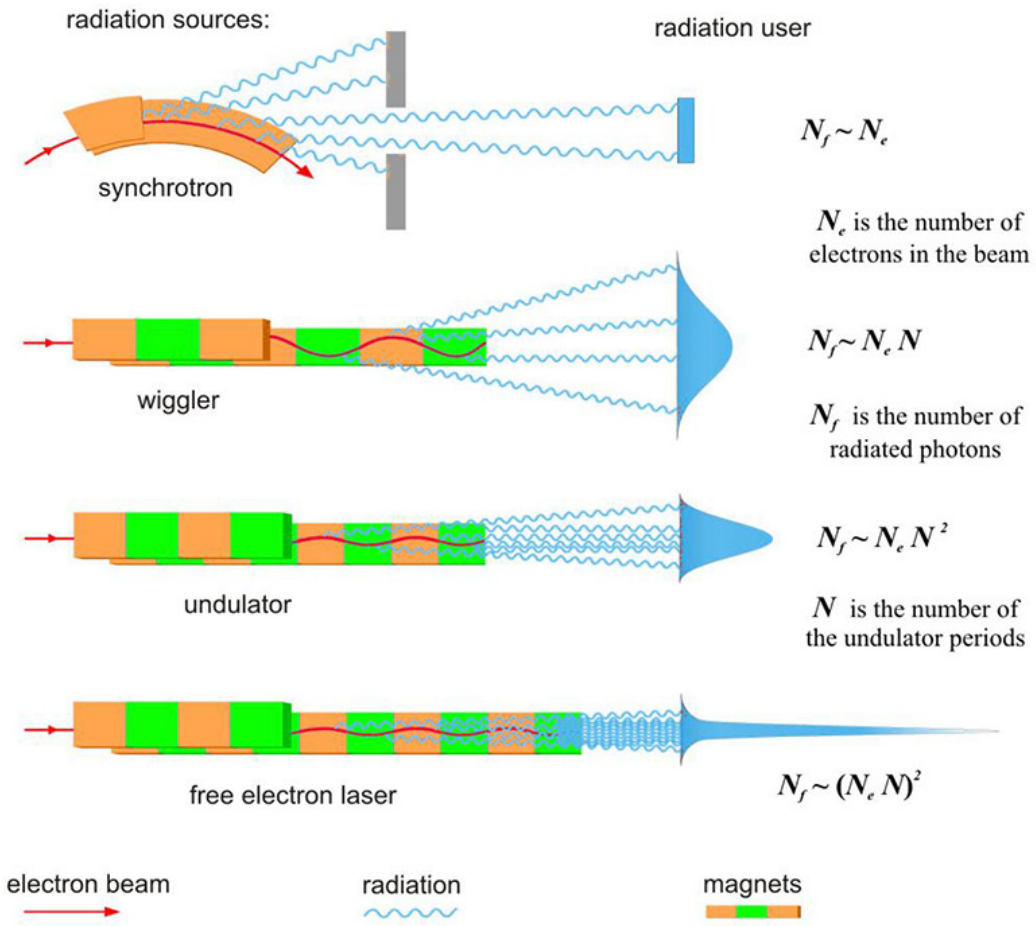

Figure 3.2: Schematics of several X-ray generating methods using magnets (orange & green). The emitted spatial power distribution is expressed in light blue in the right side. From [86], licensed under CC BY 3.0.

waves makes more intense radiation waves. This is the principle of lasing by an undulator and happens at a resonant wavelength given by

$$\lambda_{res,und} = \frac{\lambda_u}{2\gamma^2}\left(1 + \frac{K_0}{2} + \gamma^2\theta^2\right), \tag{3-2}$$

where λ_u is the undulator period, γ is the Lorentz factor $\gamma = 1/\sqrt{1 - v^2/c^2}$, θ is the observation angle, and K_0 is the undulator parameter. The undulator parameter is given by [87]:

$$K_0 = \frac{eB_0\lambda_u}{2\pi mc}, \tag{3-3}$$

where B_0 is the magnetic field between the magnets. Eqs. 3-2 and 3-3 show that the wevelength of the radiaion waves depends on the magnetic field between the pairs of magnets and therefore can be tuned by changing the magnetic field. As a result, the power of emitted radiation depends quadratically on the number of magnetic dipole pairs [88]:

$$P \propto n_{mag}^2 \tag{3-4}$$

3.1.3 SASE emission in a FEL

Undulators can emit a brilliant photon beam through the interaction between the emitted radiation and electrons in the path. When the length of the undulators increases, further constructive interference between emitted fields and electrons occurs. Although the accelerated electrons have relativistic velocity in the traveling path, their velocity is slightly slower than the speed of light. This means that the propagating photons and electrons have a phase difference, and depending on the phase, each electron gains or loses energy during the interaction with the photon field. Consequently, an electron bunch will be periodically modulated and behave like a set of smaller bunches in the photon field. This modulation is referred to as "microbunching." Fig. 3.3 shows a schematic of microbunching in a long undulator.

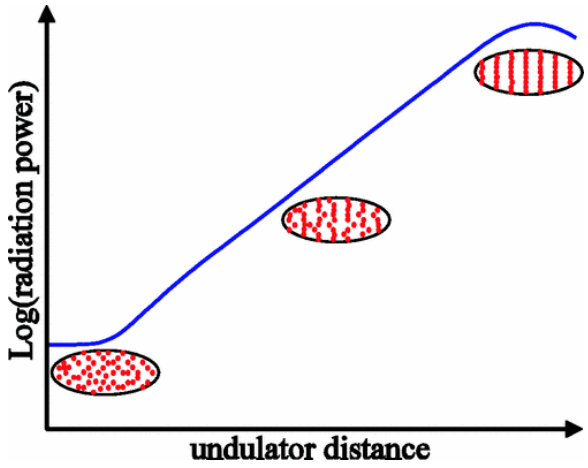

Figure 3.3: A schematic of microbunching. As an undulator gets longer, an electron bunch travels and interacts with the emitted radiation fields in the longer path, which leads to the periodic modulation of the electron bunch. Then each microbunch in the modulated bunch interacts with the radiation fields and eventually, the radiated photons make a coherent beam. The emitted power increases exponentially with respect to the length of the undulator and saturated at a certain undulator length. From [89], licensed under CC BY 3.0.

To achieve microbunching, an electron bunch has to interact with the radiation field collectively, and this occurs only when the electrons have a narrow spatial and kinetic energy distributions. These distributions are characterized by a quantity called "emittance", and low-emittance electron bunches is essential for light sources to generate high-quality laser pulses. Each FEL source is designed to produce low-emittance bunches, and the resonance condition occurs when $\theta = 0$ (see Eq. 3-2). So,

$$\lambda_{res,FEL} = \frac{\lambda_u}{2\gamma^2}\left(1 + \frac{K_0}{2}\right). \tag{3-5}$$

Under this resonant condition, the emitted light overtakes the electrons by exactly one radiation cycle during the undulator period. That is, the period of the oscillation of electrons in the field matches the period of the oscillation of electrons in the undulator, resulting in the enhancement of the intensity of the radiated beam. This is a key process of laser emission by FELs and called

"slippage" [87]. Fig. 3.4 shows a schematic of the slippage. During the travel in a long undulator, the electron bunch interacts with the phase-matched photon field and becomes more structured, and thereby the photon field is amplified, which is often called "self-amplification". This type of radiation is called self-amplification by spontaneous emission (SASE), and the power of emission depends quadratically on the number of electrons:

$$P \propto n_e^2. \tag{3-6}$$

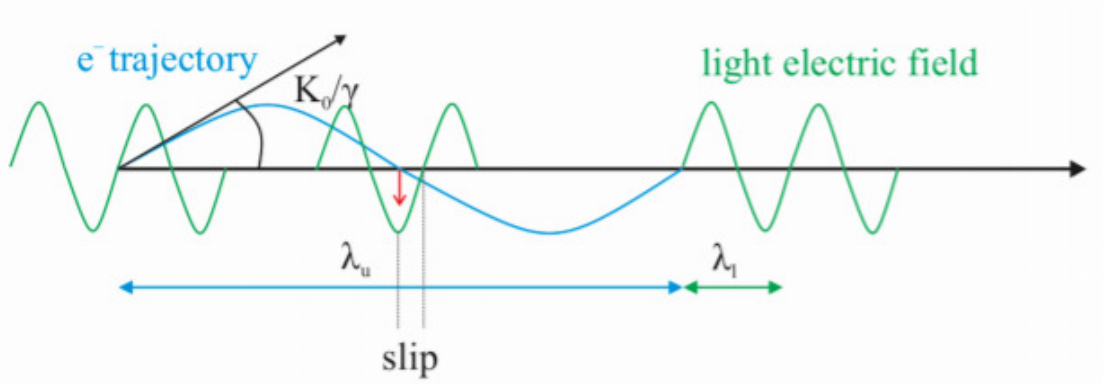

Figure 3.4: A schematic of the slippage of the light wave with respect to the electron beam in an undulator. From [62], licensed under CC BY-NC 3.0.

3.1.4 SACLA: the first facility providing FEL pulses with sub-Å wavelength

The SPring-8 Ångstrom Compact free-electron LAser (SACLA) is the FEL light source that was used in this work. SACLA is located at the SPring-8 synchrotron facility in Hyogo Prefecture, Japan. SACLA came online in 2011 as the second hard X-ray FEL in the world [90] and operates for users in 2012. The SACLA electron accelerator uses S-band and C-band technologies in the acceleration part. This technology has been tested and verified at SPring-8's first FEL facility, SPring-8 Compact SASE Source (SCSS). As built on the concept of a compact FEL, SACLA has only a 700 m length (the acceleration part: 400 m, the undulator part: 240 m, the experimental research building for users: 60 m along the direction of XFEL injection), so SACLA is the shortest among the existing XFEL sources.

Beamline

The detail of SACLA at the time of its operation is depicted in Fig. 3.5. The electron injector has a single-crystal cerium hexaboride (CeB_6) and generates a low-emittance electron beam of $\sim 6\pi$ mm mrad [91]. A single electron beam is collimated and then accelerated and compressed alternately in three C-band acceleration tubes and compression systems, resulting in an electron bunch with high

current up to 3 kA and relativistic kinetic energy. After acceleration and compression, the electron bunch is introduced to an undulator. As a key component of the technologies building SACLA, magnet arrays are installed inside vacuum chambers (in-vacuum undulator system), which allows us to decrease the magnet size down to an 18-mm periodic length (λ_u) and increase the effective magnetic field between pairs of magnets. With this device, a sufficiently high magnetic deflection parameter K_0 up to 2.2 is achieved at the time of 2012 [90] and nowadays reaches 2.7 [92]. The electron bunch is deflected by a magnet into a dump after exiting the undulator, and the generated X-ray laser pulse is deflected and focused by soft or hard X-ray mirrors and introduced to the experimental hutches.

Typical parameters of the electron beam and the X-ray pulse at the time of 2019 [92] are listed in Tab. 3.1. SACLA can provide XFEL pulses with the shortest wavelength (0.634 Å[90]) of all the existing XFEL facilities. SASE operation can be used normally, and recently two-color emission and self-seeding emissions have been realized and available [93, 94]. In addition to the operation at beamlines 2 (BL2) and 3 (BL3), soft X-ray FEL pulses are available at beamline 1 (BL1) since 2016.

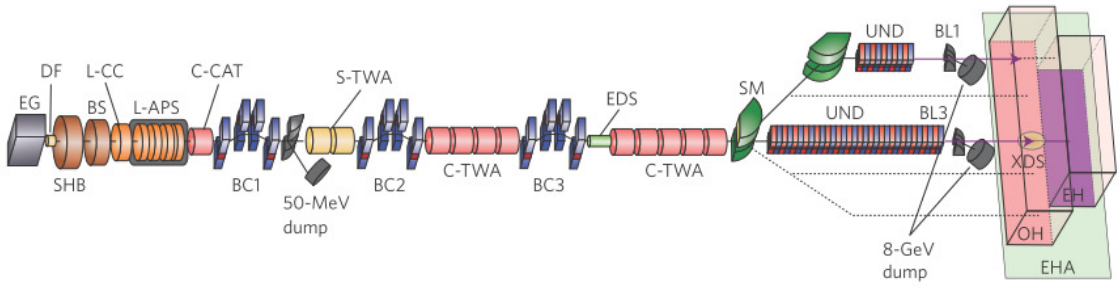

Figure 3.5: A schematic of the accelerator of SACLA. From [90]. Reprinted with permission from Nature Publishing Group.

Table 3.1: Typical parameters of the electron beam and the X-ray pulse of SACLA. From [92], licensed under CC BY 3.0.

Parameter	BL1	BL2 and BL3
Electron beam energy (max.)	800 MeV	8.5 GeV
Bunch charge	0.2-0.3 nC	0.2-0.3 nC
Peak current	0.3 kA	$>$ 10 kA
Bunch length (FWHM[1])	$<$ 1 ps	$<$ 20 fs
Repetition (max.)	60 Hz	60 Hz
Undulator period	18 mm	18 mm
Undulator K_0 value (max.)	2.1	2.7
# of undulator units	4.5 m $\times$ 3	5 m $\times$ 18 (BL2), 5 m $\times$ 21 (BL3)
Photon energy	40–150 eV	4–15 keV
FEL pulse energy	0.1 mJ 100 eV	0.7 mJ 10 keV

BL3 of SACLA is the main beamline and designed by taking account of flexibility in user experiments. It has been widely used for various purposes and many notable results have been generated

from this beamline. A schematic of the X-ray optics from down to the optical hutch (OH) of BL3 is shown in Fig. 3.6. The X-ray optical system has two monitoring systems installed to OH and the experimental hutch 1 (EH1): an arrival timing monitor for pump-and-probe experiments [95], and an inline spectrometer for X-ray photon diagnostics [96]. Fig. 3.7 shows an overview of the X-ray optical system from the downstream side of OH to EH2. A diffraction grating installed in OH splits XFEL beam into three pulses, which are often referred to as the 0th-order (main beam) and the ±1st-order branches. The −1st branch is guided to a gallium arsenide (GaAs) crystal of the arrival timing monitor installed in EH1. The +1st branch is diffracted by a Si crystal of the dispersive spectrometer and detected by a multi-port charge-coupled device (MPCCD) sensor to monitor XFEL spectra for each shot. The inline spectrometer is installed in the upstream vacuum duct of the XFEL pass and composed mainly of a thin diamond film and an MPCCD sensor. The configuration of the diamond film is adjusted so that it diffracts XFEL pulses to the MPCCD sensor. Due to the high transmittance of the film, the inline spectrometer enables shot-by-shot diagnostics of the photon energy of XFEL pulse.

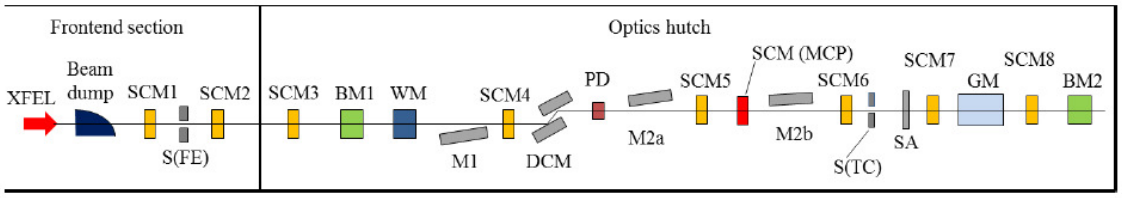

Figure 3.6: An overview of the optical system of BL3 at SACLA. SCM(MCP): screen monitor with a microchannel-plate image intensifier, BM: thin-foil beam monitor, WM: thin-foil wavelength monitor, M: total reflection mirror, DCM: double-crystal monochromator, PD: photo diode, GM: scattering-based gas monitor, SA: solid attenuator. From [97], licensed under CC BY 3.0.

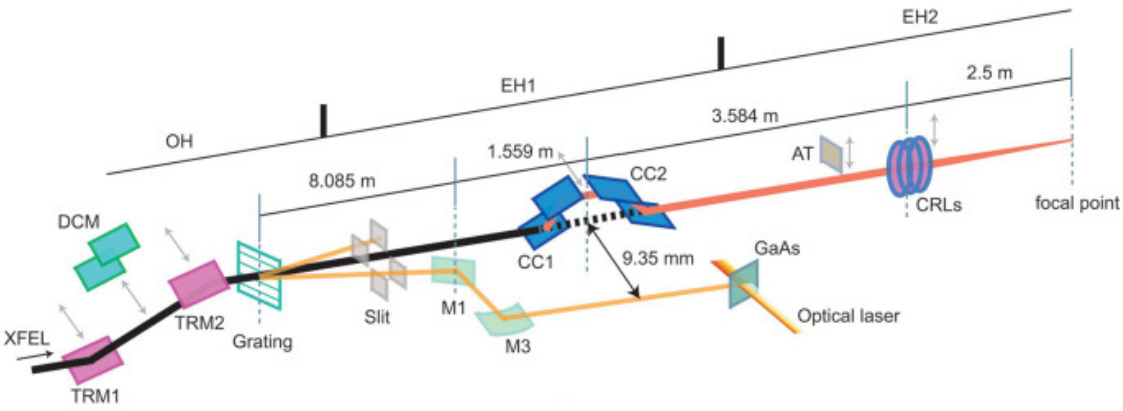

Figure 3.7: An overview of the X-ray optical system from the downstream side of OH to EH2 at BL3 of SACLA. TRMs: total reflection mirrors, DCM: double-crystal monochromator, M1 and M3: mirrors to reflect the −1st-order branch, CCs: channel-cut crystals, AT: silicon attenuator, CRLs: compound refractive lenses. From [98], licensed under CC BY 4.0.

Table 3.2: Typical radiation parameters of BL3 at a photon energy of 10 keV. From [97], licensed under CC BY 3.0.

Parameter	Value
Electron beam energy [GeV]	8
Repetition rate [Hz] (maximum)	60
Undulator deflection parameter (K value)	2.1
Photon energy [keV]	10
Bandwidth	5×10^{-3}
Beam size at EH2 [mm, FWHM]	0.3
Peak power [GW] (at July, 2012)	> 30
Pulse energy [mJ]	0.3
Average power [W] (at 60Hz operation)	0.02
Pulse duration [fs]	< 10
Photons per pulse	2×10^{11}

Arrival timing monitor

There is a fluctuation between the arrival timings of an XFEL pulse and a NIR pulse when using these pulses for pump-and-probe experiments. The fluctuation is referred to as jitter. It is of importance to measure the jitter to compensate for the difference between the arrival timings and thereby increase the temporal resolution. Fig. 3.8 shows a schematic of the arrival timing monitor. It utilizes the property of a GaAs crystal that the transmittance of GaAs in the optical spectral regime decreases by absorbing X-ray photons. For each shot, a NIR pulse is irradiated to the crystal vertically, and a -1st-order branch of an XFEL pulse is irradiated to the GaAs crystal with an angle of 45°. Then the spatial distribution of the NIR transmittance of the crystal is measured by a CCD camera. The temporal jitter between XFEL pulses and optical laser pulses reflects on the edge of the transmittance shown in the measured CCD images.

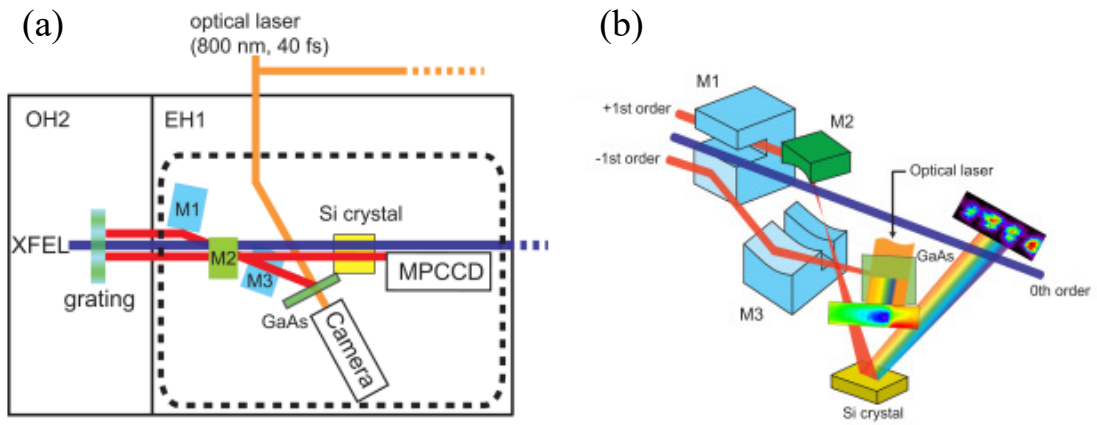

Figure 3.8: The arrival timing monitor and the dispersive spectrometer. (a) A top-view diagram of the optical system. (b) A schematic of the arrival timing monitor and the dispersive spectrometer. A grating installed in OH2 splits XFEL pulses into the main beam and branches for photon diagnostics and measurements of the temporal jitter between XFEL and optical laser pulses. For each shot, the -1st-order branches and NIR pulses are irradiated to a GaAs crystal and images of the crystal are recorded by a CCD camera. From [98], licensed under CC BY 4.0.

Experimental hutches

BL3 has five experimental hutches, each of which is designed for specific purposes. EH2 is designed for pump-and-probe measurements and one can investigate ultrafast dynamics in laser-matter interaction by the use of EH2. EH2 has Beryllium compound refractive lenses (CRLs) as a focusing system of XFEL pulses [98]. The CRLs can focus XFEL pulses with the photon energy available at SACLA (5–15 keV), and the resulting focal spot size reaches around 1 μm at full width at half maximum (FWHM). EH3 is designed for coherent focusing and has a focusing system composed of a pair of mirrors in the Kirkpatrick-Baez (KB) geometry [99], whose schematic is shown in Fig. 3.9. The KB mirror focusing system has the ability to focus XFEL pulses down to 1 μm (FWHM) at the photon energy of 10 keV, and the resulting power density can reach 10^{18} W/cm^2 at the focal point. Thus, the XFEL beam available in EH3 is suitable for the investigation of nonlinear phenomena and optics, CDI experiments of the nanoscale samples and non-crystal samples such as biomolecules, and so on.

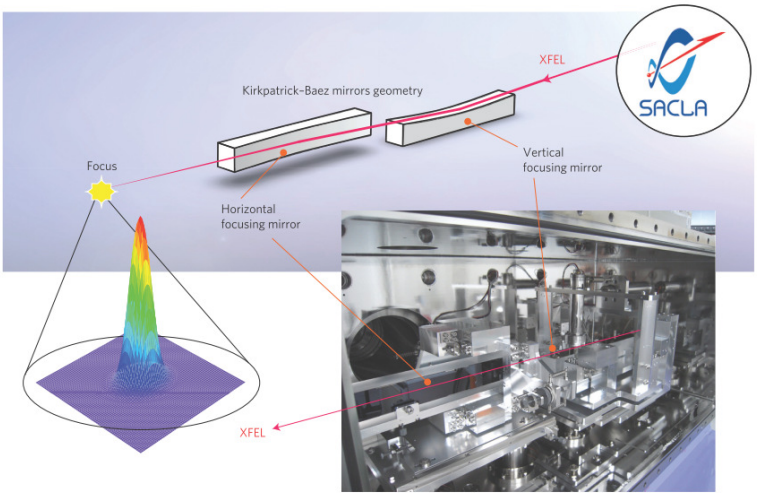

Figure 3.9: A schematic of KB mirrors and the deployment of KB mirrors in SACLA. The incident X-ray beam is focused both horizontally and vertically by a pair of concave mirrors down to 1 μm at FWHM. From [100]. Reprinted with permission from Nature Publishing Group.

3.1.5 FEL diagnostics in the experimental chambers

A home-made position monitor was installed to each reaction chamber in order to monitor the positions of XFEL and NIR pulses in a vacuum. Fig. 3.10 shows photographs of the position monitors used in the two experiments for this thesis. The position monitor had three elements: a cerium-doped yttrium aluminum garnet (Ce:YAG) screen, a gallium arsenide (GaAs) crystal, and a gold (Au) cross wire. These elements were used for the following purposes:

- Ce:YAG screen: to monitor the position of XFEL beams.
- GaAs crystal: to check spatial and temporal overlaps between XFEL and optical laser pulses in pump-probe experiments.

- Au cross wire: to check the focal size of XFEL beams.

The beam position monitor was installed to the reaction chamber so that the center of these elements could be moved to the designed reaction point. In the experiments, the Ce:YAG screen was used to adjust the position of the reaction chamber in order to overlap the designed reaction point with the XFEL focal point.

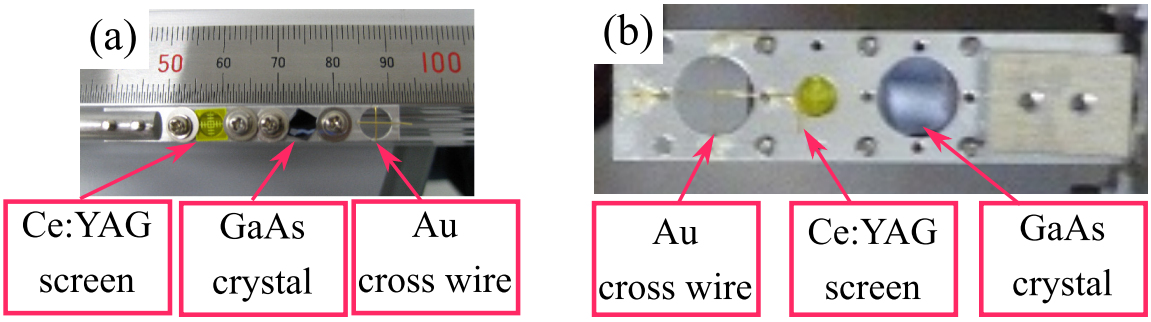

Figure 3.10: Photographs of the position monitors used in the SAXS experiment (a) and the WAXS experiment (b). Each element set on a stainless plate with holes is used for their appropriate purposes as described in the main text. The beam position monitor shown in (b) has a 1-mm hole next to the Au cross wire and the hole was used to adjust the position of the reaction chamber.

3.2 Optical laser systems

SACLA has an optical laser system which is suitable for pump-and-probe measurements. Fig. 3.11 shows a schematic of the optical laser system implemented in SACLA [97]. The Ti:sapphire chirped-pulse-amplification system is operated at 1 kHz and the laser pulses can be introduced in synchronization with the XFEL shots by using the master clock for the SACLA accelerators. The laser system provides NIR (800 nm) laser pulses with the pulse energy on the order of 1 mJ.

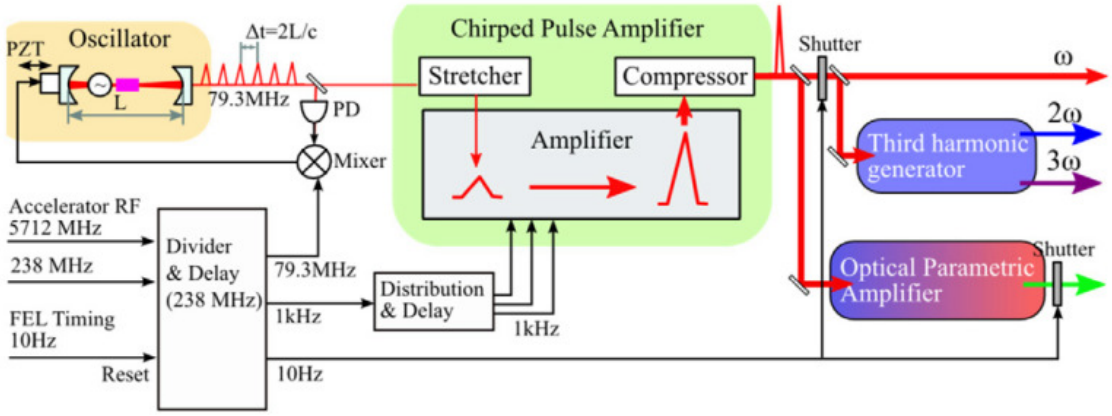

Figure 3.11: A schematic of the optical laser system implemented in SACLA. The Ti:sapphire laser system can provide second and third harmonics other than 800-nm NIR laser pulses. From [97], licensed under CC BY 3.0.

3.3 Cluster generation and jet source

Clusters are ensembles of particles such as atoms and molecules, and have been studied as isolated many-body systems. While various methods of generating clusters have been developed, the method utilizing adiabatic expansion of gas to the vacuum has been widely used for generating clusters from the gaseous flow. This section will describe the properties of clusters generated from the gaseous-state jet and the principle of cluster generation with the adiabatic expansion, partly by following the discussion in Ref. [101, 102].

3.3.1 Rare gas clusters

Clusters have the following properties:

- Clusters have the bulk-like density.
- The number of atoms/molecules in a cluster, which is often called "cluster size," can be tuned. The cluster size ranges from a few atoms[2] to mesoscopic sizes such that one can classify a cluster as a bulk material.
- A cluster is regarded as a finite system and has no energy dissipation into its surroundings.

In this work, Clusters composed of xenon atoms were used as the sample in the experiments. Rare gas atoms have closed electron shells and are chemically stable. The interaction force binding rare gas atoms in a cluster is the van der Waals force, which is well approximated by a Lennard-Jones potential:

$$V(r) = 4\epsilon \left\{ \left(\frac{\sigma}{r}\right)^{12} - \left(\frac{\sigma}{r}\right)^{6} \right\}, \tag{3-7}$$

where r is the interatomic distance, ϵ and σ are Lennard-Jones parameters and often referred to as the depth of the potential (binding energy) and the diameter of atom, respectively. Tab. 3.3 shows the values of the Lennard-Jones parameters. With this simple interaction force and the above features, rare gas clusters are regarded as ideal samples and have been widely used to study laser-matter interaction and well characterized.

Table 3.3: Lennard-Jones parameters for rare gas atoms. From [103]. Reprinted with permission from AIP Publishing.

Atom	Helium	Neon	Argon	Krypton	Xenon
σ [Å]	2.63	2.78	3.40	3.60	4.06
ϵ/k_B [K]	6.03	34.9	122	158	229

Studies on the structure of rare gas clusters have reported that they form an icosahedral structure for relatively small sizes, typically in nanometer scale [104], and that the stable structure is changed into a face-centered cubic (fcc) structure or a hexagonal closed-packed (hcp) structure when their size increases [105, 106]. The experiment for this work also observed xenon clusters with fcc and hcp structures by using a WAXS technique, which will be described in chapter 5.

[2] For example, clusters formed by two, three, ... atoms are called dimers, trimers, etc.

3.3.2 Principle of cluster generation by adiabatic expansion

As shown in Tab. 3.3, the binding energy of rare gas atoms corresponds to the temperature on the order of a few to hundreds Kelvin (K), so rare gas atoms can be aggregated together only when the temperature of the gas is enough low. Supersonic expansion is a common phenomenon used to create clusters in the gaseous state, which can be realized by releasing gas from a reservoir into a vacuum through a nozzle. The gas in the reservoir is kept at a certain stagnation pressure p_0 and a certain stagnation temperature T_0. p_0 is usually set so that the mean free path of the gaseous atoms is much smaller than the nozzle diameter, which achieves a condition that many collisions occur in the nozzle during the gas expansion but that no collisions occur in the supersonic expansion.

Collisions for cluster aggregation

Firstly let us discuss an intuitive picture of cluster aggregation by collisions, which has been introduced in some studies [102, 107]. The starting point of the cluster aggregation is the formation of a dimer. A dimer can be formed in a three-body collision, where two monomers bind each other and the third one is usually evaporated by removing the excess binding energy from the bound monomers. This can be expressed mathematically by the following formula,

$$A_1 + A_1 + X \rightarrow A_2 + X, \tag{3-8}$$

where A_1 is a monomer and X can be a certain body. The subsequent cluster growth from an aggregate can be achieved by the aggregate colliding another aggregate/monomer. This can be described mathematically as follows:

$$A_n + A_m \rightleftarrows A^*_{n+m}. \tag{3-9}$$

Here n, m denote the number of monomers in the aggregates A_n, A_m. In this collision, the new aggregate A^*_{n+m} is in a meta-stable state so it is possible to dissociate if no subsequent collisions release excessive energy from it. The deactivation by collision with another body can be formulated as

$$A^*_{n+m} + X \rightleftarrows A_{n+m} + X, \tag{3-10}$$

where X is another body again and can add or remove energy from A^*_{n+m}. The initial stages of the cluster growth are driven by monomer addition, and cluster–cluster coagulation becomes dominant in the later stage of the growth as more and more clusters are generated.

Phenomenological description of adiabatic expansion

Here the target gas is assumed to be an ideal gas, which is a good approximation for a gas flow composed of rare gas atoms. Fig. 3.12 shows a schematic of the adiabatic expansion. The velocity distribution of the gas in the reservoir follows thermal distribution[3] at a set temperature T_0. The

[3] This distribution is so-called a Maxwell-Boltzmann distribution.

enthalpy for an ideal gas in the reservoir can be given as

$$H_0 = C_P T_0. \tag{3-11}$$

Here C_P is the specific heat at constant pressure. The expansion of the gas through the nozzle occurs when the stagnation pressure is higher than the backing pressure p_b, i.e. the pressure at the outlet region. It is well known that the expansion will be supersonic only when the pressure ratio p_b/p_0 exceeds a critical value of G, which is given by

$$G = \left(\frac{\gamma+1}{2}\right)^{\frac{\gamma}{\gamma-1}}, \tag{3-12}$$

where $\gamma = C_P/C_V$ (C_V is the specific heat at constant volume). For atomic gases, γ can be treated as a value independent of temperature. In the nozzle, the steady gas flow is formed and directed to the outlet, and the enthalpy is converted into kinetic energy. Based on the conservation of energy, the following relation is satisfied:

$$H_0 = C_P T + \frac{1}{2}mv^2, \tag{3-13}$$

where T is the local temperature along with the gas flow, m is the mass of the atoms in the gas and v is the speed of the gas flow. Under the supersonic condition, where $p_0/p_b \geq G$, the speed of the steady gas flow reaches the sound speed at the exit of the nozzle, and increases beyond the sound speed after exiting the nozzle. The sound speed is given as

$$c_s = \sqrt{\frac{\gamma k_B T}{m}}, \tag{3-14}$$

where k_B is the Boltzmann constant. By rewriting Eq. 3-13 with the sound speed, the following relation between T and T_0 can be derived:

$$\frac{T}{T_0} = \left(1 + \frac{\gamma-1}{2}M_a^2\right)^{-1}, \tag{3-15}$$

where M_a is a Mach number: $M_a \equiv v/c_s$.

In the adiabatic expansion, the gas volume increase and the gas temperature decreases accordingly, which results in a decrease of c_s and therefore an increase in M_a, as indicated in Fig.3.12. Actually the adiabatic expansion does not hold when the gas volume increases enough and the frequency of atomic collisions is too low, so there is a terminal value of the temperature and the velocity of the gas flow, v_∞ and T_∞. v_∞ is given as

$$v_\infty = \sqrt{\frac{2(C_P - C_V)}{m}\frac{\gamma}{\gamma-1}T_0}, \tag{3-16}$$

and T_∞ is empirically given as a function of P_0, T_0, and the nozzle diameter d:

$$T_\infty = K(P_0 d)^{-4/5} T_0^{9/5}, \tag{3-17}$$

where K is a specific constant dependent on the gas species. v_∞ is useful to calculate gas or cluster flight times as $t_{flight} = D/v_\infty$, where D is the flight length and often set as the distance between the nozzle orifice and the interaction point between the gas jet and another incident beam.

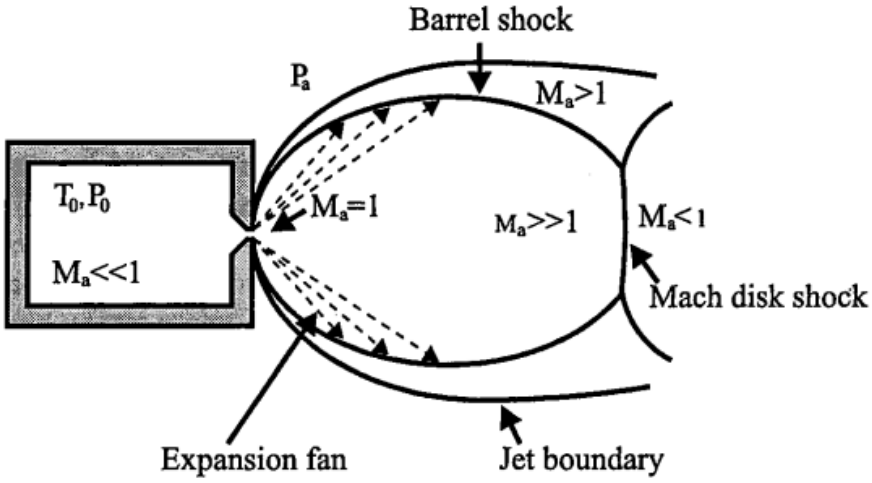

Figure 3.12: A schematic of a supersonic gas expansion into the vacuum. The gas is stored in a reservoir at pressure p_0, temperature T_0, and the speed of the gas is thermally distributed ($M_a \ll 1$). As the gas enters the nozzle area, it is accelerated to the speed of sound ($M_a = 1$) and as the gas expands, the temperature T drops altering the speed of sound such that the gas now travels supersonically ($M_a \gg 1$). From [102]. Reprinted with permission of Springer Nature.

Mach disk and experimental consideration

The appearance of the supersonic jet stream, as shown in Fig. 3.12, is also important for the experimental aspect of introducing samples to the interaction region. After the gas stream exits the nozzle, M_a increases to some value much larger than 1. The region where $M_a \gg 1$ is referred to as "a zone of silence", where the gas flow is not influenced by other particles or boundary conditions. At the borders of the zone of silence, the pressure inside the zone of silence is lower than the outside pressure, and the recompression of the expanding flow by oblique shock waves at the border (called "barrel shock") occurs. Especially the front side of the boundary is called "Mach disk" and the Mach disk must be distant from the exit of the nozzle enough so that the clustering of gaseous atoms and its transport to the reaction region is achieved without any disturbance by the shock waves at the boundary. The distance from the nozzle to the Mach disk has been investigated experimentally and can be given as the following analytic form [108]:

$$\frac{x_{MD}}{d} = 0.67\sqrt{\frac{p_0}{p_b}}. \tag{3-18}$$

This shows that the backing pressure must be enough low compared to the stagnation pressure so that the cluster jet is introduced to the reaction region. For experiments, one can decrease p_b by separating the region of jet expansion into separately pumped compartments with skimmers at their interfaces. This differential pumping scheme is also adopted to the experimental chambers used in the experiments for this work.

3.3.3 Scaling law

It has been studied well and known that the average cluster size is strongly dependent on the gas type, P_0, T_0 and the shape of a nozzle (especially its diameter). There is an empirical scaling law found by Hagena and his collaborators [109–111] which makes it easy to estimate the mean cluster size. The scaling parameter Γ^* is given by the following formula:

$$\Gamma^* = K_{gas} T_0^{0.25 q_{gas} - 1.5} p_0 d_{eq}^{q_{gas}}. \tag{3-19}$$

In Eq. 3-19, K_{gas} is a characteristic constant specific to the element of the gas. K_{gas} for some rare gases are shown in Tab. 3.4. q_{gas} is an exponent value specific to the gas species and varies between 0.5 and 1. According to the experiments by Hagena et al. [109–111], q_{gas} is usually set to 0.85. d_{eq} is the equivalent nozzle diameter for sonic nozzles. For conical nozzles, d_{eq} can be written as [108]

$$d_{eq} = 0.74 \frac{d}{\tan \alpha}, \tag{3-20}$$

where α is the half-opening angle of the nozzle. The relation between the mean cluster size $\langle N \rangle$ and Γ^* is known to be the following [108, 112, 113]:

$$\langle N \rangle = \begin{cases} \text{no cluster formation is observed} & (\Gamma^* < 350) \\ 38.4 \left(\frac{\Gamma^*}{1000} \right)^{1.64} & (350 < \Gamma^* < 1800) \\ 33 \left(\frac{\Gamma^*}{1000} \right)^{2.35} & (1800 < \Gamma^* < 10^4) \\ 100 \left(\frac{\Gamma^*}{1000} \right)^{1.8} & (10^4 < \Gamma^* < 10^6) \end{cases} \tag{3-21}$$

For $\Gamma^* > 10^6$, the formula $\langle N \rangle = 33 \left(\frac{\Gamma^*}{1000} \right)^{2.35}$ is suggested again [108, 114].

Table 3.4: Characteristic constant of rare gas atoms. From [115]. Reprinted with permission from AIP Publishing.

Element	Helium	Neon	Argon	Krypton	Xenon
K_{gas}	3.85	185	1646	2980	5554

Cluster size distribution

In general, a supersonic expansion technique creates clusters of different sizes and structural isomers. It has been reported in some investigations [116–118] that clusters generated solely through monomer addition follow a size distribution of exponential decay, while that larger clusters generated by

cluster-cluster coagulation follow a log-normal distribution as shown in Fig. 3.13. The formula of a log-normal distribution is as follows:

$$f(N) = \frac{1}{N\sigma\sqrt{2\pi}} \exp\left[-\frac{(\ln N - \mu)^2}{2\sigma^2}\right], \tag{3-22}$$

where μ, σ correspond to the mean and standard deviation of the distribution curve, respectively. With these parameters, the mean cluster size $\langle N \rangle$ and its standard deviation S can be given as follows:

$$\langle N \rangle = \exp(\mu + \sigma^2/2), \; S = \langle N \rangle \sqrt{\exp(\sigma^2) - 1}. \tag{3-23}$$

The size distribution can be an experimental challenge to resolve, especially for investigating size-dependent effects. Electron diffraction techniques [119] have been used to determine $\langle N \rangle$, mean temperature, and mean geometry of the ensemble of clusters. As FELs have been available now, one can determine the size and structure of a single particle from a diffraction image [44, 45, 47, 48].

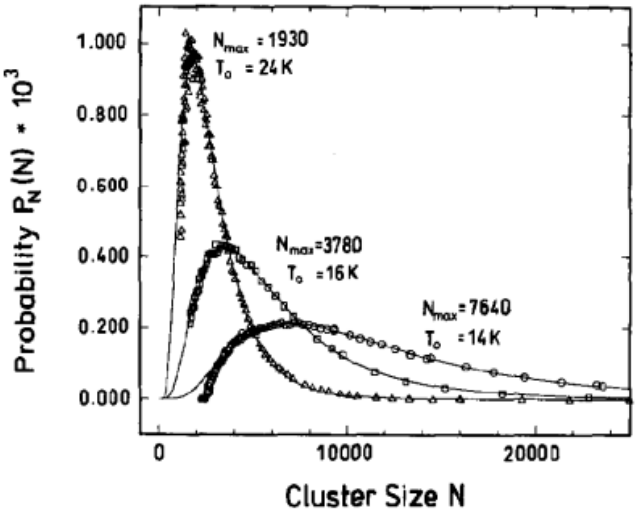

Figure 3.13: Experimentally observed distributions of cluster sizes. Adapted from [118]. Reprinted with permission from Elsevier.

Conversion from clsuter size to cluster radius

In this work, $\langle N \rangle$ is often converted into the radius of a cluster, r_0. For the conversion, the expression using the Wigner-Seitz radius r_s is a good approximation [120]. r_s is given by

$$r_s = \left(\frac{3M_{mol}}{4\pi\rho N_A}\right)^{1/3}, \tag{3-24}$$

where M_{mol} is the molar mass, ρ is the mass density, and N_A is the Avogadro number. r_s is typically given in the unit of Å. In the assumption that clusters are symmetric in 3D, the cluster radius can be described as

$$r_0 = r_s \langle N \rangle^{1/3}. \tag{3-25}$$

3.3.4 A pulsed cluster jet source

At the end of this section, an experimental consideration for cluster generation is introduced. It is important to introduce less than one cluster in the FEL focal volume to achieve a single-shot single-particle condition suitable for CDI measurements of single nanoparticles. As described in the previous subsections, it is also important to increase the degree of vacuum, i.e. to reduce p_b, so that clusters can be generated and introduced to the reaction point. To achieve these conditions, pulsed jet sources are often used owing to their following features:

- They can generate a gas jet pulse with low volume, which makes a high-vacuum condition as well as sample consumption lower than continuum sources.
- The timing of injecting a jet pulse is adjustable electrically, that is, the injecting timing can be synchronized with the timing of FEL shots.

In the experiments carried out in this work, pulsed solenoid valves were used to generate a pulse jet beam. The left panel of Fig. 3.14 shows a schematic of a pulsed valve (Parker Series 99) which was used in this work. The valve has a magnetic cylinder surrounded by a solenoid coil and a poppet in the cylinder normally closes the orifice of the valve. When applying a voltage to the solenoid coil, the magnetic cylinder is pulled back and the poppet gets away from the orifice, leading to the introduction of the gas jet. With this mechanism, this valve can generate a pulsed jet beam by application of pulsed voltage to the solenoid coil. For generating larger clusters efficiently, a convergent-divergent nozzle[4] was mounted on the orifice side of the valve. A schematic of the convergent-divergent nozzle is shown in the right panel of Fig. 3.14.

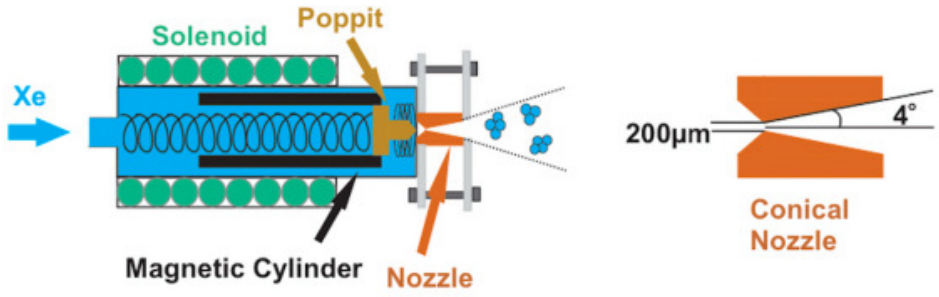

Figure 3.14: Schematics of a solenoid pulse valve and an attachment nozzle. From [62], licensed under CC BY-NC 3.0.

From the experimental investigation, the scaling law holds in the case of clustering in the adiabatic expansion of a steady flow [108]. On the other hand, a recent experiment [47] using a pulsed valve for cluster generation has observed that there are clusters generated in the "afterpulse" following the main jet pulse introduced by a pulsed valve and that the clusters in the afterpulse have the size

[4] A convergent-divergent nozzle is often referred to as a conical nozzle.

much beyond the predicted size with the scaling law. This is thought to be due to a certain effect occuring at the timing of the closing of the valve [47].

3.4 Ion time-of-flight spectrometer

Ion time-of-flight (TOF) spectroscopy has been widely used to study the dynamics of laser–matter interaction. In this section, the principle of the ion TOF spectroscopy is introduced.

3.4.1 Principle of the ion time-of-flight spectroscopy

Firstly, consider an ion with the mass of m and the charge of q under a constant electric field $\mathbf{E}$. The acceleration that the ion feels is given by $\mathbf{a} = (q/m)\mathbf{E}$ according to the equation of motion. When this ion has the zero initial velocity and moves a distance L in the direction of $\mathbf{E}$, then the elapsed time is

$$t = \frac{L}{v} = \frac{L}{2V}\sqrt{\frac{m}{q}}, \tag{3-26}$$

where V is the voltage between the start position and the goal position distant from the start position by L. Eq. 3-26 shows that the ratio m/q can be determined by measuring the TOF between two distant points under some electric field.

Further, assume that ions have positive charges, and consider a simplified TOF spectrometer shown in Fig. 3.15, which consists of the followings:

- a pusher: an electrode to which a voltage is applied to push the positively charged ions towards a detector,
- an extractor: an electrode to which a voltage lower than that applied to the pusher is applied,
- a drift tube: a tube having zero voltage, and
- a detector.

TOF spectrometers with this configuration are known as Wiley-McLaren-type spectrometers [121] and the spectrometer used in the second experiment for this thesis has a similar configuration (see chapter 5). Assume that the electric field between the pusher and the extractor and the field between the extractor and the tube is constant and their direction is perpendicular to the electrode. The kinetic energy of the ion with initial velocity $\mathbf{v} = (v_{x,0}, 0, 0)$ is given by the following:

$$K(x) = \begin{cases} \frac{mv_{x,0}^2}{2} + qxE_s & (0 \le x < s) \\ \frac{mv_{x,0}^2}{2} + qsE_s + q(x-s)E_d & (s \le x < s+d) \\ \frac{mv_{x,0}^2}{2} + qsE_s + qdE_d & (s+d \le x < s+d+L) \end{cases} \tag{3-27}$$

Using these and the formula of the x component of the speed $v_x = \sqrt{2K(x)/m}$, the TOF of the ion from the starting point S to the detection point G on the detector can be calculated analytically

and given by the following:

$$T_{S\to G} = t_s + t_d + t_L \tag{3-28}$$

$$t_s = \int_0^s \frac{\mathrm{d}x}{v_x(x)} = \sqrt{\frac{2m}{q}}\sqrt{\frac{s}{E_s + v_{x,0}^2/2q}} \tag{3-29}$$

$$t_d = \int_s^{s+d} \frac{\mathrm{d}x}{v_x(x)} = \sqrt{\frac{2m}{q}}\left(\frac{\sqrt{sE_s + dE_d + v_{x,0}^2/2q} - \sqrt{sE_s + v_{x,0}^2/2q}}{E_d}\right) \tag{3-30}$$

$$t_L = \int_{s+d}^{s+d+L} \frac{\mathrm{d}x}{v_x(x)} = \frac{1}{2}\sqrt{\frac{2m}{q}}\frac{L}{\sqrt{sE_s + dE_d + v_{x,0}^2/2q}} \tag{3-31}$$

These formulas indicate that the initial position s has less effect on the total TOF when the electric field between the extractor and the tube is stronger than that between the pusher and the extractor.

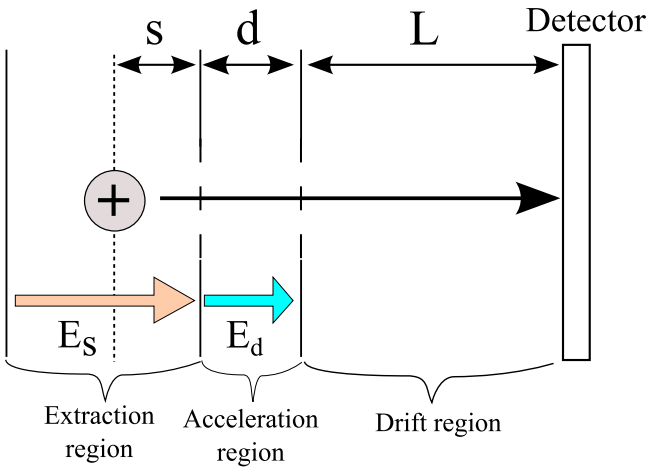

Figure 3.15: A schematic diagram of a test TOF spectrometer.

In practice, more sophisticated spectrometers have been used for TOF measurement and the TOF is much more difficult to calculate analytically. Some simulation tools such as SIMION [122, 123] are used to simulate trajectories of ions in the designed spectrometers.

3.5 X-ray photon detector (MPCCD sensor)

In general, when a photon is absorbed by a semiconductor part of a charge-coupled device (CCD) element, the photon creates charges in the element. The number of those charges reflects the photon energy of the absorbed photon, so one can obtain the photon energy of the absorbed photon by reading the charges from the CCD element.

MPCCD sensors [124] have recently developed for experiments using XFEL pulses at SACLA. An MPCCD module consists of 8 arrays of CCD elements, each of which is a metal-oxide insulator (MOS). An MPCCD module is designed to be used in experiments using XFEL pulses and has the following features:

- It has high sensitivity (quantum efficiency) in the X-ray regime, as shown in Fig. 3.16(a).
- It has 8 ports for 1 array of CCD elements to read out generated charges from, which allows a high-speed readout and therefore high-frequency measurements.

The specification and the typical performance of an MPCCD module are shown in Tab. 3.5.

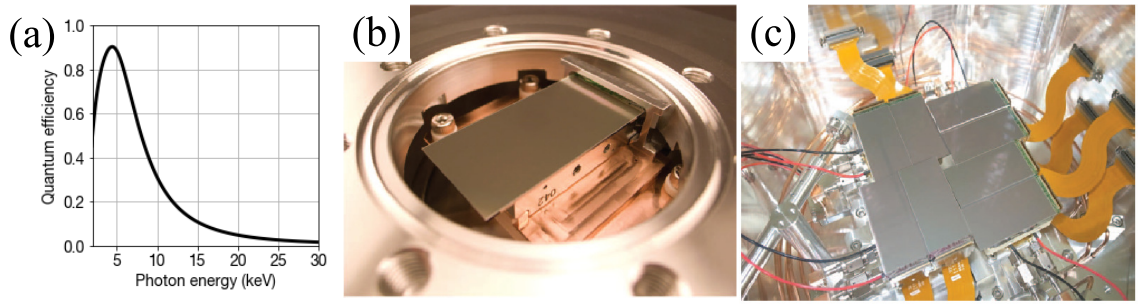

Figure 3.16: Quantum efficiency and photographs of MPCCD sensors. (a) Typical quantum efficiency of MPCCD. The dataset for visualization was a courtesy of T. Kameshima. (b) Design of a single MPCCD sensor. The detection area is 25.4×51.2 mm^2. From [124]. (c) Design of an octal MPCCD sensor. The detection area is around 102×102 mm^2. From [124]. (b) and (c) are reprinted with permission from AIP Publishing.

The raw signal of the MPCCD sensor, here called "CCD count," has the unit of digital number (DN). The number of detected photons can be calculated by using the following relation:

$$N_{photon} = \frac{(CCD\ count) \times Gain}{h\nu/\epsilon}, \tag{3-32}$$

where $Gain$ is the system gain of the MPCCD sensor (in the unit of 1/DN), $h\nu$ is the photon energy of detected photons (eV), and ϵ is the energy required to generate an electron-hole pair in the component semiconductor (eV). Since the CCD elements are composed of Si, $\epsilon = 3.65$ eV.

Table 3.5: Specification and typical performance of an MPCCD module. From [124]. Reprinted with permission from AIP Publishing.

Specification		
Description	Parameters	Unit
Pixel size	50×50	μm
Pixel number	1024× 512	N/A
Imaging area	51.2 × 25.6	mm^2
Sensing material	Epitaxial silicon	N/A
Sensing layer thickness	50	μm
Sensor structure	Front-illumination	N/A
Image format	Full frame transfer	N/A
Operation temperature	0 to −30	°C
Quantum efficiency	80	% at 6 keV
	20	at 12 keV
Max. frame rate in un-binned mode	60	Hz
Max. pixel readout speed	5.4	MHz
Readout port	8	N/A
Typical performance		
Description	Parameters	Unit
System noise	100-250	e- rms
Peak signal	2500-3000	photons/pixel with 6 keV X-ray
	4.1-5.0	Me-/pixel
Radiation hardness	>3.2 ×10^{14}	photons/mm^2 with 12 keV X-ray
Frame rate	30	Hz
Pixel readout speed	3.3	MHz
Dark signal	600	ke-/pixel/s at 293 K

3.6 Signal and data processing

3.6.1 Timing chart

A time chart of the signals used in the experiments is shown in Fig. 3.17. The master oscillator installed to SACLA generates master signals, which determines the repetition rate of the XFEL beam. The XFEL shots are triggered by signals delayed to the master signals by 15.3 ms. The timing of the valve opening is adjusted for purposes specific to each experiment.

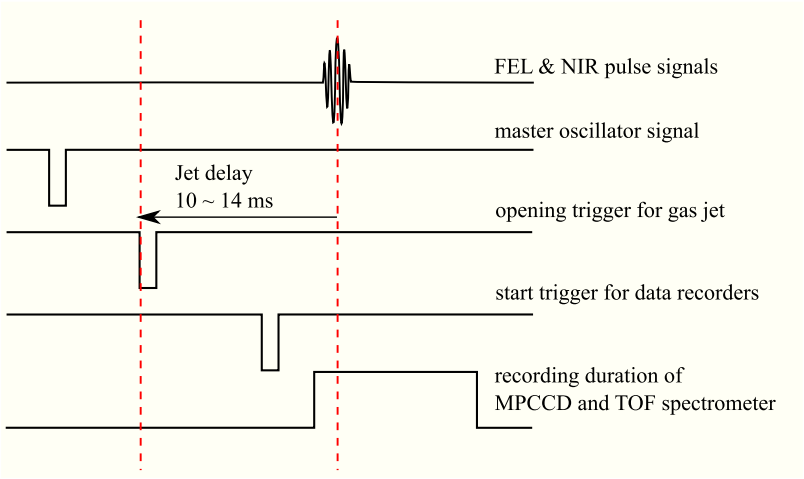

Figure 3.17: A timing chart of the trigger, the cluster jet pulses, the XFEL pulses and the NIR pulses.

3.6.2 Configuration of the data acquisition system

The configuration of the data acquisition system used in the experiments is depicted in Fig. 3.18. Scattering signals were collected by the single and octal MPCCD sensors and stored in the storage of SACLA. The ion signals collected by the ion TOF spectrometer were stored in the prepared storage or the storage of the SACLA high-performance computing (HPC) server. In the time-resolved experiment for this work, images collected by the arrival timing monitor were also stored in storage of SACLA HPC server. For each FEL shot, signals were linked with a tag number, which is the number delivered from the facility to identify each FEL shot. The extracted data were put together into a database for analysis to access them easily.

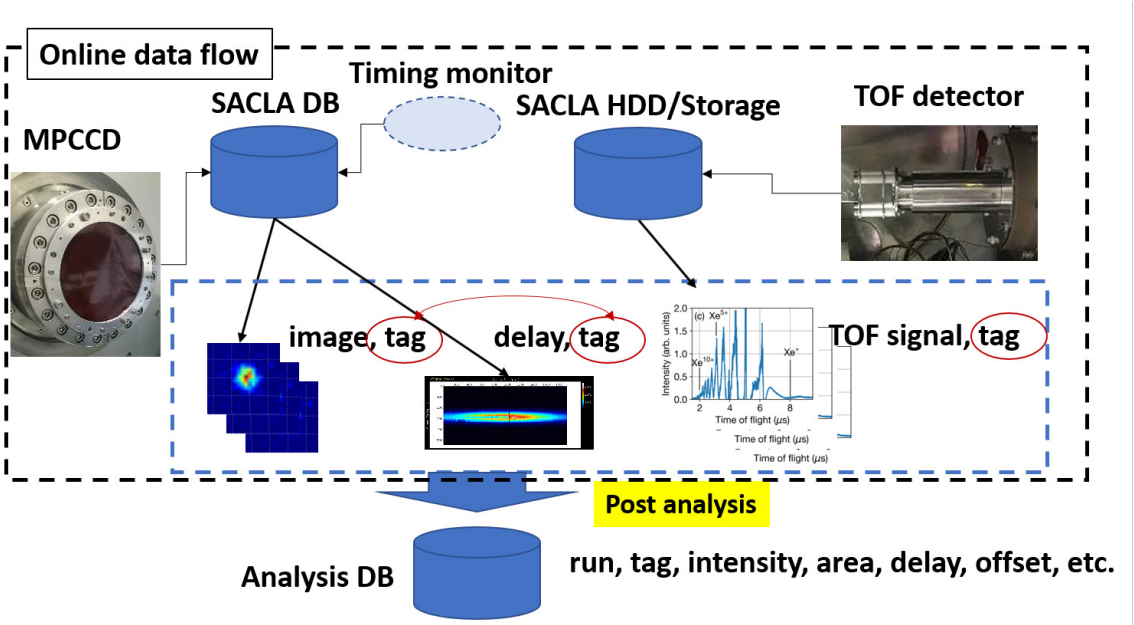

Figure 3.18: A schematic of data flow. During the measurements, signals collected by the octal MPCCD sensor were stored in the database constructed in the SACLA facility. Ion signals were collected by the spectrometer and stored in our storage or the storage of the SACLA HPC server. Scattering signals and the images of the arrival timing monitor for each FEL shot were linked to each other with single tag numbers. The observables extracted from the signals were put together into a database for analysis.

Chapter 4

Results and discussion I: Multi-spectroscopic study of single Xe clusters using XFEL pulses

We present the results of multispectroscopy of xenon cluster [125] in this chapter. XFELs deliver ultrashort coherent laser pulses in the X-ray regime enabling investigation of the structure of nano-scale samples in the particle-by-particle scheme. The XFEL-based X-ray diffraction technique can provide a size- and structure-selective evaluation of the light–matter interaction processes when combined with other spectroscopic methods. This combined technique has the possibility to give the insight into light-matter interaction on the level inaccessible in the traditional experimental schemes. In this study, single-shot SAXS measurements combined with fluorescence and ion TOF spectroscopies by using XFEL pulses provided from SACLA were demonstrated. The experimental methods, procedures of data processing and analysis, and the findings are detailed below.

4.1 Experimental setups

The experiment in this study was carried out at EH3 of BL3 [97] of SACLA [90]. The experimental setups are summarized in Fig. 4.1. Fig. 4.2 shows a photograph of the experimental apparatus in EH3. This experimental system was composed of the following apparatuses.

- XFEL source: SACLA
- Cluster source: a pulsed cluster jet generator
- Ion detector: an ion time-of-flight spectrometer
- Photon detector: MPCCD sensors

Specific parameters of this experiment are described in this section.

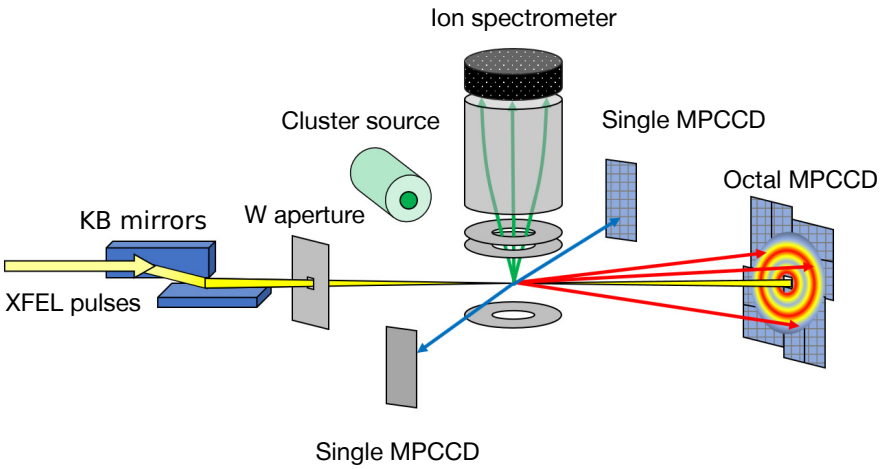

Figure 4.1: A schematic diagram of the experimental setup used in the first experiment. XFEL pulses were focused by a pair of KB mirrors. The cluster beam was generated through adiabatic expansion and introduced through two skimmers to the reaction point. The scattered photons were collected by an octal MPCCD sensor installed 1,500 mm from the reaction point in the direction of XFEL beam. Fluorescence photons were detected by two single MPCCD sensors, whose distances from the reaction point were 600 mm and 800 mm, respectively. Ions were collected by an ion TOF spectrometer, set on the upper side of the chamber. From [125], licensed under CC BY 4.0.

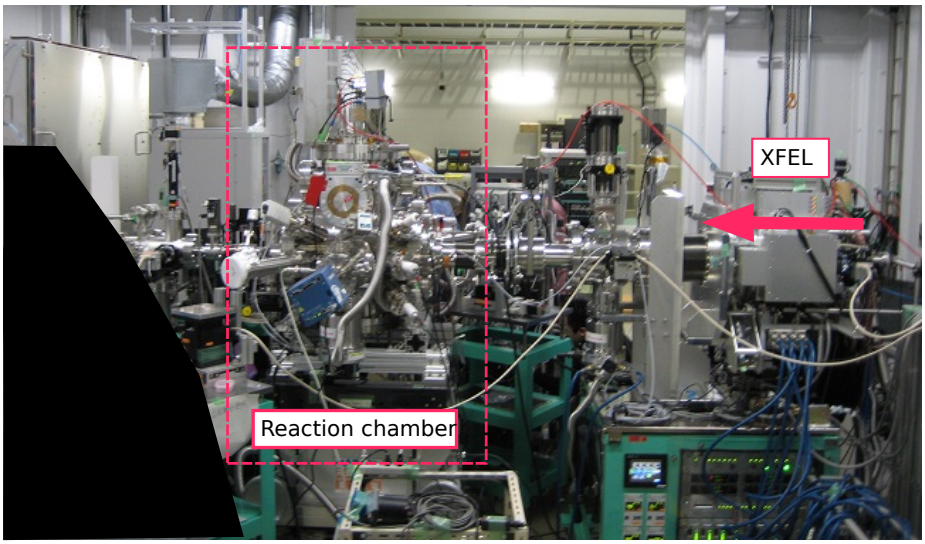

Figure 4.2: A photograph of the entire apparatuses. An ion time-of-flight spectrometer was installed vertically in a chamber (reaction chamber). The reaction chamber was set on the downstream of the XFEL path. Another chamber equipped with a pulsed gas jet source was connected to the reaction chamber so that the direction of the gas jet beam was perpendicular to that of the XFEL pulses.

4.1.1 XFEL pulses and X-ray optics

XFEL pulses were focused by the KB mirror system to 1.5×1.3 μm (vertical & horizontal directions, FWHM). We adopted 5.5 keV for X-ray photon energy slightly above the L-edge of the Xe atom. The photon energy of each XFEL pulse was measured by a spectrometer with a double-crystal monochromator system before the experiment. Fig. 4.3 shows the photon energy spectrum of XFEL pulses accumulated on several tens shots. The photon energy used in the experiment was estimated to be 5.48 keV by fitting this curve with a Gaussian function. The corresponding wavelength and wavenumber were 2.26 Å and 2.79 $Å^{-1}$, respectively. The averaged fluence of the XFEL pulses was determined to be 16 $\mu J \mu m^2$ from the observed diffraction patterns.

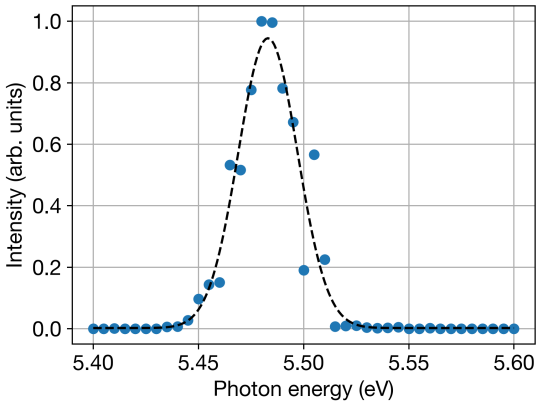

Figure 4.3: The photon energy spectrum of XFEL pulse measured for the experiment. The dashed line is a fitting curve and the resulting photon energy is 5.48 keV.

The KB mirror system often causes undesirable scattered light, so-called parasitic scattering, which is mainly due to unexpected scattering of the X-ray beam by the edge of the mirrors. The parasitic scattering is critical for CDI experiments because it causes artifacts on the detected signals. In this experiment, a pair of aperture plates made of tungsten and had square holes with different sizes was installed to the upstream side of the experimental chamber. The positions of the aperture plates were adjusted by monitoring the intensity of the parasitic scattering appearing on the octal MPCCD sensor.

A beam position monitor was put on a translator and installed to the reaction chamber so that the center of these elements could be moved to the designed reaction point. The Ce:YAG screen was used to adjust the position of the reaction chamber in order to overlap the designed reaction point with the XFEL focal point.

4.1.2 The cluster source

A cluster jet source was implemented with a pulse valve. Fig. 4.4 shows photographs of the cluster source used in this experiment. The cluster source shown in Fig. 4.4(a) has a pulse valve mount

made of copper (Cu) on a cold unit made by Oxford Instruments Corp. The opening of the solenoid valve is controlled by using a dedicated controller IOTA ONE. A convergent-divergent nozzle was mounted on the front plate of the solenoid valve with a support made of aluminum (Al), as shown in Fig. 4.4(b). An indium sheet gasket was inserted between the Cu nozzle and the pulse valve to ensure the gas sealing. The diameter and half angle of the nozzle are 200 μm and 4°, respectively. Liquid nitrogen was used as the refrigerant to cool the source. The duration of the pulsed gas beam was set to 1 ms and the repetition rate was set to 10 Hz to match that of the XFEL shots. The stagnation pressure was set to 21 bar and the stagnation temperature was set to 300 K (without cooling) and 250 K (with cooling).

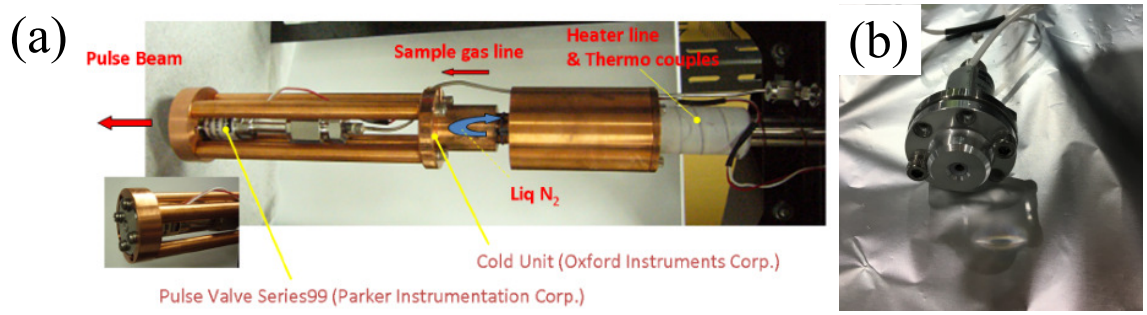

Figure 4.4: Cluster source. (a) A photograph of the cluster source used in the experiment. (b) A photograph of the top of the valve. A convergent-divergent nozzle was attached on the front plate of the solenoid valve via a sealing indium gasket and covered with an Al support to fix its position on the valve.

4.1.3 Experimental chamber

Our apparatus consists of three vacuum chambers, i.e. cluster source chamber, differential pumping chamber and reaction chamber (Fig. 4.5(a)). Fig. 4.6 shows a photograph of the source chamber. A cluster source is mounted on a motorized three-axis stage and installed in the cluster source chamber. The cluster beam passes two skimmers so that the core of the cluster jet can be delivered to the reaction point. Each vacuum chamber equipped with several pumps as shown in the schematic diagram (Fig. 4.5(b)) and Tab. 4.1. This configuration has enabled to keep the high vacuum during the experiment which is often essential for effective cluster generation. The pumping system could reduce the pressure in the cluster source chamber and the differential pumping chamber without gas load as low as 10^{-4} Pa and 10^{-5} Pa, respectively.

Table 4.1: Specification of vacuum pumps used in the experiment. The pumping speed is for N_2.

Chamber	TMPs	Roughing pumps
Cluster source	Pfeiffer HiPace 700 (685 L/s) × 1 Priffer TMU 521 (510 L/s) × 2	ULVAC DIS-500 (10 L/s) × 1
Differential pumping	Edwards STP-iX455 (450 L/s) × 2	Common to Cluster source
Reaction	Pfeiffer HiPace 700 (685 L/s) × 1 Edwards STP-301 (300 L/s) × 1	Busch FO-0030 (10 L/s)

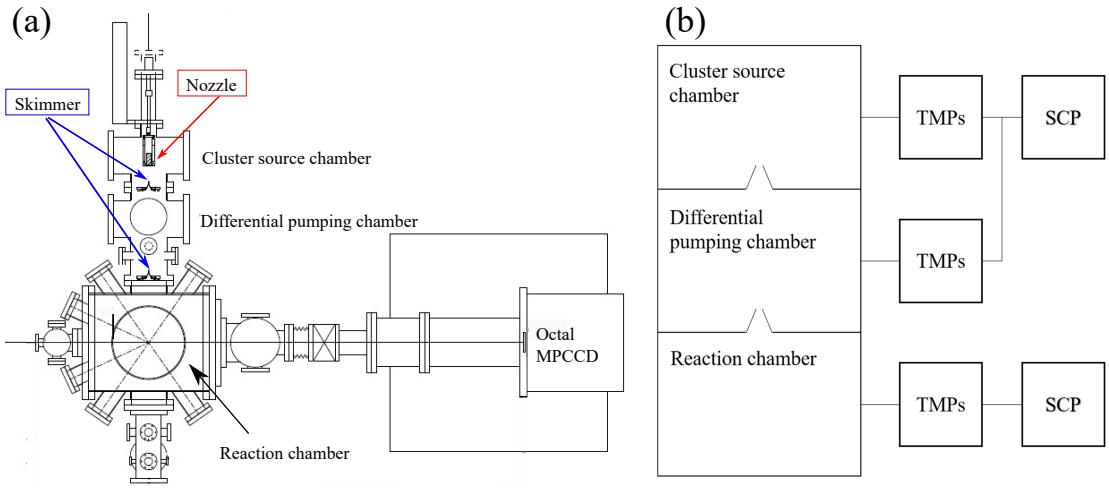

Figure 4.5: Schematics of the chambers and the pumping system. These are courtesy of K. Nagaya. (a) A schematic of the chambers. The source chamber is composed of two parts for differential pumping. A skimmer with a diameter of 0.5 mm was set to the interface between the cluster source chamber, and a skimmer with a diameter of 1.0 mm was set to the interface between the differential chamber and the reaction chamber. The cluster source was installed so that its top was a few tens mm distant from the cusp of the first skimmer. (b) A schematic of the pumping system.

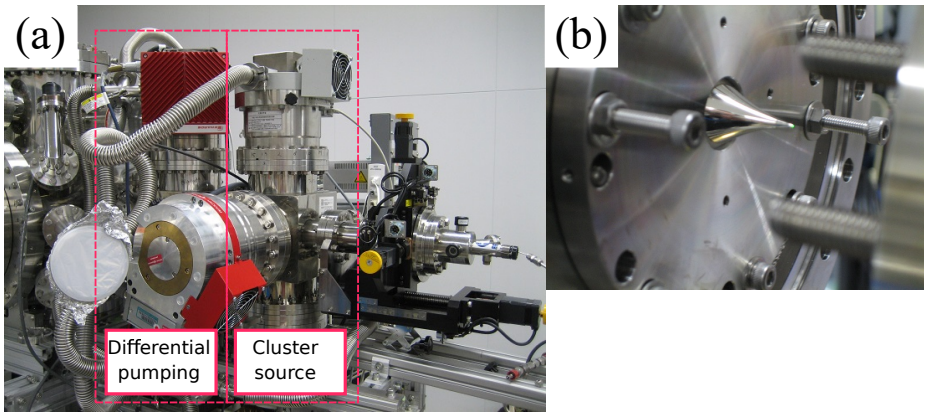

Figure 4.6: Photographs of the source chamber (a) and the second skimmer (b). The second skimmer was installed to the interface between the differential pumping chamber and the reaction chamber.

4.1.4 Adjustment of the position and timing

The position of the reaction chamber was adjusted coarsely by using the three-axis stage under the chamber so that the designed reaction point and the focal point of incident XFEL pulses were overlapped. The position of the cluster source was aligned by the motorized translator so that the core of the cluster jet could be introduced to the reaction point in the reaction chamber. To achieve this condition, a quadrupole mass spectrometer (QMS), which is named microvision2 and made by MKS Corp., was set on the downstream of the gas jet and the volume of gas jet reaching the mass spectrometer was monitored. The position of the gas jet was determined by using Ar gas and by maximizing the yields of dimers and trimers detected by the QMS. The final distance between the nozzle and the top of the first skimmer was set to around 25 mm.

4.1.5 Ion TOF spectrometer

The ion TOF spectrometer used in the experiment is shown in Fig. 4.7. This spectrometer has five electrodes (U1, U2, U3, D1, and D2), and two detectors (HEX 80) made by RoentDek Handels GmbH. The detectors are composed of a micro-channel plate (MCP) and a delay-line anode and suitable for detection of charged particles. The reaction point was the center of the region between the two electrodes U1 and D1. Generated ions were extracted toward the upper detector along the electron field generated by applying the voltages to the electrodes. The applied voltages are listed in Tab. 4.2. When ions are detected by HEX 80, the voltage applied to HEX 80 is changed depending on the intensity of the ion signal. For each XFEL shot, the voltage applied to HEX 80 was recorded by a high-speed digitizer (Acqiris DC282) made by Agilent Technologies.

Table 4.2: List of the voltages applied to the electrodes and the detector.

Parameter	HEX 80	U3	U2	U1	D1	D2
Voltage [V]	-1,800	0	1,000	1,500	2,000	2,750

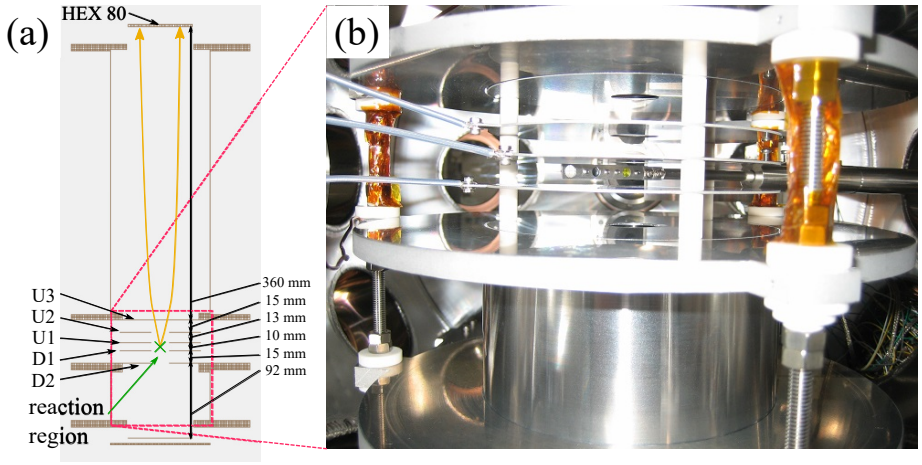

Figure 4.7: Ion TOF spectrometer. (a) A schematic of the ion TOF spectrometer. Voltages were applied independently to the five electrodes and HEX 80. Ions generated were extracted to HEX 80 installed to the upper side of the spectrometer. (b) A photograph of the reaction region. Each electrode was insulated to each other by ceramic spacers. The position monitor showing up in (b) has targets for adjusting the position of the reaction chamber.

4.1.6 MPCCD

An octal MPCCD sensor was installed at the downstream side of FEL and recorded SAXS signals. The distance of the octal MPCCD sensor from the reaction point was 1,500 mm. The size of the center hole of the MPCCD sensor was adjusted to avoid the direct beam of FEL. With this setup, the detector covered a scattering angle range of 0.10–2.8°, which corresponds to a momentum transfer of $q = 0.049$–1.4 nm^{-1}. Two single MPCCD sensors were set in front of two viewports of the reaction chamber. The distances of the single MPCCD sensors from the reaction point were 600 mm and 800 mm, respectively. The SAXS and fluorescence signals detected by the MPCCD sensors were stored in the storage of the SACLA HPC server.

4.1.7 Experimental parameters

At the end of this section, the experimental parameters are shown in Tab. 4.3.

Table 4.3: List of experimental parameters. Single MPCCD sensors are numbered for convenience. The peak fluence of XFEL pulses was estimated by analyzing the obtained SAXS images.

Cluster source	
Gas	Xenon
Stagnation pressure [bar]	~ 21
Stagnation temperature [K]	~ 300
(cooling)	~ 250
Pulsed valve	
Nozzle diameter [μm]	200
Nozzle half angle [degree]	4
Pulse duration [ms]	1.0
Jet delay [ms] (Xe atom)	13.3
(main pulse)	12.3
(after-pulse region)	10.3

XFEL	
Photon energy [keV]	5.548
Repetition rate[Hz]	10
Pulse duration [fs]	~ 10
Focus [μm^2, FWHM]	1.5×1.3
Peak fluence [μJ/μm^2]	~ 16
Ion TOF spectrometer	
HEX 80 [V]	-1,800
U_3 [V]	0
U_2 [V]	1,000
U_1 [V]	1,500
D_1 [V]	2,000
D_2 [V]	2,750
MPCCD sensor	
System gain [eV] (Octal)	17.38
(Single 1)	17.74
(Single 2)	19.05
Energy to generate an electron-hole pair [eV]	3.65

4.2 Preprocessing of experimental data

4.2.1 Extraction of "hit" images

Totally 90,225 images were recorded in the experiment. At the first stage of analysis, the "hit" images, where signals from the clusters show up, were chosen by the following procedure:

1. The number of pixels that had digital number (DN) above a threshold and in the specific region, N_{over}, was calculated.

2. The images where the ratio of N_{over} to the total number of the target pixels N_{tpix} was above another threshold were chosen as candidates for the hit images.

3. The final hit images were selected from all the candidate images by checking with the eyes and by applying a fitting to the radial profiles of images, which will be described in the following section.

Fig. 4.8(a) shows a typical DN distribution of an octal MPCCD image. The pixels in an 800×800-pixel square around the center of the image and out of the center blank of the image were analyzed for the thresholding. The threshold to DN was set to 85, corresponding to 1 photon. Fig. 4.8(b) shows the ratio of N_{over} to N_{tpix}. The threshold to the ratio was set to 0.01 (1 %). The number of the hit images was 81, and the resulting hit ratio, defined by the ratio of the number of the hit images to the total number of the collected images, was 0.09 %.

During the experiment, three conditions for cluster generation were used: the normal pulse timing at 300 K, the after-pulse timing (see section 3.3.4) at 300 K, and the normal pulse timing at 250 K. The statistics of hit images are shown in Tab. 4.4. Most of the hit images were obtained by using the after-pulse timing condition.

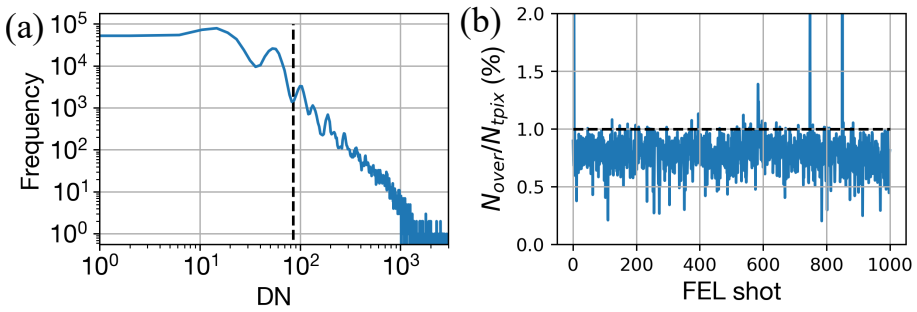

Figure 4.8: (a) A typical DN distribution of the target pixels. The dashed line corresponds to the threshold. (b) The ratio of N_{over} to N_{tpix} for sequential 1,000 FEL shots. The dashed line corresponds to the threshold.

Table 4.4: The statistics of the SAXS images having the signals from clusters.

Normal pulse timing, 300 K	After-pulse timing, 300 K	Normal pulse timing, 250 K	Total hits	Total FEL shots
1	69	11	81	90,225

4.2.2 Correction of baseline of MPCCD sensors

Images obtained from the MPCCD sensors had background due to the dark current of each CCD element [124], as well as photons from the parasitic scattering, as shown in Fig. 4.9(b). To extract the signals coming from the clusters, the following steps were applied to the collected images:

1. A background image for a hit image was calculated by averaging over the images with tag numbers near the tag number of the hit image. The background image and the hit image are linked together with the tag number.

2. A signal from clusters was obtained by subtracting the background image from the hit image.

Fig. 4.9(b)-(c) show the background image for the image shown in Fig. 4.9(a) and the background-subtracted image, respectively. Each background image was obtained from almost 1,000 images.

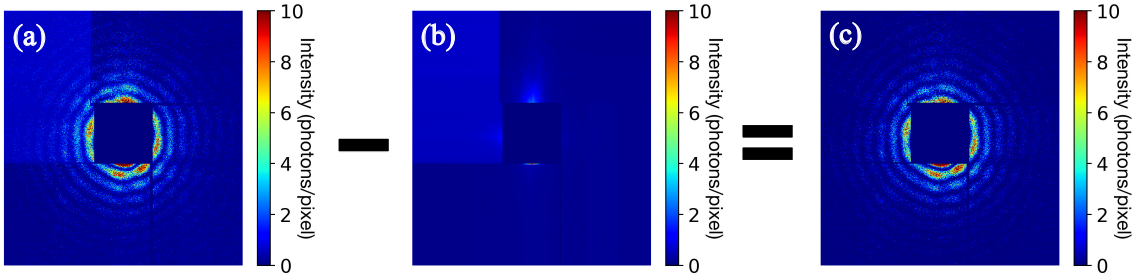

Figure 4.9: A schematic of the procedure for baseline correction of the MPCCD images. (a) Raw images had baselines coming from the dark current of each CCD element, which could influence the data analysis. (b) Background images were calculated by averaging over the images with tag numbers near the tag number of each hit image. (c) The background-subtracted images are free from the non-signal background and the different baseline levels of CCD elements. All the images are shown in the same color scale.

4.2.3 Background correction of fluorescence spectra

As for single MPCCD sensors, after the baseline correction, a background histogram of CCD count was subtracted from the signal histogram in order to calculate the number and the photon energy of fluorescence photons. For a specific image with signals from clusters, the background histogram was calculated by averaging the histograms of CCD count from images measured at shots close to the shot where the signal image was measured. Fig. 4.10 shows an example of raw histograms and background spectra. The background histogram had the mean of 0 keV and the standard deviation of 0.5 keV.

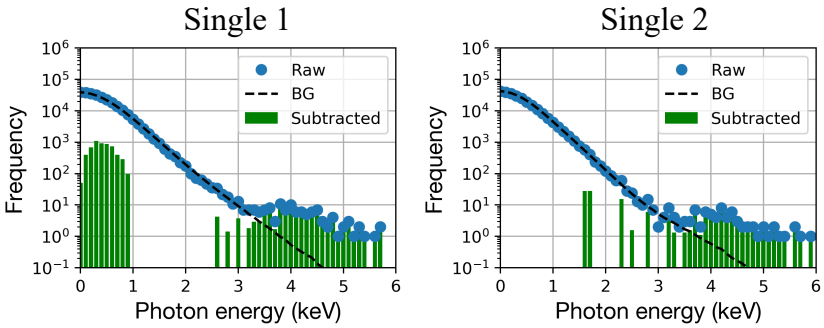

Figure 4.10: Typical histograms of CCD count of images of single MPCCD sensors. The corresponding background spectra were plotted with black dashed lines. The background-subtracted histograms are plotted with green bars.

4.2.4 Baseline correction of TOF spectra

When a large number of ions is detected by the spectrometer, the following problems could occur:

- The baseline of the TOF spectrum is modulated.
- The detection efficiency of the spectrometer gets lower.
- The signal intensity is saturated, i.e., the signal intensity reaches the upper limit of the detectable range of the digitizer.

Modulation of the baseline could lead to the undershoot and overshoot of the signals against the detectable range of the digitizer, which makes the analysis of the TOF spectrum difficult. The baselines of each TOF spectrum were calculated by using a procedure that combines a moving average and a Savitzky-Golay filter [126].

Fig. 4.11(a) shows an example of observed the raw TOF spectra in light blue and the corresponding baseline in orange. Fig. 4.11(b) shows the baseline-corrected spectrum. The procedure successfully compensated the modulated baseline. In most of the collected TOF spectra, the signals of doubly charged Xe ions at ~ 5 μs and those of singly charged Xe ions at ~ 6 μs were crucially influenced by the saturation, undershoot of the baseline and the lowering of the detection efficiency. Hence, it is noted that the intensity of doubly/singly charged Xe ions were less reliable compared to highly charged Xe ions.

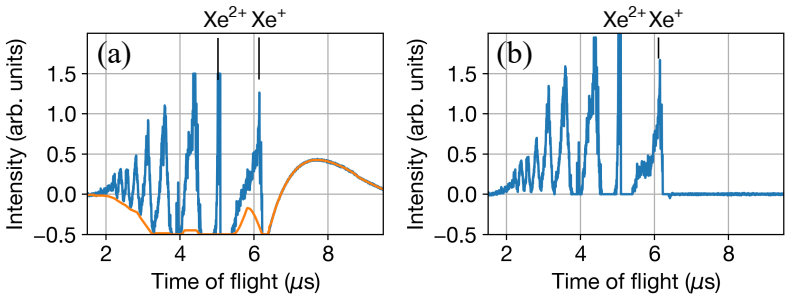

Figure 4.11: Baseline correction of ion TOF spectra. (a) A typical raw spectrum (light blue) and the corresponding baseline (orange). The baseline was calculated by using a smoothing method based on the moving average and used to compensate for the TOF spectrum. (b) The baseline-corrected TOF spectrum.

4.3 Analysis

4.3.1 Extraction of the cluster size and the FEL fluence

The recorded SAXS images suggest that most of the observed clusters had spherical shapes. Based on this fact, the clusters were assumed to be almost spherical and their radii and the fluences of the XFEL pulses at the actual reaction point were extracted from the SAXS images by the following procedure:

1. The center of the diffraction patterns was determined by maximizing Friedel centrosymmetry of the sum of the hit images.

2. The radial profiles of each image were calculated by the averaging in the angle direction around the determined center of the image.

3. FItting was applied to each radial profile.

Determination of the center of the diffraction patterns

Considering the discussion on scattering by an electron bound to an atom (subsection 2.1.1), the scattering of hard X-rays by Xe atoms can be described by Thomson scattering. The absorption efficiency of a 5.5-keV X-ray photon by a Xe atom is very low. Furthermore, the Ewald sphere is approximated as a plane in the detectable range of momentum transfer in the experiment because the maximum of the detectable momentum transfer (1.4 nm^{-1}) is quite lower than the wavenumber of the incident photons (27.9 nm^{-1}). Therefore, the scattered intensity can be considered to satisfy the Friedel centrosymmetry, $I(\mathbf{q}) = I(-\mathbf{q})$ [127].

Based on the discussion in Ref. [127], the Friedel centrosymmetry of the sum of the hit image was

evaluated by using correlation functions:

$$
\begin{aligned}
C_{sym}(x_0, y_0) &= \frac{E - O}{E + O} \\
E &= \sum_{x,y \in ROI_{sym}} \left[I_0(x, y) + I_{sym}(-x, -y; x_0, y_0) \right]^2 , \\
O &= \sum_{x,y \in ROI_{sym}} \left[I_0(x, y) - I_{sym}(-x, -y; x_0, y_0) \right]^2 ,
\end{aligned}
\tag{4-1}
$$

where x and y are the coordinates of the image, ROI_{sym} is the range of interest without the missing region of the detector (e.g. the center hole if the detector) for the calculation of C_{sym}, (x_0, y_0) is the coordinate of the center of the diffraction patterns (in the unit of pixel), and I_0 and I_{sym} are the observed diffraction intensity and its so-called Friedel mate, respectively. In this work the Friedel mate was given by $I_0(-(x - x_0), -(y - y0))$. The intensities of diffraction patterns were low and even the diffraction pattern with highest intensity had only ~ 10 photons/pixel at the center region of image. To get better statistics for calculation, C_{sym} of the sum of the hit images was calculated to determine the center of the diffraction patterns. Fig. 4.12(a) shows the image made by summing the hit images, and Fig. 4.12(b) shows the map of C_{sym} in the (x_0, y_0) space. Here a 400×400-pixels square region surrounding the center of the image was set as ROI_{sym}. The pair (x_0, y_0) which was around the center of CCD image and maximized C_{sym} was taken as the center of the diffraction patterns. The obtained values are $(-8.52, 7.44)$.

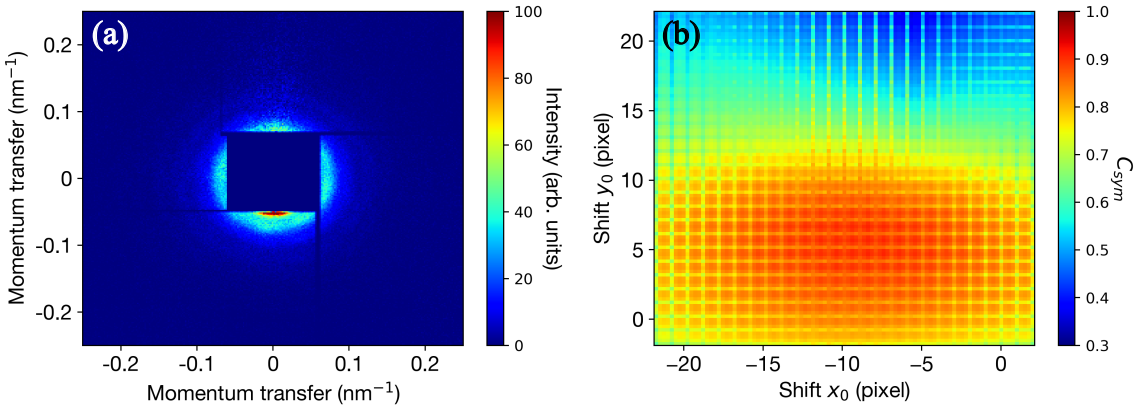

Figure 4.12: The summed-up diffraction image and a Friedel centrosymmetry map. (a) The image made by summing the hit images. (b) A map of C_{sym} in the (x_0, y_0) space.

Fitting to the radial profile

Fig. 4.13 shows a schematic of the detection of scattering photons by a planar detector. The solid angle at the coordinate (x_{pix}, y_{pix}) on the detector can be written by

$$
\mathrm{d}\Omega = \cos^3 2\theta \frac{A}{L^2}, \tag{4-2}
$$

where A is the area of a pixel, L is the distance of the detector from the reaction point (camera length), and (x_{pix}, y_{pix}) is related to the scattering angle θ:

$$2\theta = \tan^{-1}\frac{\sqrt{x_{pix}^2 + y_{pix}^2}}{L} = \tan^{-1}\frac{R_{pix}}{L}. \tag{4-3}$$

By substituting the solid angle in Eq. 2-44 and applying the azimuthal average, the number of scattered photons in the experimental setup can be formulated as follows:

$$\begin{aligned} N_s(R_{pix}; r_0, J_0) &= J_0 r_e^2 (3NZ)^2 \frac{1+\cos^2\{2\theta(R_{pix})\}}{2} \left[\frac{\sin\{q(\theta(R_{pix}))r_0\} - q(\theta(R_{pix}))r_0\cos\{q(\theta(R_{pix}))r_0\}}{\{q(\theta(R_{pix}))r_0\}^3}\right]^2 \\ &\quad \times \cos^3\{2\theta(R_{pix})\}\frac{A}{L^2}. \end{aligned} \tag{4-4}$$

The fitting function was based on Eq. 4-4 and the formula is

$$\begin{aligned} N_s(R_{pix}; r_0, K, base) &= K \frac{1+\cos^2\{2\theta(R_{pix})\}}{2} \left[\frac{\sin\{q(\theta(R_{pix}))r_0\} - q(\theta(R_{pix}))r_0\cos\{q(\theta(R_{pix}))r_0\}}{\{q(\theta(R_{pix}))r_0\}^3}\right]^2 \\ &\quad \times \frac{\cos^3\{2\theta(R_{pix})\}}{L^2} + base. \end{aligned} \tag{4-5}$$

In Eq. 4-5, the pre-factor and the pixel area A of Eq. 4-4 is put together into a parameter K, and *base* represents an uniform baseline coming from the residual background.

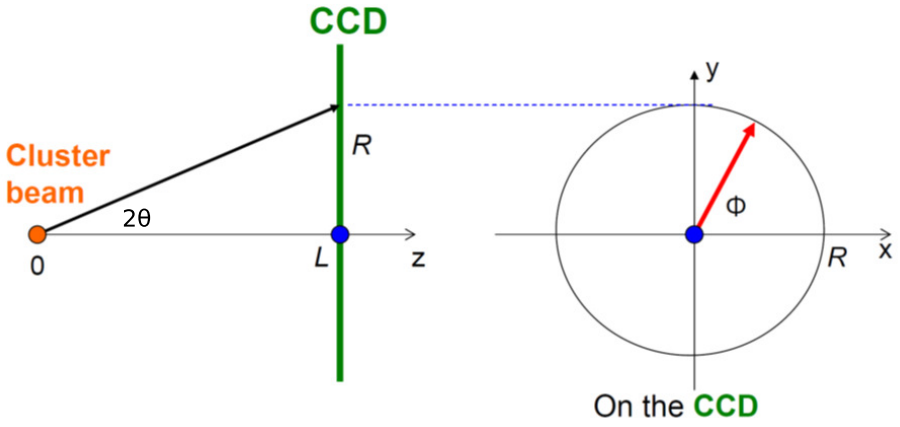

Figure 4.13: A schematic of detection of scattering photons by a planar detector. scattered photons in the direction characterized by (θ, ϕ) are detected by the detector pixel at (x_{pix}, y_{pix}).

Fig. 4.14 shows a schematic of the procedure of calculating the radial profiles. Diffraction images were projected into the polar coordinate, and the radial profiles were calculated by averaging the polar plot in terms of the angle direction. The cluster radii of each observed cluster and the FEL fluence were obtained by fitting to the radial profiles of the diffraction patterns with the curve expressed in Eq. 4-5. The total number of scattered photons can be calculated by using the fitting curve as follows:

$$N_{scat} = \sum_{x_{pix}, y_{pix}} N_s\left(\sqrt{x_{pix}^2 + y_{pix}^2}; r_0, K, 0\right). \tag{4-6}$$

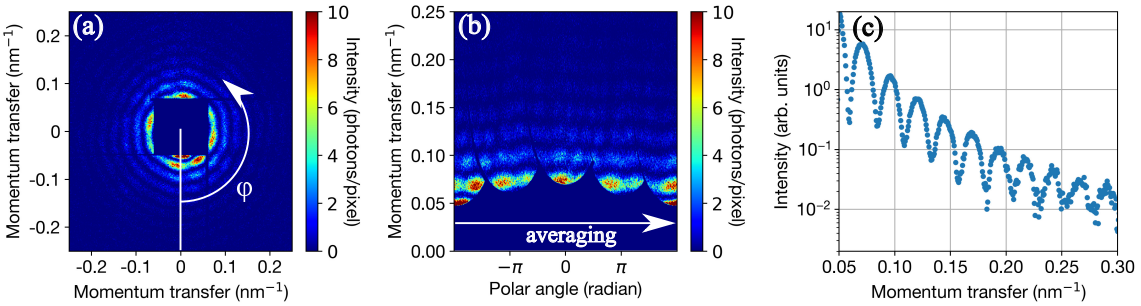

Figure 4.14: A schematic of calculation of radial profiles. The polar plot (b) was calculated by projecting the raw image (a) from the Cartesian coordinates (q_x, q_y) to the polar coordinates (q_r, ϕ) with a cubic interpolation. The radial profile (c) was then calculated by averaging the polar plot in terms of ϕ. In the calculation of the radial profile, only non-zero pixels were used; zero-value pixels correspond to the missing region of CCD elements of the sensor.

4.3.2 Extraction of the number and the photon energy of florescence photons

The number and the photon energy of fluorescence photons coming from Xe clusters were evaluated with the fluorescence spectra recorded by the single MPCCD sensors. The procedure of evaluation is as follows:

1. The specific energy range ROI_{flu} where fluorescence photons were expected to appear was determined on the basis of atomic fluorescence lines and the width of the background spectrum.

2. The numbers of fluorescence photons for each spectrum calculated by summing the photons within ROI_{flu}.

3. The mean photon energies of fluorescence photons for each spectrum were calculated by applying the weighted average to each spectrum within ROI_{flu}.

Considering that 5.5-keV photons dominantly ionize electrons in the L shell of Xe atoms, ROI_{flu} was determined by choosing the surrounding energy range of the Xe atomic lines [128] as follows:

$$ROI_{flu} = \{h\nu \in \mathbb{R} | \min\{L \text{ lines}\} - 3\sigma_{BG} \leq h\nu \leq \max\{L \text{ lines}\} + 3\sigma_{BG}\}\,. \tag{4-7}$$

The number of fluorescence photons N_{flu}, the mean photon energy $\overline{h\nu_{flu}}$, their errors $\sigma_N, \sigma_{\overline{h\nu_{flu}}}$ and the variance of $h\nu_{flu}$, $\Sigma^2_{\overline{h\nu_{flu}}}$, were calculated as follows:

$$N_{flu} = \sum_{j, h\nu_j \in ROI_{flu}} \max(S_j - B_j, 0), \tag{4-8}$$

$$\sigma_N^2 = \sum_{j, h\nu_j \in ROI_{flu}} (S_j + B_j), \tag{4-9}$$

$$\overline{h\nu_{flu}} = \frac{\sum_{j, h\nu_j \in ROI_{flu}} h\nu_j \max(S_j - B_j, 0)}{N_{flu}}, \tag{4-10}$$

$$\sigma^2_{\overline{h\nu_{flu}}} = \left(\frac{\sum_{j, h\nu_j \in ROI_{flu}} h\nu_j \sqrt{S_j + B_j}}{N_{flu}} \right)^2 + \left(\frac{\sigma_N}{N_{flu}} \times \overline{h\nu_{flu}} \right)^2, \tag{4-11}$$

$$\Sigma^2_{\overline{h\nu_{flu}}} = \frac{\sum_{j, h\nu_j \in ROI_{flu}} (h\nu_j - \overline{h\nu_{flu}})^2 \max(S_j - B_j, 0)}{N_{flu}}. \tag{4-12}$$

In Eq. 4-8-4-12, S_j and B_j are the value of the raw signal spectrum and the background spectrum at $h\nu_j$, respectively. Each bin of energy for the histogram as shown in Fig. 4.10 is identified by j. These values defined in Eq. 4-8-4-12 were calculated for each single MPCCD sensor and finally put together.

4.3.3 Assignment of charge states and the kinetic distributions by using SIMION

SIMION [122, 123] is a powerful tool to model ions and calculate their trajectories under a given electric field. To attribute the charge states and kinetic energies to the ions in TOF spectra, trajectories of Xe ions under the electric field of the spectrometer were simulated by using SIMION. The setting of voltage shown in Tab. 4.3 was used in the SIMION simulations. Fig. 4.15 shows a typical simulation result of trajectories of Xe ions. The ions are emitted in the direction toward the detector (forward emission) or backward the detector (backward emission). When the kinetic energy of ions increases, the detectable emission angle of ions is limited. Here the limit of the emission angle is called the acceptance angle.

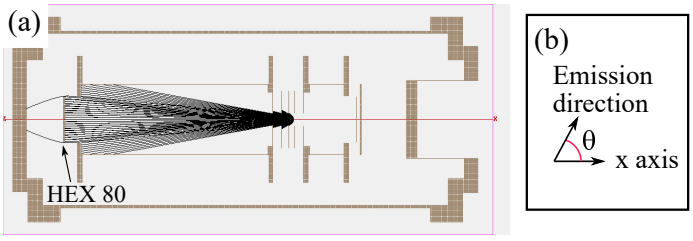

Figure 4.15: (a) A typical simulation result of ion trajectories with SIMION, where Xe^{3+} ions with the kinetic energy of 500 eV were emitted in the uniform direction. Ions hitting the detector HEX 80 are counted for calculation of the acceptance. (b) The definition of the emission angle θ.

Since the spectrometer used in the experiment has axial symmetry in terms of the x-axis shown

in Fig. 4.15(b), the threshold of angle which determines the acceptance of ions for the detector is defined by the angle between the emission direction and the x-axis, θ. The threshold can be defined in both forward and backward emission, so here the following angles are defined for convenience:

- $\theta_{accp,f}(KE_x, q)$: the acceptance angle for forward emission,
- $\theta_{accp,b}(KE_x, q)$: the acceptance angle for backward emission,

where q is the charge stage of an ion, and KE_x is the absolute value of the x-component of the initial KE of the ion, defined by $KE_x = KE \times |\cos\theta|^2$. The relationship between the time-of-flight t_{TOF} and KE_x can be also simulated by using SIMION.

Figs. 4.16(a)–(b) show the acceptance angles as functions of KE_x. Each acceptance angle varies monotonically at $KE_x = 0 \sim 1000q$ eV, which allows the inner interpolation of the acceptance angels easily in the range $[0, 1000q]$ eV for each q. Fig. 4.16(c) shows a plot of KE_x as a function of t_{TOF} for forward/backward emission. KE_x varies monotonically in the forward emission. Note that KE_x increases sharply at some t_{TOF} in each charge state, which could make the sharp TOF peaks. By comparing the KE_x-t_{TOF} curves with the observed TOF spectra and by considering the fact that the kinetic energy of ions increases with their charge state, the charge states of each TOF peak could be assigned roughly and determined by the fitting described below.

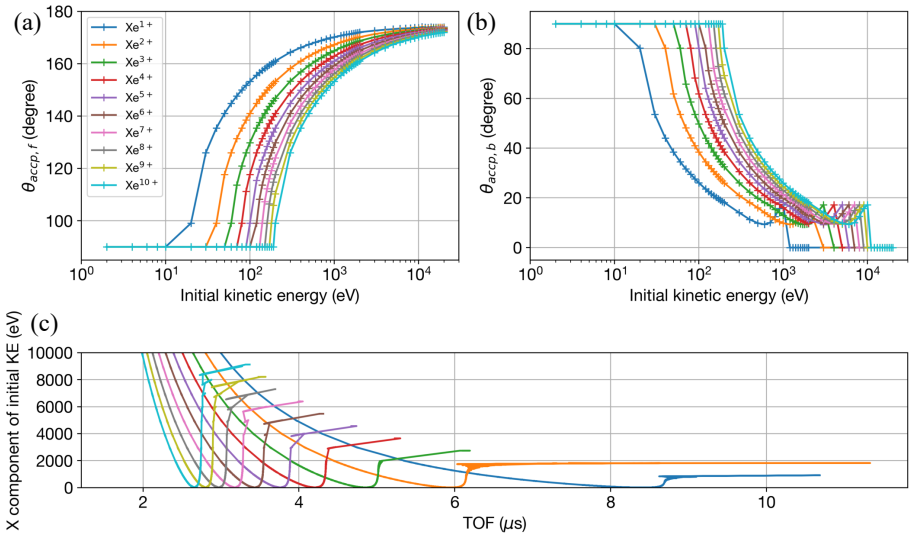

Figure 4.16: Acceptance angles and KE_x-t_{TOF} curves for Xe ions. (a) The charge and the initial KE dependence of the acceptance angle of forward emission. (a) The charge and the initial KE dependence of the acceptance angle of backward emission. (c) KE_x-t_{TOF} curves of each charge state.

The mean and standard deviation of KE, $\overline{KE}(q)$ and $\sigma_{KE}(q)$ respectively, were estimated by using

two methods. The first method is to adopt the weighing average:

$$\overline{KE}(q) = \frac{\sum_{t_{TOF}} KE(t_{TOF},q)I(t_{TOF},q)}{\sum_{t_{TOF}} I(t_{TOF},q)} \tag{4-13}$$

$$\sigma_{KE}(q) = \sqrt{\frac{\sum_{t_{TOF}} \left(KE(t_{TOF},q) - \overline{KE}(q)\right)^2 I(t_{TOF},q)}{\sum_{t_{TOF}} I(t_{TOF},q)}} \tag{4-14}$$

where $KE(t_{TOF},q)$ is KE of a charge state q as a function of t_{TOF} which is calculated by using SIMION, and $I(t_{TOF},q)$ is the intensity of a peak corresponding to q.

The second method is to use simulations with SIMION by assuming the kinetic energy distribution (KED). The scheme is as follows:

1. Xe ions having a charge state q and an initial kinetic energy KE are generated and emitted in the random direction. The distribution of emission direction is assumed to be uniform. This simulation gives acceptance angles of forward/backward emissions in the SIMION coordinates, denoted by $\theta_{accp,f}(KE,q)$, $\theta_{accp,b}(KE,q)$ respectively.

2. Pairs of the azimuthal angle θ and the polar angle ϕ are generated so that they are distributed uniformly, that is, $(\theta_k,\phi_l) = (k\pi/N_\theta, 2l\pi/N_\phi)$ $(k = 0 \sim N_\theta - 1,\ l = 0 \sim N_\phi - 1)$. The pairs (θ,ϕ) satisfying $\cos\theta\cos\phi \leq \cos\theta_{accp,f}(KE,q)$ are selected as the pairs identifying ions emitted in the forward direction and collected by the detector. The pairs (θ,ϕ) satisfying $\cos\theta\cos\phi \geq \cos\theta_{accp,b}(KE,q)$ are selected as the pairs identifying ions emitted in the backward direction and collected by the detector.

3. The x-component of KE, $KE_x(\theta_k,\phi_l)$, are calculated from each of the selected pairs by using the following relation:

$$KE_x(\theta_k,\phi_l) = KE \times \left|\cos\theta_k \cos\phi_l\right|^2. \tag{4-15}$$

   KE_x is then converted to t_{TOF} by using $KE(t_{TOF},q)$.

4. A histogram of the values of t_{TOF} obtained in the above procedure is calculated, and this histogram, denoted by $h(t_{TOF},KE,q)$, corresponds to the TOF spectra from the ions which have the charge state of q and the initial KE of KE and are emitted in the uniform direction.

5. Finally, the TOF spectrum of ions having the charge state of q and the KED $f(KE,\mu,\sigma)$ (here μ is the mean KE of KED and σ is the standard deviation of KED) is calculated as follows:

$$H(t_{TOF},q,\mu,\sigma) = \sum_{KE} f(KE,\mu,\sigma)h(t_{TOF},KE,q) \tag{4-16}$$

6. The peaks of each TOF spectrum are fitted with $H(t_{TOF},q)$, from which $\overline{KE}(q) = (\mu \text{ of the best fit})$ and $\sigma_{KE}(q) = (\sigma \text{ of the best fit})$ are obtained.

Fig. 4.17 shows a typical result of the fitting to a TOF spectrum. Here N_θ and N_ϕ were set to 1,000. The ions were assumed to have Gaussian kinetic energy distributions. The peaks of highly

charged Xe ions ($q \geq 3$) are well reproduced by the fitting procedure, and the fitting could confirm the assignment of the charge states.

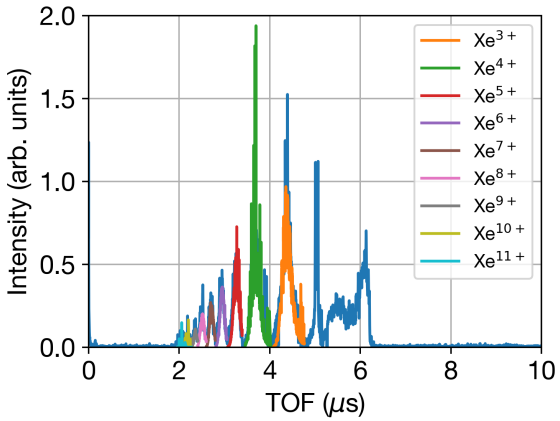

Figure 4.17: A typical result of the fitting to a TOF spectrum. Highly charged ions ($q \geq 3$) were assumed to have Gaussian kinetic energy distributions. μ and σ of the kinetic energy distributions were determined so that the calculated TOF spectra reproduced each peak best.

4.4 Results and discussion

The multi-spectroscopic measurements of Xe clusters were carried out with the experimental setups described in section 4.1. Fig. 4.18 shows typical results of the SAXS images, fluorescence spectra and ion TOF spectra from Xe clusters recorded for each FEL pulse. Since the hit ratio is less than 0.1 % under the current condition, the recorded data of each FEL shot was considered mainly to originate from a single cluster in the focus of the FEL pulse. Clear diffraction rings were observed in the SAXS images of Xe clusters, and most of the SAXS images consisted of concentric rings. These images suggest a spherical shape for the xenon clusters. The size of the Xe clusters and the fluence of XFEL pulses at the actual reaction point were extracted by applying the analysis scheme described in subsection 4.3.1. The obtained values of cluster size and XFEL fluence are given above Fig. 4.18 (a), (d) and (g). Fig. 4.18 (a)–(c) show the SAXS image, fluorescence and TOF spectra recorded at the high fluence. The diffraction pattern had high intensity, and the fluorescence spectrum shows an evident peak at around 4.5 keV, at the high energy side of the dark signal peak of the MPCCD sensor at 0 keV. Highly charged ions were observed in the TOF spectrum. As the XFEL fluence and the cluster size decreased, as shown in Fig. 4.18 (d)–(f) and (g)–(i), the SAXS signals got weaker, the yield of fluorescence photons decreased, and less highly charged ions were observed, while ions in the lower charge state showed up. These results indicate that XFEL–cluster interaction can be investigated more accurately by using size- and fluence-selective measurements, i.e. by eliminating the washout of characteristics of single targets due to size distribution of the sample and laser intensity profile [46, 49, 57, 58].

4.4.1 SAXS signals and properties of clusters

Characteristics images and their interpretation

The SAXS images, or diffraction patterns, have information on the size and shape of the clusters and the XFEL fluence at the actual reaction point. Fig. 4.19 shows characteristic diffraction patterns from clusters. The diffraction patterns shown in Figs. 4.19(a)–(c) were observed by using the after-pulse timing at 300 K, and the pattern shown in Fig. (d) was observed by using the normal timing at 300 K. The statistics of patterns in terms of their pattern types is shown in Tab. 4.5. The majority (over 90 %) of the observed diffraction patterns were composed of concentric circular rings as shown in Fig. 4.19(a), which suggested spherically shaped clusters. A few diffraction patterns showed diffraction rings with modulation of intensity as shown in Fig. 4.19(b)-(c), indicating that non-spherical clusters were generated in the after-pulse timing. While these patterns are considered to come from single clusters, there was one pattern consisting of Newton rings whose center was far from the center of the MPCCD detector (Fig. 4.19(d)). This image indicates that a few clusters were in the focal spot of FEL. Observation of these characteristic patterns has been reported in the preceding studies using soft X-ray FELs [43–45, 47], and one can distinguish patterns coming from single clusters from patterns coming from several clusters in the FEL focus.

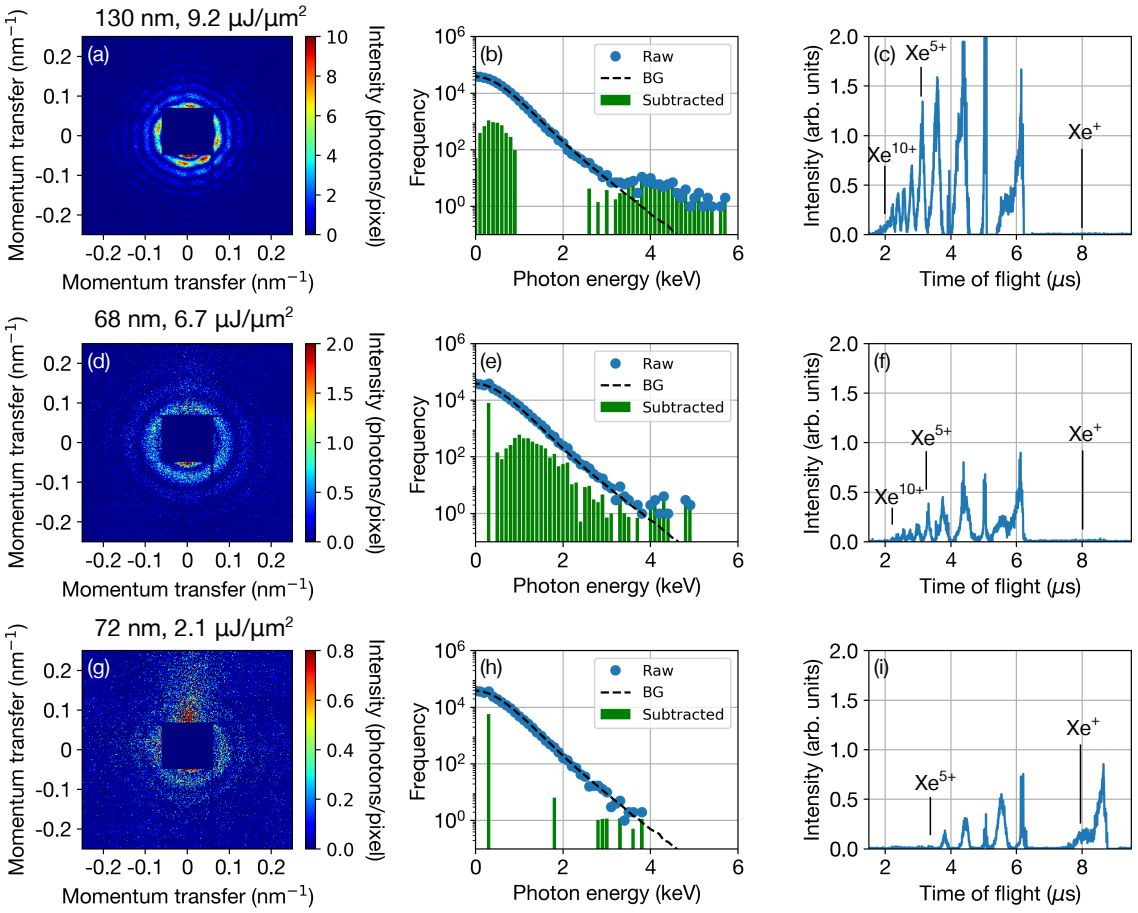

Figure 4.18: Characteristic results of the multi-spectroscopic measurements. Each diffraction image, fluorescence spectrum and ion TOF spectrum shown in (a)–(c), (d)–(f), and (g)–(i) were observed from Xe clusters with the radius of cluster and the fluence (r_0, J_0) of (130 nm, 9.2 μJ/μm^2), (68 nm, 6.7 μJ/μm^2), (72 nm, 2.1 μJ/μm^2), respectively. Scattered intensity was observed in the upper region of diffraction images ((a), (d), (g)), which came from the parasitic scattering of the XFEL pulses due to the configuration of the upstream optical system. From [125], licensed under CC BY 4.0.

Analysis of the SAXS image (Fig. 4.19(b)) using a gradient search algorithm in combination with an initial estimate give an insight into the cluster growth process [129]. Fig. 4.20 shows the result of the reconstruction of the 2D electron density map from the SAXS image (Fig. 4.19(b)). It shows that a hailstone-shaped cluster, which has a shape of a large cluster (r_0 = 130 nm) with a small cluster (r_0 = 20 nm) on its surface like a protrusion, were generated by using the after-pulse timing of the gas jet. The observation of the hailstone-shaped clusters is a signature of cluster-cluster aggregation for the growth of large clusters [47, 117, 130], while monomer addition is dominant in the initial growth of clusters as discussed in section 3.3.

Table 4.5: The statistics of the SAXS images in terms of their pattern types.

Concentric circular rings	Concentric modulated rings	Newton rings	Total hits
74	6	1	81

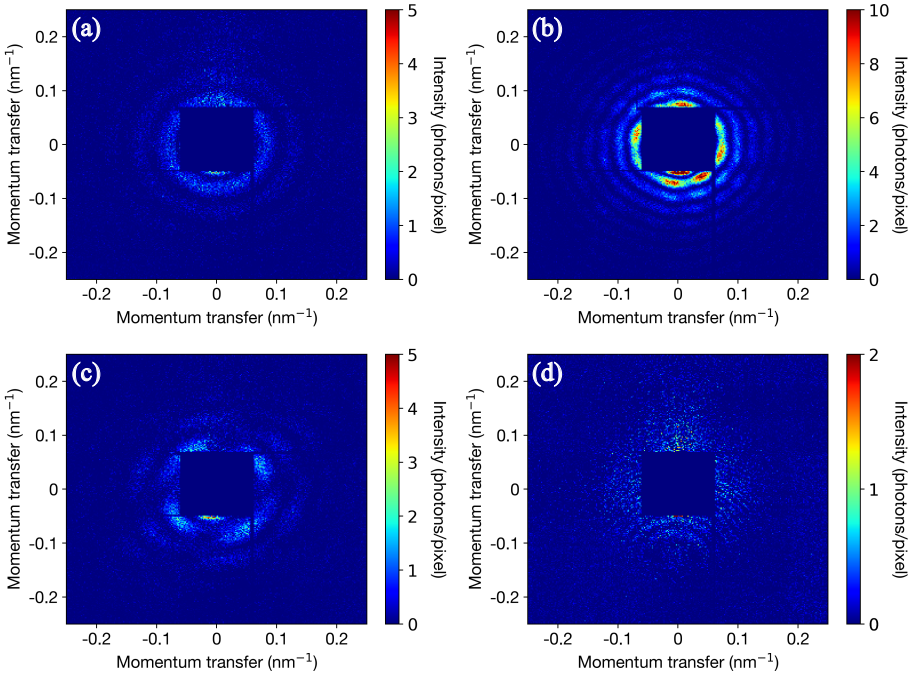

Figure 4.19: Characteristic SAXS images observed in the experiment. (a) Most of the observed images were composed of uniform concentric circular rings. (b) The image having the highest signal intensity showed modulated rings, suggesting a hailstone-shaped cluster [129]. (c) A few images showed non-circular rings, which suggests non-spherical clusters. (d) Newton rings indicating a few clusters were in the focal spot of FEL.

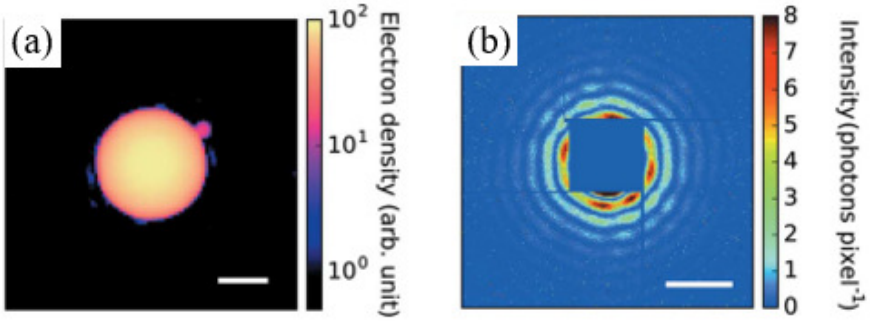

Figure 4.20: The 2D electron density map reconstructed by using a refinement method. (a) The reconstructed 2D density map from the diffraction pattern shown in Fig. 4.19(b). The density map is composed of one larger sphere component on its center and one smaller sphere component on the surface of the larger one. (b) The diffraction pattern calculated from the density map shown in (a). From [129], licensed under CC BY 4.0.

Fitting results and the cluster size distribution

Fig. 4.21(a) shows typical radial profiles derived from diffraction images and the corresponding fitting curves. The fitting assuming a single uniformly dense sphere with Thomson scattering reproduced the experimental results well. Fig. 4.21 (b) shows the histogram of radii of the spherical Xe clusters under the after-pulse condition at 300 K (top panel) and the normal pulse condition at 250 K (bottom panel). Fitting curves (black dashed lines) based on the log-normal distribution of cluster size give the average cluster radius of 81 nm on the after-pulse condition and 35 nm on the normal pulse condition with cooling. Cluster radii peaked around 80 nm and the larger clusters were observed. These clusters have larger radii than the clusters predicted by The well-known scaling law [108, 112] predicted the average cluster radius of 25–44 nm at 300 K and 32–61 nm at 250 K. Compared with the predicted values, the after-pulse condition gave much larger clusters than the predicted size, while the average size of clusters observed on normal pulse condition with cooling are in good agreement with the predicted size. The generation of such larger clusters occurred because we adopted jet timing where extremely large Xe clusters can be generated on the after-pulse condition [47].

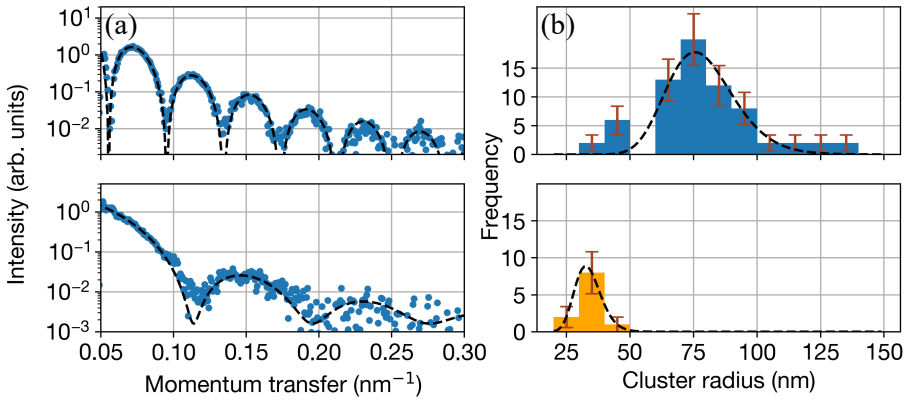

Figure 4.21: Radial profiles and distributions of cluster radius. (a) Characteristic radial profiles of diffraction images. The radii of the Xe clusters giving the top and the bottom profiles are 81 nm and 39 nm, respectively. The formula of the fitting curves (black dashed lines) is described in Eq. 4-5. (b) The histograms of radii of the observed Xe clusters on the after-pulse condition at 300 K (top) and on the normal pulse condition at 250 K (bottom). The error bars are composed of the statistical errors of the frequency of observation. The black dashed lines in (b) are fitting curves based on a log-normal distribution of cluster size and give the averaged radii of 81 nm and 35 nm, respectively. No clusters with the radii of 50–60 nm were observed on the after-pulse condition (top panel in (b)), which could be an accidental error due to the low statistics.

4.4.2 Fluorescence spectra

As mentioned in subsection 4.3.2, the L-shell ionization of Xe atoms is dominant with photons with the energy of 5.48 keV, and the fluorescence from L shells (L_β and L_α lines) is expected to be emitted dominantly. The fluorescence photons were observed around these Xe atomic fluorescence lines, as shown in Fig. 4.18(b), (e), and (h). Furthermore, the probability of X-ray absorption by Xe atoms is expected to very low and the expectation of the absorption rate by Xe atoms is estimated to be only

a few percentages by using the cross section shown in Fig. 2.1(b). On the other hand, the preceding study [9] using ion TOF spectroscopy has reported that highly charged Xe atoms were generated via two-photon ionization within the exposure of single 5.5-keV XFEL pulses at the fluence equivalent to those observed in this work. The number of fluorescence photons from a particle is proportional to the product of J_0 and the volume exposed to the incident photons under the conditions where the intensity of the incident beam is not so extremely high. In the experiment, the cluster size was much smaller than the focal spot of FEL, and therefore N_{flu} would be proportional to the product of J_0 and the cluster volume, i.e. the number of atoms in the cluster N ($\propto r_0^3$). On the other hand, it can be shown by calculating Eq. 4-6 that N_{scat} is approximately proportional to Kr_0^4, i.e. proportional to $J_0 r_0^4$ for spherical clusters with the observed size. Therefore, it can be expected that N_{flu} and N_{scat} have a relationship $N_{flu} \times r_0 \propto N_{scat}$. Fig. 4.22(a) shows the correlation between $N_{flu} \times r_0$ and N_{scat}, and there is evidence of linear correlation between N_{scat} and $N_{flu} \times r_0$. This indicates that both the observed fluorescence and scattered photons actually came from the same targets for each XFEL shot.

The position of the fluorescence photon peak was also plotted in Fig. 4.22(b). A broad peak was found to be located at 4 keV, and the position of this peak was not changed by the FEL fluence. Furthermore, the observed peak position corresponds to the fluorescence energies of the Xe atomic L_α and L_β lines. Therefore, these photons are the result of the radiative decay of inner-core excited Xe atoms in the clusters. Although more detail discussion (e.g. multi-photon absorption) cannot be expected due to limited statistics and the energy resolution of the fluorescence spectroscopy in the current conditions, the above results show that fluorescence spectroscopy monitoring of the fluence of the incident FEL pulses offers the possibility of studying the degree of inner ionization of samples under intense laser field [9, 14, 15, 42, 131].

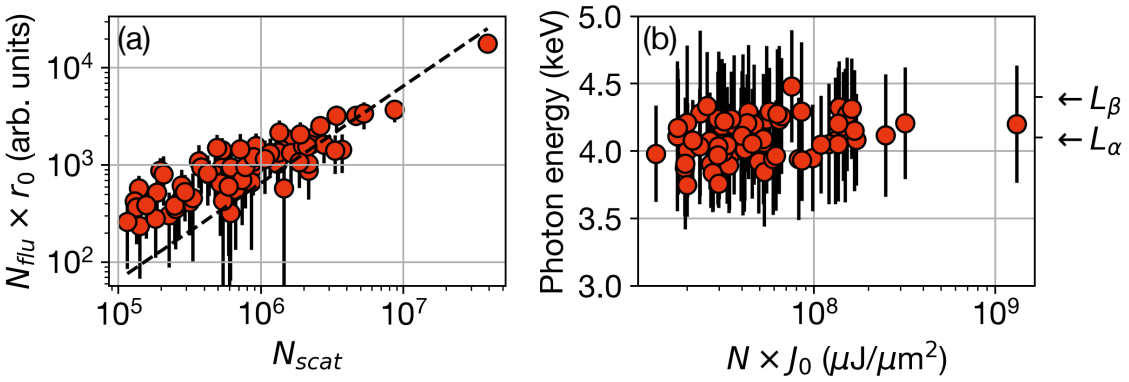

Figure 4.22: Correlation maps between the observables obtained from fluorescence spectra and SAXS images. (a) Correlation between the number of scattered photons and that of fluorescence photons detected by one of the two single MPCCD sensors. The black dashed line is a guide for the eyes representing $N_{flu} \times r_0 \propto N_{scat}$. (b) Correlation between the X-ray dose (= cluster size × XFEL fluence) and the photon energy of fluorescence. The positions of the photon energies of Xe atomic L_α and L_β fluorescence are shown to the right side of (b). The error bars shown in (a) are composed of the statistical errors of N_{flu} defined in Eq. 4-9 and N_{scat}. The error bars shown in (b) are defined in Eq. 4-11. From [125], licensed under CC BY 4.0.

4.4.3 TOF spectra of Xe ions

Ion TOF spectroscopy records ions generated in laser-matter interaction undergo the whole process in the interaction. The charge distribution and the kinetic energy distribution of ions extracted from recorded TOF spectra contain information on ion generation processes, with which the fundamental mechanisms of the formation and development of nanoplasmas have been discussed.

Fluence and size dependence of TOF spectra and ion charge distributions

Fig. 4.23 shows the ion TOF spectra of Xe clusters under different conditions. TOF spectra recorded at high FEL fluence ($\sim$ 8 μJ μm^{-2}) and low FEL fluence ($\sim$ 3 μJ μm^{-2}) are shown in Figs. 4.23 (a)–(c) and Figs. 4.23 (d)–(f), respectively. The apparent charge distributions of Xe ions are shown in the insets of each panel of Fig. 4.23. Substantial TOF intensity of singly charged Xe ions was observed at lower XFEL fluence irrespective of cluster size. On the other hand, singly charged ions were suppressed and more highly charged ions were generated at higher XFEL fluence.

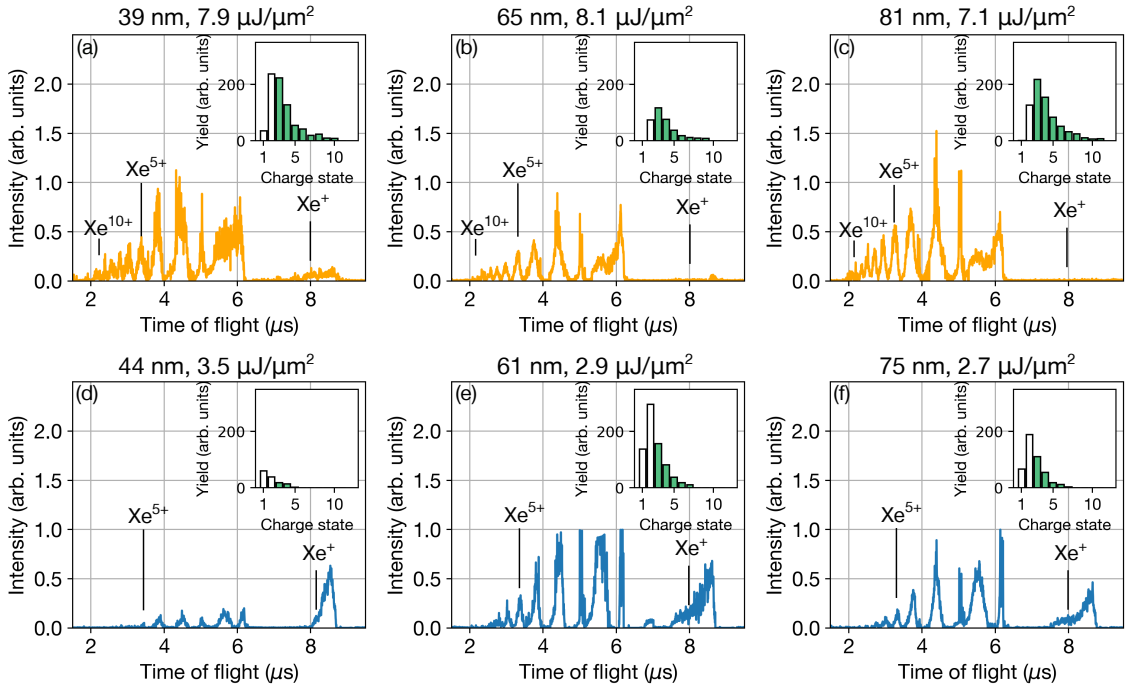

Figure 4.23: Ion TOF spectra of Xe clusters with sizes of around (a,d) 40 nm, (b,e) 60nm, and (c,f) 80 nm. Ion charge states of each peak were determined by a simulation using SIMION [122]. The charge distributions of the detected Xe ions extracted from each TOF spectrum are shown in the insets. The yields of doubly charged ions and singly charged ions are less reliable due to the lowering of detection efficiency and the saturation of signal, which were caused by the detection of a large number of highly charged Xe ions. The baseline of spectra is corrected because it was modulated due to the lowering of detection efficiency and the detection of a large number of ions. From [125], licensed under CC BY 4.0.

Fluence and size dependence of the maximum charge state and the apparent averaged charge state

Fig. 4.24 shows the XFEL fluence dependence of the maximum charge state (Z_{max}) and the apparent averaged charge state (Z_{ave}) of Xe ions. Z_{max} increased steeply and saturated at around 12 as the XFEL fluence increased. Z_{ave} also increased with the XFEL fluence. In the current data set, both Z_{max} and Z_{ave} seemed to show a dependence on the cluster size slightly, but the further discussion of the size dependence is difficult because there is a limited statistic. Elucidation of the size dependence should be an important theme for further understanding of laser-matter interaction.

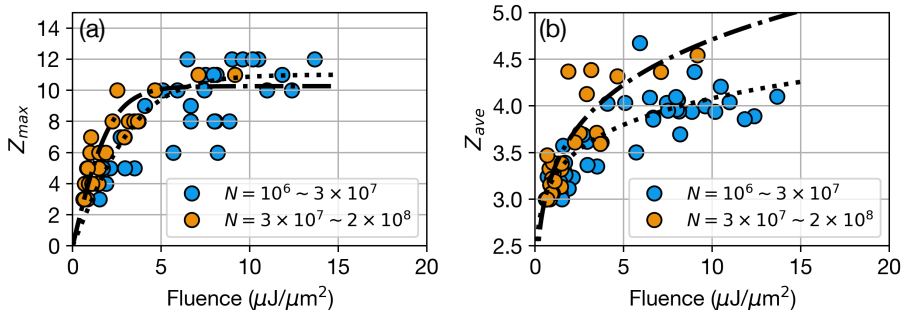

Figure 4.24: XFEL fluence dependence on the charge state of Xe ions. (a) The observed maximum charge state Z_{max}. (b) The apparent averaged charge state Z_{ave} calculated by weighted averaging over the peaks in the TOF spectrum corresponding to the charge state ≥ 3. The dashed lines and the dotted lines in (b)-(c) are the guides for the eyes. From [125], licensed under CC BY 4.0.

The strong dependence of the charge state of Xe ions on the fluence of the XFEL pulses is in agreement with the preceding studies using soft XFELs with 91 eV [49] and 800 eV [46]. Moreover, the suppression of singly charged ions and steep increase of charge state with higher fluence also agrees well with the results using 800-eV XFEL pulses [46], suggesting the efficient suppression of electron-ion recombination. Notably, the saturated charge state observed in this study was also lower compared to the preceding studies. This difference may be due to the different excitation energy, deposition energy and ionization efficiency of the incident photons.

4.5 Summary of results and discussion I

In this chapter, the methods and apparatus for multi-spectroscopic measurements of SAXS by using XFEL of SACLA are presented and their discoveries are discussed. The SAXS signals, fluorescence spectra and ion TOF spectra of single giant xenon clusters were recorded simultaneously in the shot-by-shot scheme. The radii of the clusters and the XFEL fluences at the reaction point have been evaluated from SAXS signals. Ion TOF spectra and fluorescence spectra were sorted by using the obtained radii and fluences. A clear correlation of the observables extracted from the ion TOF and fluorescence spectra with the cluster size and the FEL fluence was observed. The present results demonstrate the importance of removing the averaging effects of the size distribution of the clusters, as well as the laser fluence profile to obtain deep insight into the laser–matter interaction. The information extracted from our single-shot single-particle datasets is in good agreement with the findings of previous studies using similar styles of single-shot approaches in the soft X-ray and ultraviolet spectral regime. This work underlines the potential of size- and fluence-selective spectroscopy for advancing the research in laser–matter interaction in the hard X-ray spectral regime.

Chapter 5

Results and discussion II: Ultrafast structural dynamics of nanoparticles in intense laser fields

This chapter describes the second study [132] of this dissertation. Structural dynamics in atomic clusters pumped with intense near-infrared (NIR) pulses into a nanoplasma state will be described. Employing a WAXS technique with intense femtosecond X-ray pulses from an XFEL source, we find that highly excited Xe nanoparticles retain their crystalline bulk structure and density in their inner core long after the driving NIR pulse. The observed disordering of the local structural in the nanoplasma is consistent with propagation from the surface to the inner core of the clusters.

5.1 Experimental setups

The experiment in this study was carried out at EH2 of BL3 [97] of SACLA [90]. The experimental setups are summarized in Fig. 5.1 and Fig. 5.2 shows a photograph of the experimental apparatus in EH2. This experimental system was composed of the following apparatuses.

- XFEL source: SACLA
- Optical laser system
- Cluster source: a pulse cluster jet generator
- Ion detector: an ion time-of-flight spectrometer
- Photon detector: a multi-port CCD sensor

Firstly the specific setups will be described.

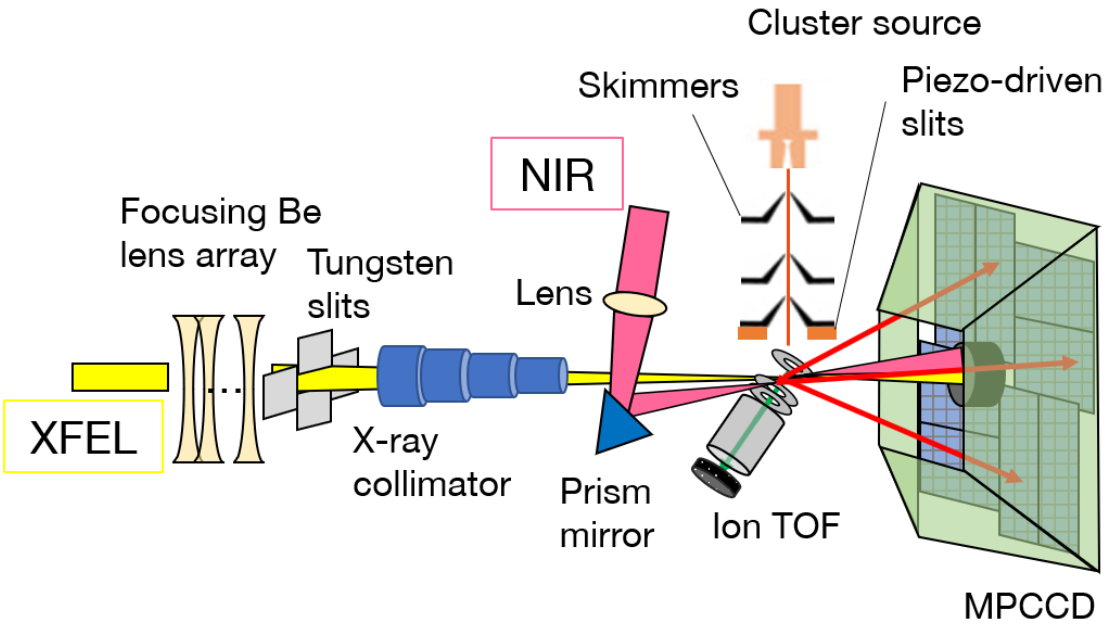

Figure 5.1: A schematic diagram of the experimental setup. XFEL pulses were focused by a Be lens array system [98]. The cluster beam was generated through adiabatic expansion and introduced through two skimmers, and finally tailored with piezo-driven slits. The scattered photons were collected by an octal MPCCD sensor installed 100 mm from the reaction point in the direction of the XFEL beam. Ions were collected by an ion TOF spectrometer installed to the orthogonal direction to the directions of the cluster jet and XFEL/NIR pulses. From [132]. Reprinted with permission from APS.

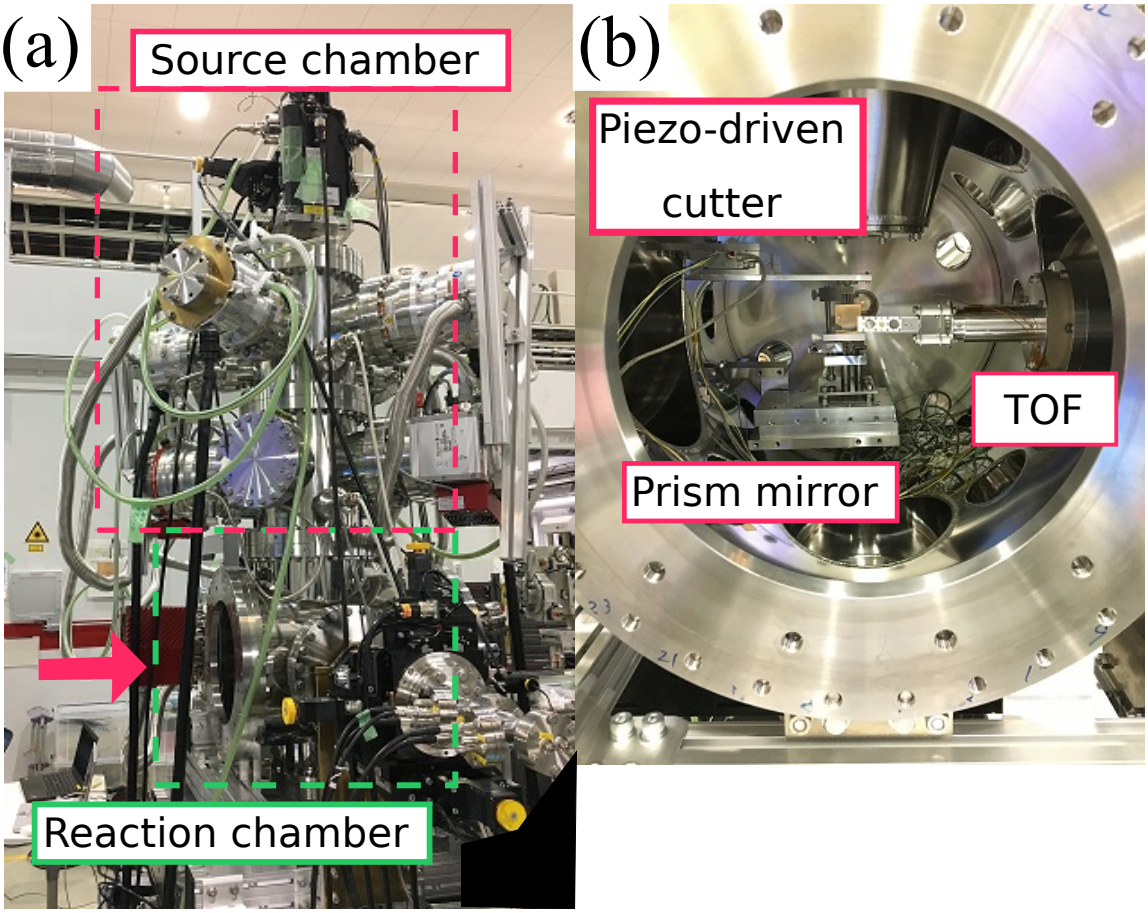

Figure 5.2: Photographs of the experimental chamber and its interior. (a) A photograph of the experimental chamber. The cluster source chamber has been located on the upper side of the reaction chamber. The short-working-distance octal MPCCD sensor was attached to the reaction chamber from the direction depicted by an arrow in (a). (b) A photograph of the interior of the reaction chamber viewed from the side directed by an arrow in (a). A prism mirror was installed on a piezo motor stage to introduce the NIR beam almost collinearly to the XFEL beam. A molecular beam cutter was mounted on the piezo motor stages and installed at the downstream of the second skimmer. An ion TOF spectrometer was installed horizontally to the reaction chamber. A beam position monitor was attached to the top of the spectrometer.

5.1.1 Laser sources and X-ray optics

We adopted 11.0 keV for X-ray photon energy so that the Bragg reflection from fcc (220) of a Xe crystal can be recorded by a short-working-distance (SWD) MPCCD sensor. XFEL pulses were focused by the CRLs to 1.4×1.6 μm^2 (horizontal & vertical directions, FWHM). The photon energy of each XFEL pulse was measured by a spectrometer with the double-crystal monochromator system before the experiment. Fig. 5.3 shows the photon energy spectrum of XFEL pulses accumulated on several tens shots. The photon energy used in the experiment was estimated to be 11.0 keV by fitting this spectrum with a Gaussian function and monitored by using the inline spectrometer [96] during the experiment. The corresponding wavelength and wavenumber were 1.13 Å and 5.58 Å^{-1}, respectively. The resulting intensity of the XFEL pulses was 4×10^{17} W/cm^2 on average.

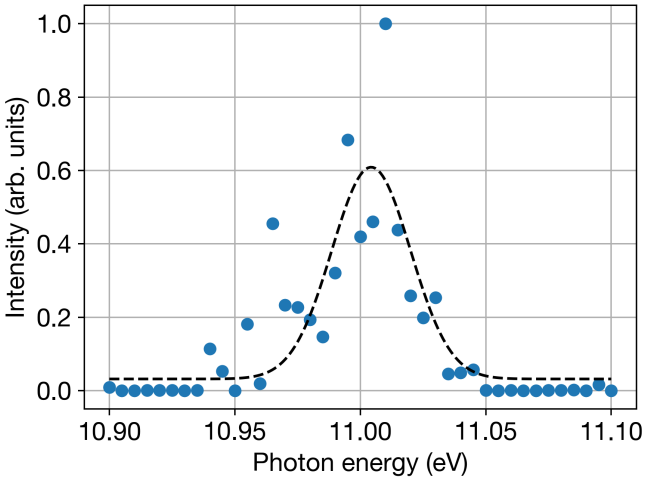

Figure 5.3: The photon energy spectrum of XFEL pulse. The dashed line is a fitting curve and the resulting photon energy is 11.0 keV.

The NIR laser pulses with a wavelength of 800 nm and a pulse length of 30 fs were focused by a single plano-convex lens (the focal length: 500 mm). Then the NIR pulses were reflected by a prism mirror on a piezo-driven stage installed in the reaction chamber and overlapped with the XFEL pulses at an angle of 3°. The focal spot size at the reaction point was $(4 \times 10^1) \times (4 \times 10^1)$ μm^2, resulting in an intensity of 4×10^{16} W/cm^2. The delay time of the XFEL pulse relative to the NIR pulse was controlled by using the delay stages of the optical laser system. Here the positive delay corresponds to a NIR pulse arriving at the reaction point earlier than an XFEL pulse. In the actual procedure, we set the delay time to 0 fs and +1,000 fs by using the delay stages, and utilized the timing jitter to obtain data at the delay time other than the set delays. The temporal jitter between the arrival time of the XFEL pulses and the NIR pulses was measured by using the arrival timing monitor with 20-fs precision.

A combination of a four-jaws slit and a stainless-steel collimator were installed on the upstream side

of the reaction chamber to reduce undesirable light coming from the upstream of the XFEL beam. The position of the collimator was adjusted so that the intensity of the XFEL beam detected by the photodiode sensor installed to the reaction chamber was maximized. A beam stop was composed of a graphite conical-shape rod, an Al disk and a tungsten plate (shown in Fig. 5.4(a)). The beam stop was installed in front of the MPCCD sensor so that the direct XFEL and NIR beams could not hit the sensor. The beam stop was fixed to the calculated position where both direct beams of XFEL and NIR were hit on the front of the beam stop. A Kapton film with a thickness of 75 μm was attached to the front of the MPCCD sensor as a filter to protect the sensor from ion debris (shown in Fig. 5.4(b)). A Baffle composed of stainless-steel plates and Al plates was attached to the front of the MPCCD sensor in order to reduce background X-ray photons (shown in Fig. 5.4(c)).

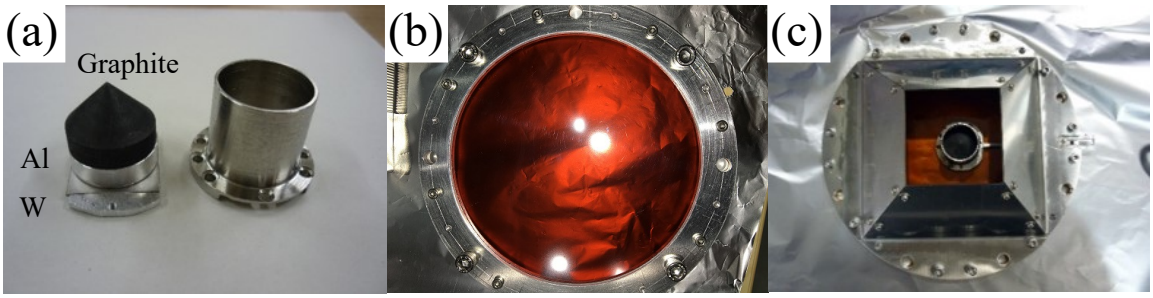

Figure 5.4: Photographs of instruments installed along the XFEL and NIR paths to perform the experiment. (a) A beam stop. (b) A Kapton film filter. (c) Assemble of the beam stop, the Kapton filter, and a baffle. The internal of the baffle was coated with graphite to reduce the background photons.

5.1.2 The cluster source

A cluster jet source was implemented with a pulse valve. Fig. 5.5 shows photographs of the cluster source used in this experiment. The cluster source shown in Fig. 5.5(a) has a valve mount made of Al and the Al mount is combined to a cooling mount made of Cu. Two Peltier devices are inserted in the interface between the Al mount and the Cu cooling mount. The pulse valve can be cooled by the Peltier devices and the flow of refrigerant. The opening of the solenoid valve is controlled by using a dedicated controller IOTA ONE. A convergent-divergent nozzle was mounted on the front plate of the solenoid valve with a support made of Al as shown in Fig. 5.5(b). The interface between the nozzle and the valve, and the interface between the nozzle and the Al support are sealed with gaskets made of indium to avoid the leak of gas. The diameter and half angle of the nozzle are 200 μm and 4°, respectively. The duration of the pulse gas beam was set to 1 ms and the repetition rate was set to 30 Hz to match that of the XFEL shots. The stagnation pressure was set to 30 bar and the stagnation temperature was set to 290 K. Under these conditions, the cluster size is estimated to be $2.2 \times 10^6 \sim 1.6 \times 10^7$ atoms ($30 \sim 60$ nm in radius) by the scaling law [108, 112].

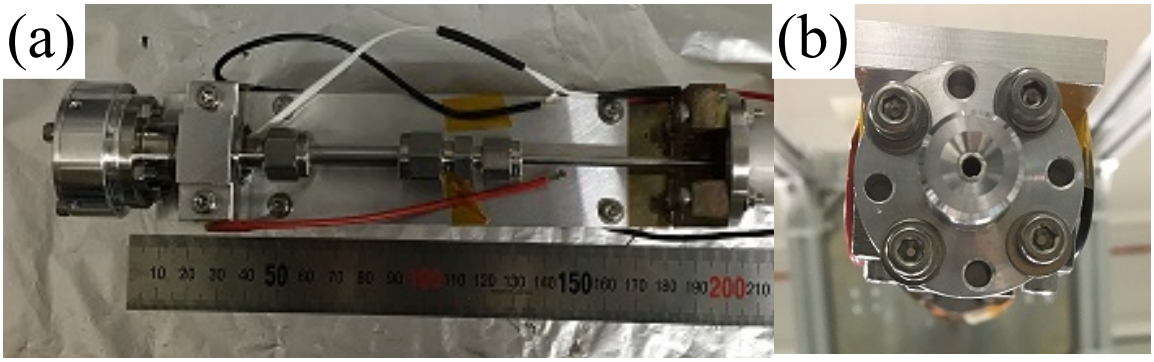

Figure 5.5: Photographs of the cluster source. (a) A photograph of the top side of the cluster source used in the experiment. A pulse valve was set on an Al mount and cooled by Peltier devices. (b) A photograph of the tip of the cluster source. The attachment nozzle has a cylindrical shape and a conical hole with a diameter of 200 μm. This nozzle was attached on the front plate of the solenoid valve via a sealing indium gasket and covered with an Al support to fix its position on the valve as shown in (b).

5.1.3 Experimental chamber

Our apparatus consists of three vacuum chambers, i.e. cluster source chamber, differential pumping chamber and reaction chamber (Fig. 5.6(a)). A cluster source is mounted on a motorized three-axis stage and installed in the cluster source chamber. The cluster beam passes two skimmers so that the core of the cluster jet can be delivered to the reaction point. The diameters of the first and second skimmer were 0.4 mm and 2.0 mm, respectively. The distance between the nozzle and the reaction point was about 200 mm to realize enough cluster number density for the diffraction experiment. Each vacuum chamber is equipped with several pumps as shown in the schematic diagram (Fig. 5.6(b)) and Tab. 5.1. This configuration has enabled to keep the high vacuum during the experiment which is often essential for effective cluster generation. The reaction chamber has the following instruments in the internal as shown in Fig. 5.2:

- A molecular beam cutter on a pair of piezo motors: to tailor the gas jet at the position near the reaction point.
- A prism mirror on a piezo motor stage: to reflect incident NIR pulses.
- An ion TOF spectrometer with a beam position monitor: to detect ions generated during the interaction between NIR/XFEL pulses and clusters.
- a photodiode sensor: to check the coming of XFEL pulses.

Fig. 5.7 shows close-up photographs of the above instruments other than the TOF spectrometer and the photodiode sensor. Pumps are also attached to the reaction chamber to keep a high vacuum degree. The positions of the piezo-driven cutters were adjusted so that the cutters reduced the width of the gas jet in the XFEL direction down to 1 mm, which was smaller than the Rayleigh length of the XFEL pulses. These setups could reduce the pressure in the cluster source chamber, the differential pumping chamber, and the reaction chamber without gas load as low as 10^{-5} Pa,

10^{-6} Pa and 10^{-4} Pa, respectively.

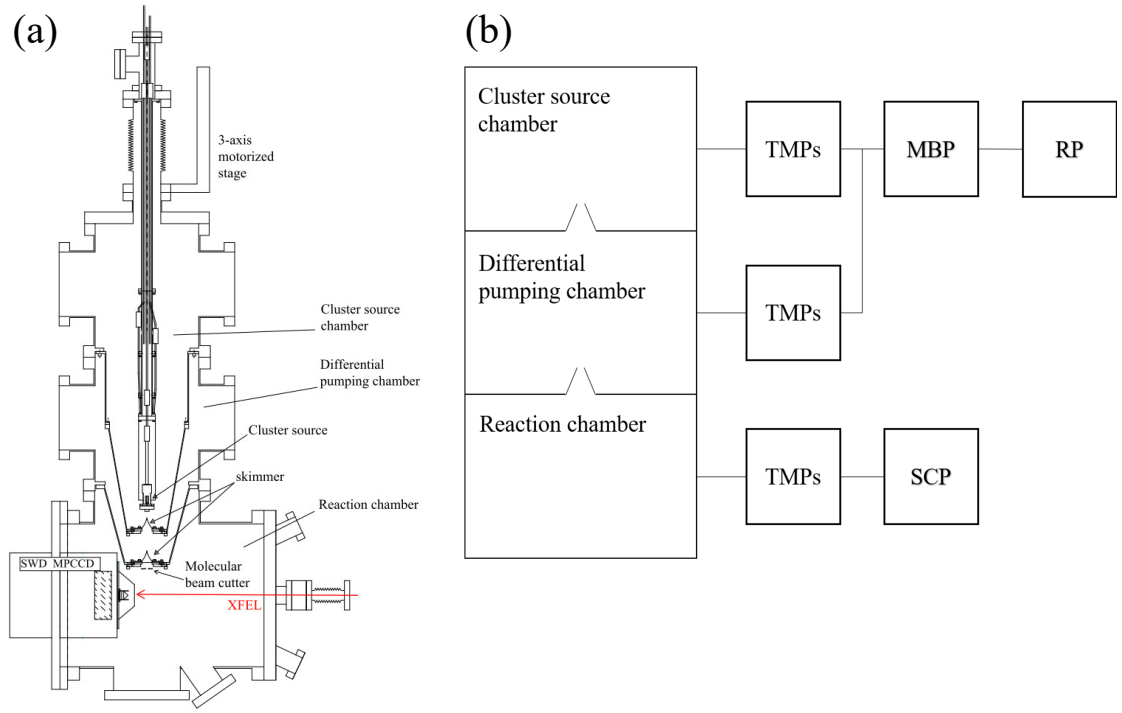

Figure 5.6: Schematics of the chambers and the pumping system. These are courtesy of K. Nagaya. (a) A schematic of the chambers. The source chamber is composed of two parts for differential pumping. The cluster source was installed so that its top was a few tens mm distant from the cusp of the first skimmer. (b) A schematic of the pumping system.

Table 5.1: Specification of pumps used in the experiment. Each pumping speed is for gaseous N_2.

Chamber	TMPs	Roughing pumps
Cluster source	Osaka TG420M (400 L/s) × 4	ULVAC PMB003C (90 L/s) × 1 with ULVAC D-950DK (15 L/s) × 1
Differential pumping	Pfeiffer HiPace 700 (685 L/s) × 2	Common to Cluster source
Reaction	Edwards STP-iX455 (450 L/s) × 2	ULVAC DIS-500 (10 L/s) × 1

5.1.4 Adjustment of the position and timing

The position of the reaction chamber was adjusted coarsely by using the three-axis stage under the chamber so that the designed reaction point and the focal point of incident XFEL pulses were overlapped. The Ce:YAG screen of the beam position monitor was used to confirm the spatial overlap between the XFEL and NIR beams. The Bragg reflection from the GaAs crystal was collected to determine the actual center of the diffraction images. The position of the cluster source was aligned by the motorized translator so that the pulse gas jet could be introduced to the reaction point in the reaction chamber. To achieve this condition, a QMS (microvision2) was installed on the downstream of the gas jet and the volume of gas jet reaching the mass spectrometer was monitored. The position of the gas jet was determined with Ar gas at 20 bar by maximizing the yields of Ar cluster ions

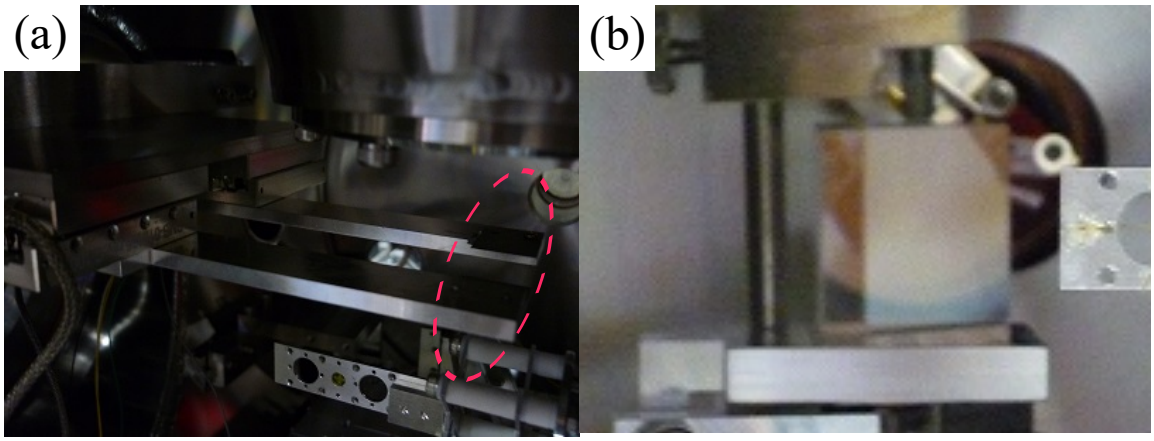

Figure 5.7: Close-up photographs of the installed instruments. (a) The piezo-driven cutter. A pair of cutters is marked with a dashed-line circle. (b) The prism mirror.

Ar_n^+ ($n = 2 \sim 7$) detected by the QMS. The final distance between the outlet of the nozzle and the cusp of the first skimmer was set to around 20 mm.

5.1.5 Ion TOF spectrometer

The ion TOF spectrometer used in the experiment is shown in Fig. 5.8. This spectrometer consists of two electrodes (pusher and puller), a drift tube, an MCP plate, a photo converter, and a photo-multiplier tube (PMT). The puller has a hole at its center. By moving the position of the hole, the spectrometer can filter ions having the specific kinetic energy. The TOF spectrometer is installed on a three-axis motorized translator made by Vacuum and Optical Instruments. This setting allows us to introduce the beam position monitor to the reaction point and to utilize the filtering with the hole of the puller. In the experiment, the reaction point was supposed to be the center of the region between the pusher and the puller. Generated ions were extracted toward the PMT along the electron field generated by applying the voltages to the components of the spectrometer. The applied voltages are listed in Tab. 5.2. For each XFEL shot, the output signal of the PMT was recorded by a high-speed digitizer (Acqiris DC282).

Table 5.2: List of the voltages applied to the components of the spectrometer.

	Pusher	Puller	Tube	MCP	Photo converter	PMT
Voltage [V]	1,000	375	100	-700	2,300	-850

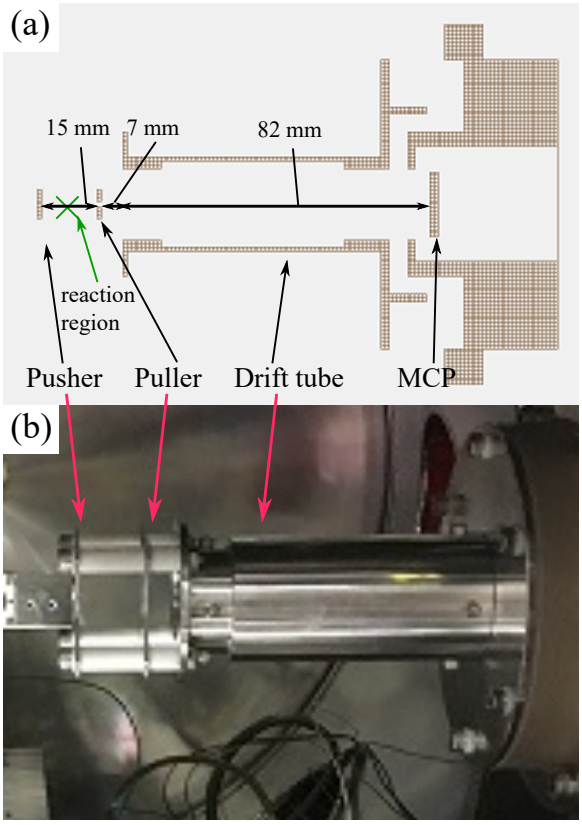

Figure 5.8: Ion TOF spectrometer. (a) A schematic of the ion TOF spectrometer. Voltages were applied independently to the electrodes, the drift tube, the MCP plate, the photo converter, and the PMT. (b) A photograph of the TOF spectrometer. Each electrode was insulated each other by ceramic spacers.

5.1.6 MPCCD

An SWD octal MPCCD sensor was used to detect X-ray photons scattered in wide-angle directions. Fig. 5.9 shows a schematic and photographs of the SWD MPCCD sensor. The specification of an MPCCD module is shown in Tab. 3.5. The MPCCD sensor was attached to the XFEL downstream side of the reaction chamber, and the distance between the reaction point and the front of the MPCCD modules was 100 mm. Under the experimental setup, the detector covered a scattering angle range of 14°–35°, which corresponds to a momentum transfer of q = 1.4–3.4 Å^{-1}.

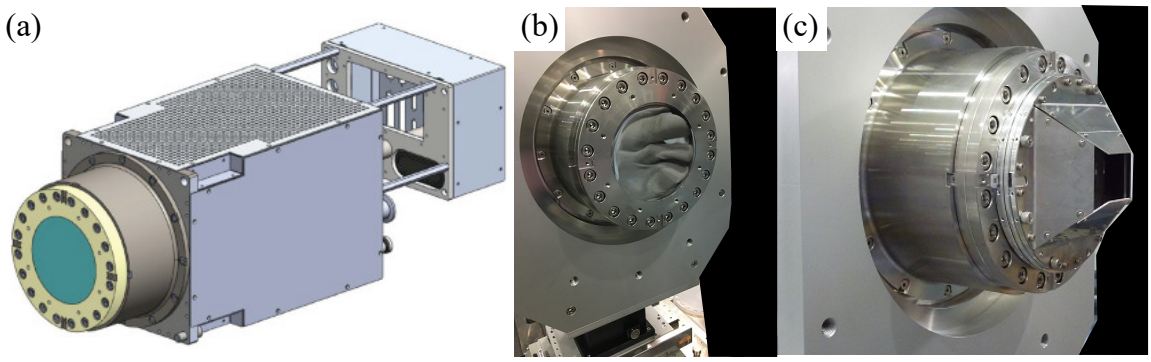

Figure 5.9: SWD octal MPCCD sensor. (a) Drawing of an SWD octal MPCCD sensor. The detection area is around 102×102 mm. From [133], licensed under CC BY 4.0. (b) A photograph of the front of the SWD MPCCD sensor. The front of the MPCCD sensor is protected with a Be film. (c) A photograph of the front of the SWD MPCCD sensor equipped with the assembly shown in Fig. 5.4(c).

5.1.7 Experimental parameters

At the end of this section, the experimental parameters are shown in Tab. 5.3.

Table 5.3: List of experimental parameters.

Cluster source	
Gas	Xenon
Stagnation pressure [bar]	~ 30
Stagnation temperature [K]	~ 290
pulse valve	
Nozzle diameter [μm]	200
Nozzle half angle [degree]	4
Pulse duration [ms]	1.0
Jet delay [ms]	13.2
XFEL	
Photon energy [keV]	11.0
Repetition rate[Hz]	30
Pulse duration [fs]	~ 10
Focus [μm^2, FWHM]	1.4×1.6
Intensity [W/cm^2]	4×10^{17}

NIR	
Photon energy [eV]	1.55
Repetition rate[Hz]	30
Pulse duration [fs]	~ 30
Focus [μm^2, FWHM]	35×40
Intensity [W/cm^2]	4×10^{16}
Ion TOF spectrometer	
Pusher [V]	1,000
Puller [V]	375
Tube [V]	100
MCP [V]	-700
Photo converter [V]	2,300
PMT [V]	-850
MPCCD sensor	
System gain [eV]	17.38
Energy to generate an electron-hole pair [eV]	3.65

5.2 Preprocessing of experimental data

5.2.1 Extraction of "hit" images

MPCCD images and ion TOF spectra were collected every "Run": a group of data. Runs included images and spectra under the same experimental conditions other than XFEL injection. Most of the Runs included 10,100 datasets (10,000 with XFEL injection and 100 without XFEL injection). Totally 2,664,863 images were recorded in the experiment. At the first stage of analysis, the "hit" images, where signals from clusters show up on the MPCCD images, were chosen by the following "HitFinding" procedure:

1. A background image for images in a specific Run was calculated by averaging over 100 images without XFEL injection in the Run. Background correction of an image was done by subtracting the background image from the image.

2. The numerical values $I(x, y)$ of images were normalized as follows:

$$I_{norm}(x,y) = \frac{I - (\bar{I} + k \times \sigma(I))}{norm} \times 255, \tag{5-1}$$

$$\overline{I_{norm}}(x,y) = \begin{cases} 255 & (I_{norm}(x,y) < 0) \\ 255 - I_{norm}(x,y) & (0 < I_{norm}(x,y) < 255) \\ 0 & (I_{norm}(x,y) > 255) \end{cases}. \tag{5-2}$$

   Here $\bar{I}$ is the mean of I, $\sigma(I)$ is the standard deviation of I, $norm$ is a parameter for normalization. This process converts an image into an 8-bit gray-scale image which is suitable for processing by using an image-processing package "OpenCV" [134].

3. An algorithm "FindBlob" in OpenCV was applied to the normalized images $\overline{I_{norm}}(x, y)$ and the hit images were obtained.

FindBlob detects Bragg spots by analyzing regions including pixels with valid signals on an image (so-called blob). The procedure of the FindBlob algorithm is as follows:

1. A step-by-step thresholding starting from $minThreshold$ to $maxThreshold$ with the step size $thresholdStep$ is applied to $\overline{I_{norm}}(x, y)$, which gave multiple binary images.

2. Regions with small areas appearing in the superposition of the multiple binary images are detected as blobs.

3. When the distance between the centers of two blobs is lower than or equal to $minDistBetweenBlobs$, the two blobs are merged to generate one new blob.

4. After merging blobs in the previous process, the centers and radii of blobs are calculated.

5. The blobs with the area over $minArea$ were chosen as the candidates for those corresponding to Bragg spots.

The parameters to set for the HitFinding procedure were shown in Tab. 5.4. After extracting images by using the above procedure, further thresholding in terms of the area of blobs was applied to extract bright Bragg spots from Xe nanocrystals. For this work, the threshold to the area of blobs was set to 0.25 (in the unit of mm), which extracted images with blobs corresponding to the Bragg spots from Xe crystals well.

Table 5.4: List of the values used for the HitFinding.

Parameters	Values
k	2
$norm$ (ADU)	5,000
$minThreshold$	240
$maxThreshold$	255
$thresholdStep$	1
$minDistBetweenBlobs$ (pixel)	10
$minArea$ (pixel)	9

Some hit images extracted by using the HitFinding procedure had one or more than one spot. The statistics of the number of spots in the hit images are shown in Fig. 5.10(a) for the pristine clusters (without irradiation of NIR pulses) and in Fig. 5.10(b) for all images. While most of the hit images had only a single Bragg spot, there were quite a few images having several Bragg spots. Furthermore, some of the images had streaks of Bragg spots. These suggest that poly-crystalline clusters were produced in the experiment and that clusters with stacking fault were also produced. However, the population of images with more than one spot is only a few percents of that of images with only one spot. Therefore, it can be assumed that there is little probability that the images with only one spot came from poly-crystalline clusters. The later discussion will be developed under this assumption.

5.2.2 Calibration of the delay time with the temporal jitter

As described in subsection 3.1.4, temporal jitter, that is the fluctuation of arrival time between XFEL and optical laser pulses, is not avoidable and is crucial to achieving high temporal resolution for pump-probe measurements. The temporal jitters for each shot were obtained by analyzing the CCD images in the arrival timing monitor. This analysis was done by using the software installed in the HPC server of SACLA [135]. Fig. 5.11(a) shows a typical CCD image of the arrival timing monitor collected in the experiment and Fig. 5.11(b) shows a histogram of the temporal jitters taken in one Run. The actual time delays of the XFEL pulses against the NIR pulses for each shot were calibrated using the information of these temporal jitters.

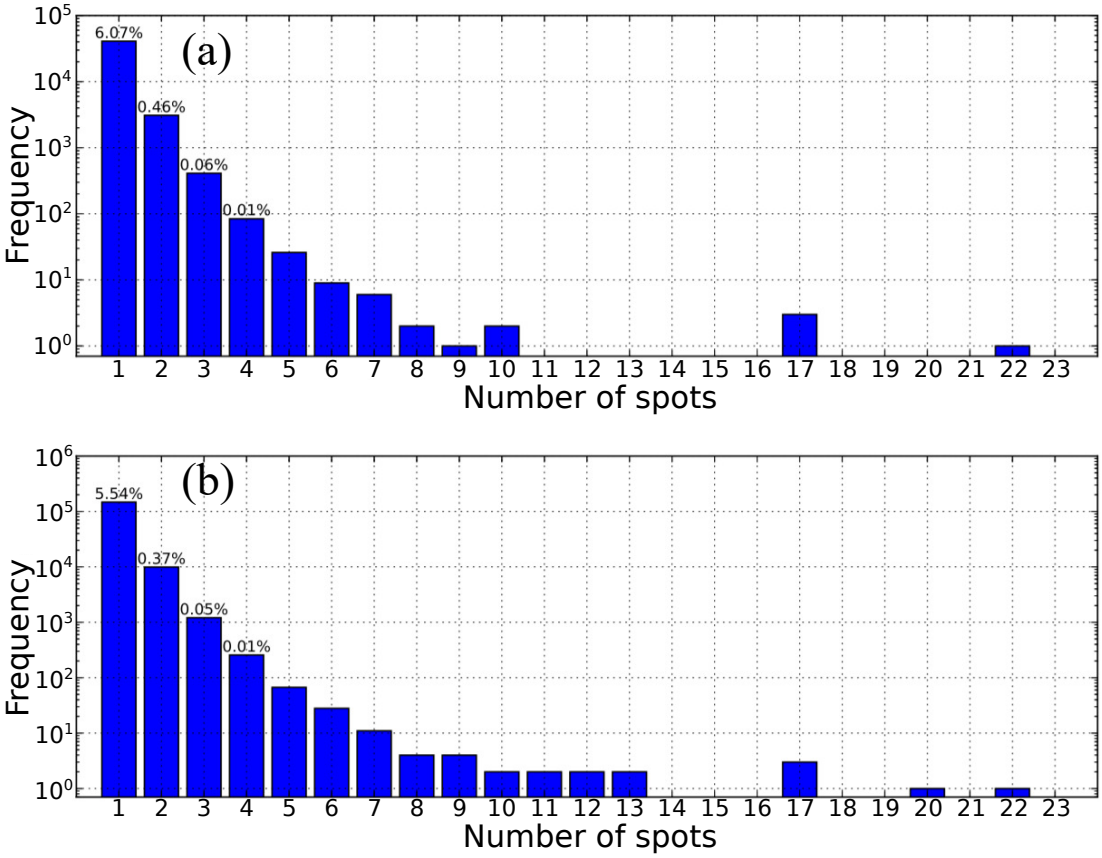

Figure 5.10: The histograms of the number of Bragg spots observed in the hit images for pristine clusters (a) and for all images (b). The numbers on the first four bars from the left side in (a) describe the proportions of the images to the total number of images taken without NIR pulses. The numbers in (b) describe the proportions of the images to the total number of images taken in the whole experiment.

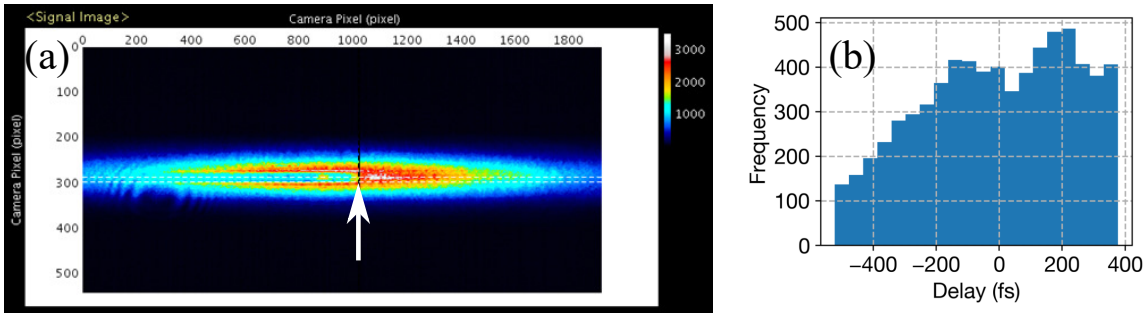

Figure 5.11: Calibration of the temporal jitter. (a) a typical CCD image of the arrival timing monitor. The reduction of transmittance of the GaAs crystal for a NIR pulse is observed. The horizontal position of a gap pointed out by a white arrow reflects on the temporal jitter. (b) A histogram of the temporal jitters taken in one Run.

5.3 Analysis

5.3.1 Determination of the center of image

We determined the actual center of the detector image by using the diffraction pattern of a GaAs crystal. The GaAs crystal on the beam position monitor was used as a reference sample. Fig. 5.12 shows the positions of Bragg spots from the GaAs crystal. We can see a clear Debye-Scherrer ring from the GaAs crystal in the image. To determine (x_0, y_0) more accurately, the value of the threshold to spot area was set to 0.23 mm in this case. (x_0, y_0) was determined to be $(1202, 1225)$ (in the unit of pixel) by minimizing the variance of the radial distance of each spot from the center (x_0, y_0), denoted by f_{err}:

$$f_{err} = \sum_j (r_j - \bar{r})^2, \tag{5-3}$$

$$r_j = \sqrt{(y_j - x_0)^2 + (y_j - y_0)^2}, \tag{5-4}$$

$$\bar{r} = \frac{\sum_j r_j}{N_{spot}}. \tag{5-5}$$

Here (x_j, y_j) is the coordinate of the j-th spot and N_{spot} is the number of Bragg spots shown in Fig. 5.12.

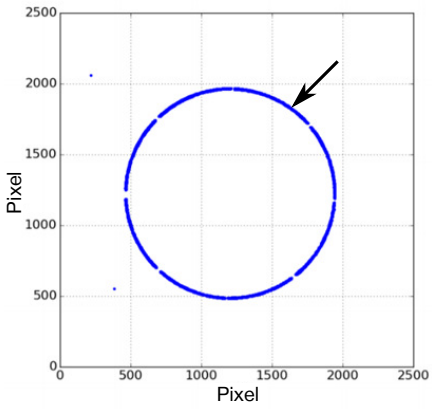

Figure 5.12: The positions of Bragg spots from the GaAs crystal. Spots far from the Debye-Scherrer ring pointed with a black arrow were excluded to determine the actual center of image.

5.3.2 Extraction of the parameters of a Bragg spot

Each Bragg spot has the following parameters which reflect on the properties of an irradiated crystal:

- Radial position of a Bragg spot on the image: the lattice constant of the crystal.
- Intensity: crystal size and XFEL intensity.
- Width: crystal size.
- Direction of the extent of a Bragg spot: other characteristics such as anisotropy of crystal.

To extract these parameters from a Bragg spot, fitting with a 2-dimensional Gaussian curve was applied to Bragg spots. The formula of the fitting curve is expressed as

$$f_{2D}(x,y) = h\exp\left\{-a(x-c_x)^2 - b(x-c_x)(y-c_y) - c(y-c_y)^2\right\} + base, \quad (5\text{-}6)$$

$$a = \frac{\cos^2\theta_{spot}}{2\sigma_x^2} + \frac{\sin^2\theta_{spot}}{2\sigma_y^2}, \quad (5\text{-}7)$$

$$b = \frac{\sin 2\theta_{spot}}{4\sigma_x^2} + \frac{\sin 2\theta_{spot}}{4\sigma_y^2}, \quad (5\text{-}8)$$

$$c = \frac{\sin^2\theta_{spot}}{2\sigma_x^2} + \frac{\cos^2\theta_{spot}}{2\sigma_y^2}, \quad (5\text{-}9)$$

where h is the height of the fitting curve, (c_x, c_y) is the coordinate of the center of Bragg spot, *base* is the baseline level of Bragg spot due to some experimental factor, σ_x and σ_y are the standard deviations along the longitudinal/latitude axes, θ_{spot} is the angle between the longitudinal axis and the horizontal axis in the positive direction (the right-hand side). Fig. 5.13 shows a typical result of the fitting.

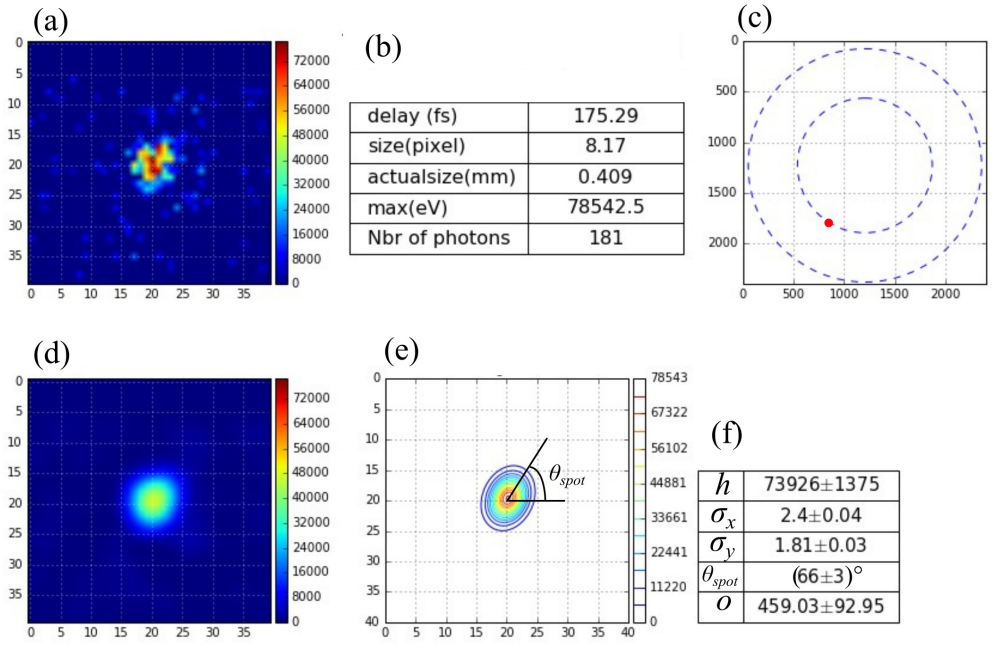

Figure 5.13: A typical result of 2D Gaussian fitting to Bragg spots. (a) Raw image of a Bragg spot. (b) Some parameters derived from the HitFinding. (c) Position of the spot (a red circle). (d) Smoothed spot image. (e) Contour of the 2D Gaussian fitting curve. (f)The parameters derived from the fitting.

5.3.3 Analysis of ion TOF spectrum (NIR irradiation only)

We need information on plasma parameters in the discussion of the structural dynamics of nanoplasma in the following section. Here we deduced the information of laser-generated nanoplasma from ion TOF spectra. Fig. 5.14 shows the TOF spectrum deduced by averaging over 9,164 shots. The procedures of assignment of the charge states and the initial kinetic energies of Xe ions are similar to those described in chapter 4. The procedures gave the averaged charge state Z_{ave} as 30, and the relation between charge state ($q = 3 \sim 8$) and the mean KE of Xe ions shown in the inset of 5.14. The mean KE of Xe ions has a linear dependence on the charge state, suggesting the hydrodynamic expansion of the nanoplasma [26].

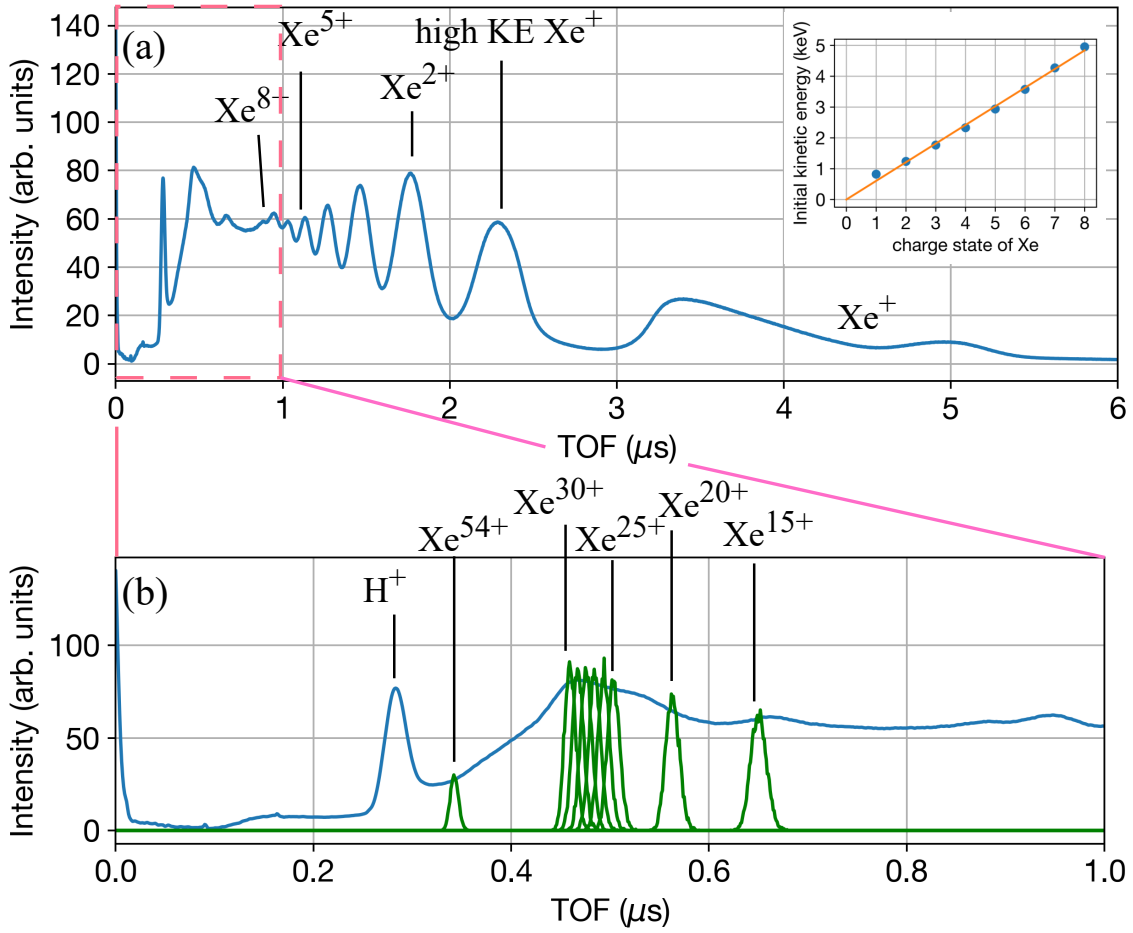

Figure 5.14: The averaged ion TOF spectrum from Xe clusters under the irradiation of the NIR pulses with the intensity of 4×10^{16} W/cm^2. (a) The whole TOF spectrum. (Inset) A KE-q plot for $q = 1 \sim 8$. An orange line in the inset shows the linear fit. (b) A close-up image of the TOF spectra at 0–1 μs. Green lines are the simulated TOF curves for some charge states. For the simulation, ions were assumed to have Gaussian kinetic energy distributions.

5.4 Results and Discussion

By using preprocessing and analysis methods described in sections 5.2 and 5.3, substantial information on the crystalline structure of Xe clusters in the neutral state and the structural changes under the irradiation of NIR laser pulses could be extracted from the datasets. This section will firstly present the results and discussion on Xe nanocrystals in their neutral state, and then on ultrafast structural changes in Xe nanoparticles induced by the irradiation of NIR laser pulses.

5.4.1 Distribution of Bragg spots: virtual powder diffraction

Xe clusters with the averaged radii of 30 $\sim$ 60 nm were irradiated by the NIR pulses and Bragg reflections from the clusters were recorded on the MPCCD sensor. Fig. 5.15 shows an accumulated image of diffraction patterns with a single spot from pristine clusters. Sharp spots from the Xe clusters were observed on the Debye-Scherrer rings corresponding to fcc (111) and fcc (220) of Xe crystal.

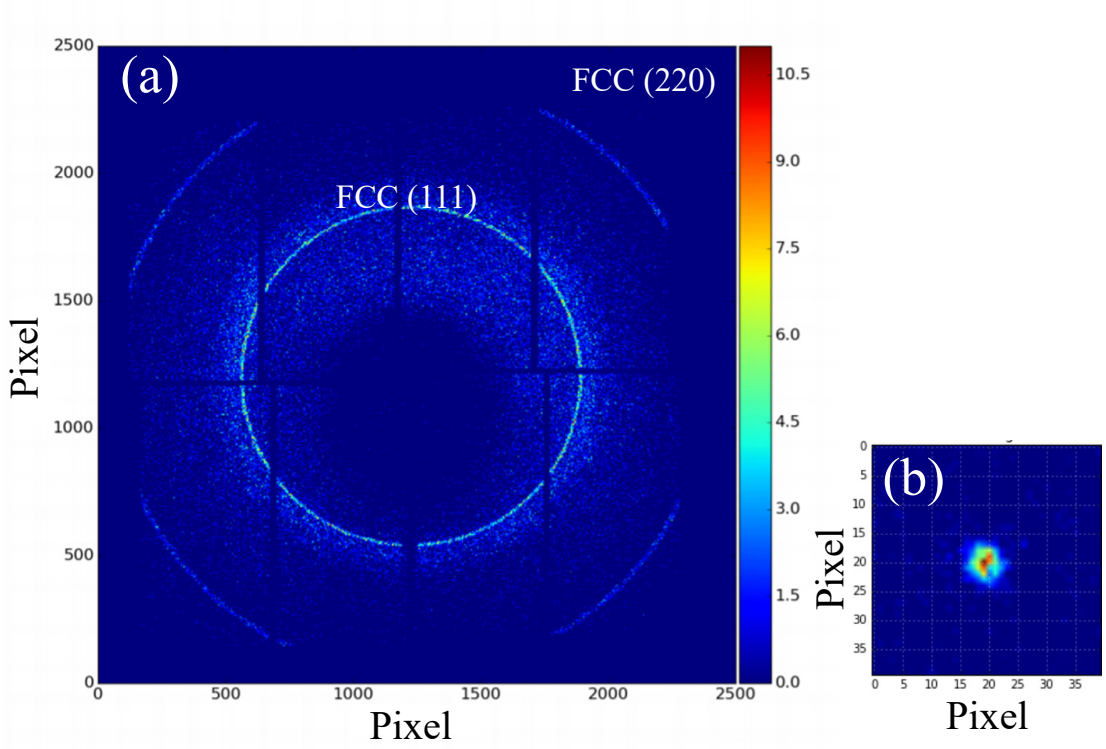

Figure 5.15: (a) An accumulated image of diffraction patterns under the conditions without NIR pulses. Some of the observed Bragg spots made clear Debye-Scherrer rings at the positions corresponding to the fcc (111) and (220) reflections. (b) A typical image of a single Bragg spot.

5.4.2 Assignment of Bragg spots: crystalline structure of Xe clusters in their neutral state

The positions of Bragg spots give information on the crystalline structure (the local order) of the Xe clusters. Fig. 5.16 shows a radial distribution of Bragg spots coming from pristine clusters. It peaks around the momentum transfers corresponding to the fcc (111), (200) and (220) reflections (1.78 Å^{-1}, 2.05 Å^{-1}, 2.90 Å^{-1}, respectively), suggesting fcc lattice structure in the Xe clusters. These observed positions give the lattice constant of the Xe clusters to be 6.13 Å, which is in good agreement with that of bulk Xe [136].

Furthermore, there was a broad peak around the position corresponding to a Bragg reflection from the hcp (101) plane, which suggests that Xe crystals with randomly stacked close-packed (rcp) structure [137] were generated under the adiabatic expansion. This means that the obtained data include both nearly perfect fcc crystals and nearly rcp crystals even at the position of Bragg reflections of fcc lattice planes. However, even in the case of the rcp structure, the profiles of the Bragg spots at the fcc (111) reflection region are identical to those from the perfect fcc structure [137]. That is, the spots appearing at the fcc (111) reflection region (q ~1.78 Å^{-1}) can be treated in the same manner regardless of the difference of stacking.

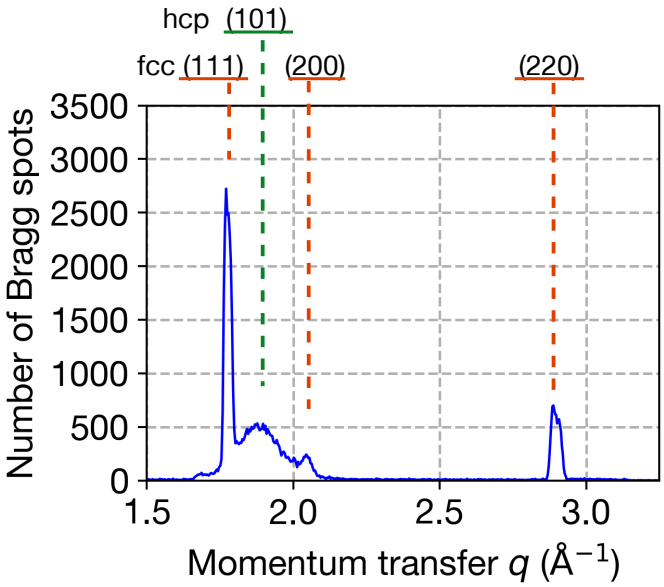

Figure 5.16: A radial distribution of Bragg spots from pristine Xe clusters. Bragg reflections at the positions of fcc (111), (200) and (220) plane were detected. A broad peak at the position of hcp (101) plane was also detected.

5.4.3 Temporal development of the "hit rate" of Bragg spots

As mentioned in chapters 1 and 2, preceding studies have reported that a nanoparticle irradiated by intense laser pulses is highly ionized and changed into nanoplasma promptly, and the nanoplasma expands into the vacuum. That allows one easily to imagine that the local structure of the irradiated nanoclusters is lost during solid-to-nanoplasma transition and following nanoplasma expansion. The disappearance of local structure, called local disordering, leads to the decrease of intensity of Bragg spots and reflects to the changes in their profiles.

The frequency of observation of Bragg spots per XFEL shot is a good measure to evaluate the degree of local disordering, and so did it in the experiment. For the spots at the positions of fcc (111), (200), (220) and hcp (101) regions, the hit rates, defined as the ratio of the number of detected Bragg spots to that of XFEL shots, are plotted as a function of the delay time in Fig. 5.17. For all cases, the hit rate decreased as the time elapsed after irradiation of the NIR pulses. This indicates that the progressive reduction of coherent diffraction from Xe crystals occurs during nanoplasma formation. Its time scale was estimated to be around 100 fs by fitting with an exponential curve, and it is noteworthy that the fcc crystal structure of Xe clusters survives much longer compared to the irradiation period.

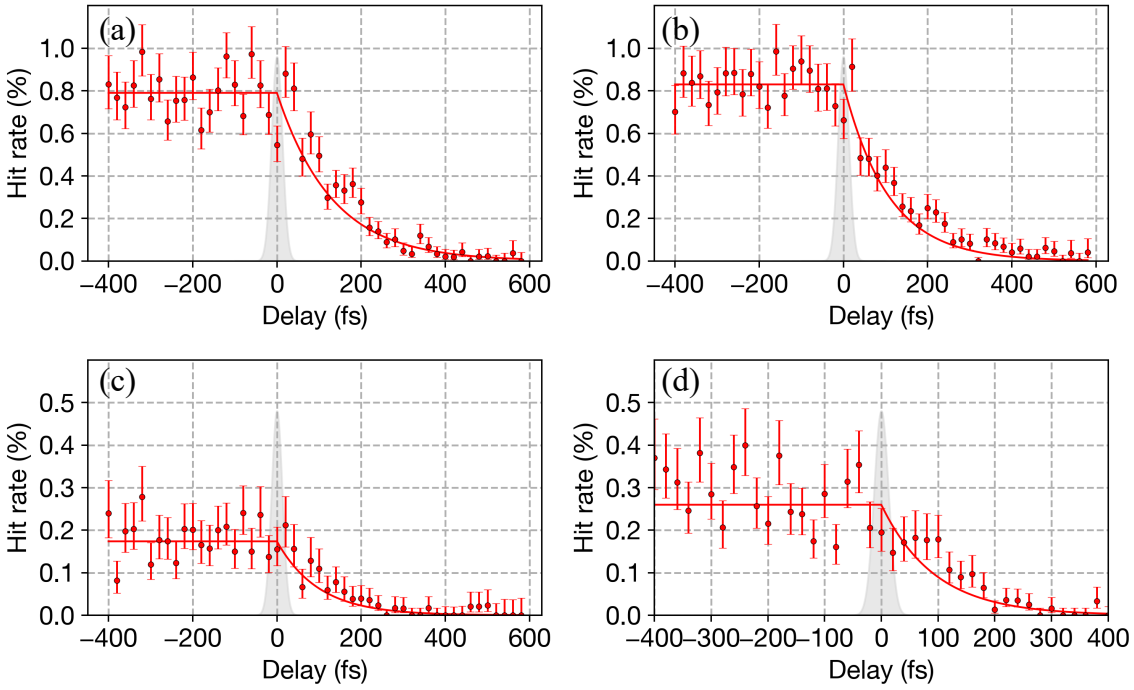

Figure 5.17: Temporal development of the hit rates for Bragg spots around the momentum transfer of (a) fcc (111), (b) hcp (101), (c) fcc (200), and (d) fcc (220). The data points were derived by averaging the whole data in each delay point. The error bars shows the statistical errors. The solid lines are fitting curves.

5.4.4 Temporal development of the lattice constant of Xe nanocrystals

When the lattice constant of a nanocrystal is changed, the momentum transfers of Bragg spots are also changed accordingly. Fig. 5.18 shows the temporal development of the momentum transfer of Bragg spots at the position of fcc (111) reflection, denoted by $\overline{q_{111}}$ for convenience. $\overline{q_{111}}$ did not change within the experimental error which came from the interaction volume of the gas jet with the XFEL beam[1]. This observation suggests that the lattice constant of the Xe fcc crystal under the irradiation of NIR laser pulses is negligible.

As introduced in chapter 1 and discussed in section 2.3.4, a recent time-resolved X-ray pump-X-ray probe WAXS experiment [61] observed shifting of the Bragg reflection to larger momentum transfer in the excited Xe nanoclusters within a few tens fs. This suggests that the lattice contraction of Xe nanocrystals is induced by the irradiation of the 10-fs hard X-ray laser pulses. The authors interpreted the lattice contraction as a consequence of the prompt changes in the potential energy landscape upon inner-core ionization and following decay processes. The present results, however, show quite different behavior from the hard X-ray induced structural dynamic. As mentioned in chapter 2, intense NIR laser pulses dominantly interact with valence electrons of Xe atoms, and the largest excitation cross sections for the NIR pulses are excitation of the valence electrons and inverse Bremsstrahlung heating [26]. Hence, it is speculated that changes in the density profiles of the excited nanoparticles are quite different in the two spectral regimes (i.e. NIR and hard X-ray) and the structural evolution of the Xe nanocrystals reflects such different excitations. At present, it is so difficult to give a fully qualified interpretation in this matter, and theoretical support describing the complex and correlated electron and nuclear dynamics will be necessary.

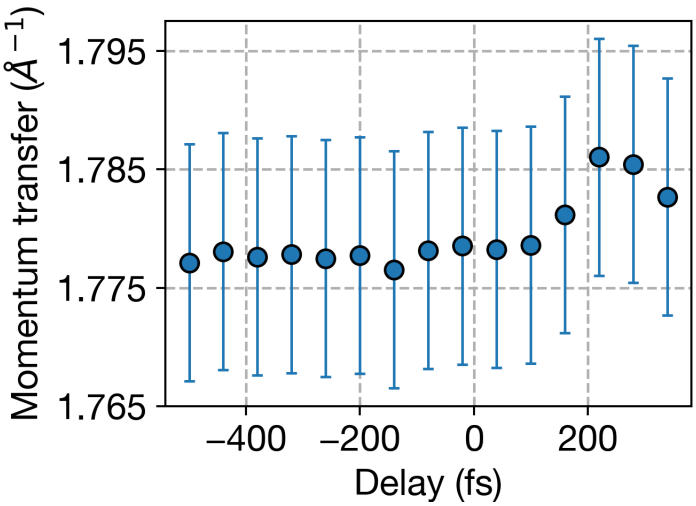

Figure 5.18: Temporal development of the momentum transfer of the Bragg spots at the position of fcc (111) reflection. The data points were derived by averaging the whole data in each delay point. The error bars consist of the standard deviations and the experimental errors.

[1]Even if the change appearing after $\sim$ 200 fs is regarded as a true change, the change is only 0.5 % compared to q_{111} for pristine Xe clusters.

5.4.5 Data filtering for further discussion

Before proceeding further discussions based on the other parameters of the Bragg spots, it should be mentioned that the datasets have to be filtered to make a clear discussion for the following reason. Firstly, the supersonic jet expansion technique for cluster generation always leads to distribution in cluster sizes [108]. Secondly, Each Xe cluster interacted with the XFEL pulses somewhere in the finite focal size of the XFEL pulses. This means that the X-ray scattering signal is convoluted with the focal volume intensity distribution. Hence, the datasets obtained in the experiment include signals taken under various conditions of the cluster size and the XFEL intensity. A schematic describing the above factors is shown in Fig. 5.19.

As discussed in chapter 4, the characteristics of the structural dynamics could be washed out by the above factors without data filtering. In order to give a clearer discussion with a reliable dataset, only the 5% most intense signals at each delay point were taken into account, which can be regarded to come from the largest clusters in the most intense part of the XFEL focal volume[2]. Considering the discussion on the crystalline structure described in the previous sections, and the statistics of the dataset consisting of the 5% most intense signals, the following discussions will focus on the spots observed t the region of the fcc (111) reflection (q ~1.78 Å^{-1}).

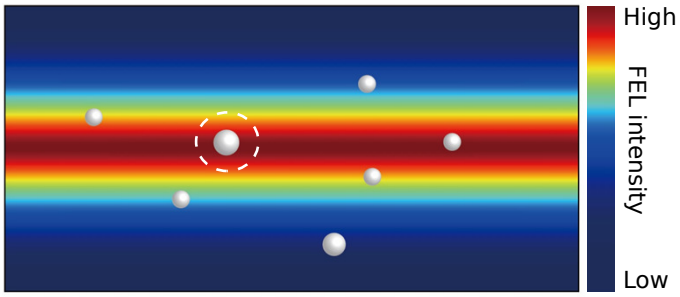

Figure 5.19: A schematic of the X-ray scattering under distributions in the cluster size and the XFEL intensity. The visualization is a courtesy of A. Niozu. For clear discussion, datasets obtained from largest clusters in the most intense region of XFEL pulses (pointed out by a white dashed-line circle) were extracted.

5.4.6 Temporal development of the intensity and the width of Bragg spots

Fig. 5.20(a) shows the characteristic images of the Brag spots from fcc (111) reflection at various delay times of the XFEL pulses. It shows that bright Bragg spots were observed before NIR irradiation and their intensity decreased after NIR irradiation. More quantitatively, Figs. 5.20(b)–(c) show the temporal development of the intensity $I(t)$ (t is the delay time of the XFEL pulses) and the FWHM of the Bragg spots from the Xe clusters $FWHM(t)$. Here $I(t)$ was calculated by a

[2]The temporal development of the intensity and width of the Bragg spots derived from the whole dataset is shown in the appendix.

product of the height and the area of the Bragg spot, $2\pi h \times \sigma_x \times \sigma_y$, and $FWHM(t)$ was calculated by the geometric average of the two widths $\sqrt{2\log 2\sigma_x\sigma_y}$. The data show that the spot intensity decreased after irradiation of the NIR pulses, which suggests the reduction of the local order in the Xe crystals and is consistent with the decrease of the hit rate. Simultaneously, the spot width increased up to a few tens of percent within 400 fs after NIR irradiation.

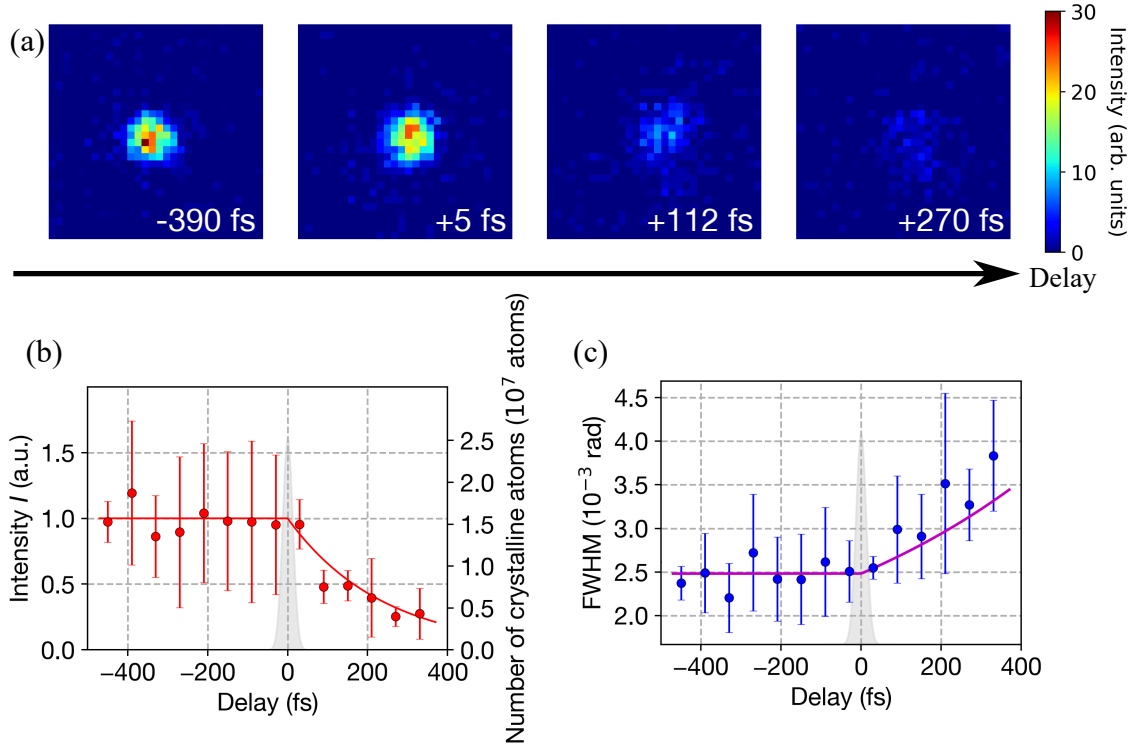

Figure 5.20: Delay dependence of the profiles of Bragg spots from fcc (111) reflection. (a) Characteristic spot images at some delay times. The images are drawn in the same color scale. (b) Temporal evolution of the spot intensity. The solid red line is a fitting curve consisting of an exponential curve. (c) Temporal evolution of the spot width. The solid magenta line is a curve based on the surface disorder model. Both solid lines are described in the main text. The shadow profiles at 0 fs in (b)–(c) represent the intensity profile of the NIR laser pulses. The error bars of (b) and (c) show standard deviations.

5.4.7 How local disordering proceeds during/after nanoplasma formation?

The simultaneous decrease in intensity and increase in width of the Bragg spots as shown in Fig. 5.20 indicates that the volume of the crystalline part in a Xe cluster decreases non-uniformly. Our results raise a question: how and from where does the local disordering proceed during/after nanoplasma formation? There are various possibilities of local disordering, but here three typical models shall be investigated:

- Core disorder: the random displacement of the position of the component atoms in a crystal (simply called "disordering" in this context) proceeds from the core to the surface of the crystal.

- Random disorder: disordering proceeds uniformly in a crystal.
- Surface disorder: disordering proceeds from the surface to the core of a crystal.

These models are depicted in Fig. 5.21. The dependence of the intensity and width of a Bragg spot on the degree of disordering for each model was simulated with a spherical fcc crystal composed of 10^4 atoms (see the Supplemental Material of Ref. [132]). The results of the simulation are shown in Fig. 5.22 and the followings were found:

- When a core disorder occurred, the intensity of a Bragg spot from fcc (111) reflection did decrease but its width did not get broader as the degree of disordering increased.
- When disordering occurred randomly in the target sphere, the spot width was not changed while the spot intensity decreased. This is consistent with a well-known fact that a uniform random displacement of the atoms in the crystal, which can be attributed to the thermal motion of atoms and represented with the Debye-Waller factor, would not influence the spot width [65].
- When a surface disorder occurred, the intensity of a Bragg spot from fcc (111) reflection decreased and its width increased simultaneously.

Therefore, the surface disorder is the model that can explain the experimental observations. Although there could be other complicated models of disordering, it can be inferred from the above results that disordering of the outer (surface) region of a crystal contributes to the increase of Bragg spot width than disordering of its inner (core) region.

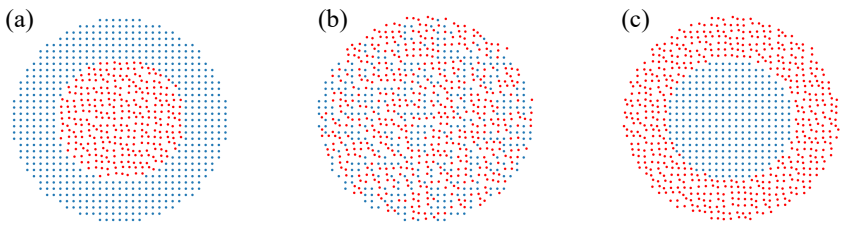

Figure 5.21: Three models to investigate for interpretation of the experimental observation. (a) a core disorder. (b) a random disorder. (c) a surface disorder. In each model, blue points show the atoms on the lattice points and red ones show the atoms affected by disordering. From the Supplementary Material of Ref. [132]. Reprinted with permission from APS.

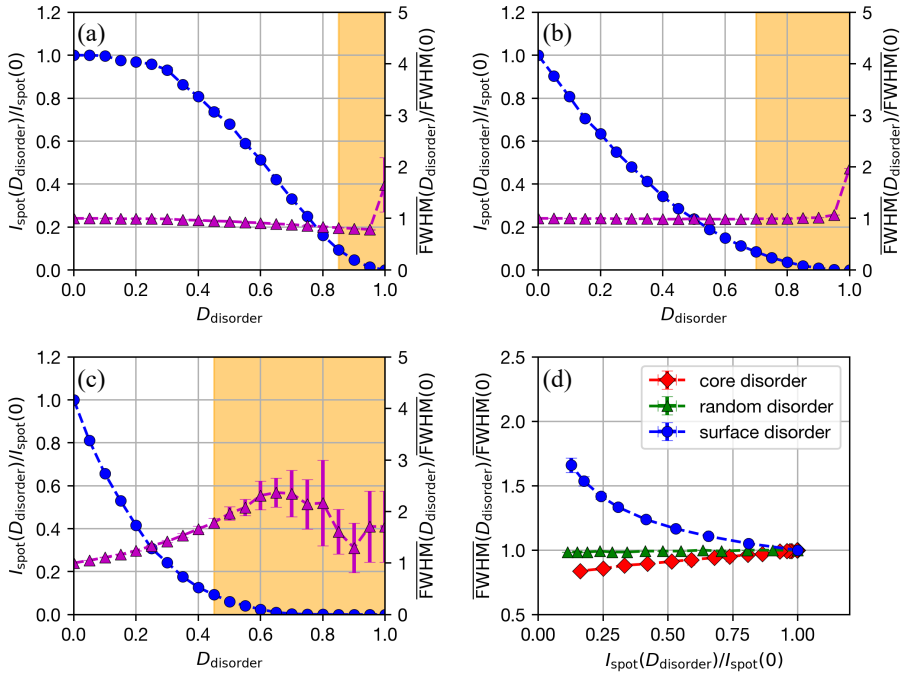

Figure 5.22: Development of the intensity I_{spot} and the FWHM $\overline{\mathrm{FWHM}}$ of Bragg spots from fcc (111) reflection in the core disorder (a), the random disorder (b) and the surface disorder (c) in the simulation. Here D_{disorder} is the degree of disordering (0–1). In (a)–(c), $I_{\mathrm{spot}}(D_{\mathrm{disorder}})/I_{\mathrm{spot}}(0)$ is plotted by blue circles with a dotted line, and $\overline{\mathrm{FWHM}}(D_{\mathrm{disorder}})/\overline{\mathrm{FWHM}}(0)$ is plotted by magenta triangles with a dotted line (D_{disorder} represents the degree of disordering). Each data point shows the average value around 10 generated samples. Data points in the orange shadow regions in (a)–(c) are not reliable in terms of the statistical error. (d) Correlation plots between $I_{\mathrm{spot}}(D_{\mathrm{disorder}})/I_{\mathrm{spot}}(0)$ and $\overline{\mathrm{FWHM}}(D_{\mathrm{disorder}})/\overline{\mathrm{FWHM}}(0)$ in each model. The error bars in (a)–(d) show the standard deviations. From the Supplementary Material of Ref. [132]. Reprinted with permission from APS.

5.4.8 Surface disorder model and the temporal evolution of the core radius

Based on the above simulation results, a surface disorder model of a Xe crystal with a spherical shape and fcc lattice structure was developed to perform a consistency check of the observed temporal evolution of the spot intensity and the spot width. In a first step, the spot intensity is assumed to be proportional to the crystal volume and the time-dependent decrease of the spot intensity reflects the reduction of the crystal volume: $I(t) \propto V(t) \propto r^3(t)$. Then the crystal radius can be written as

$$r(t) = \begin{cases} r_0 & (t < 0) \\ r_0 \left(\frac{I(t)}{I_0}\right)^{1/3} & (t > 0) \end{cases}, \tag{5-10}$$

where r_0 is the radius of cluster in the neutral state, I_0 is the spot intensity from pristine clusters. In a second step, the spot width is assumed to be composed of the three factors: crystal size, distortion of crystal, and the instrumental factor. The crystal size factor is calculated with the Scherrer equation [75] (see subsection 2.2.3), which relates the FWHM of Bragg spot β and the size of nanoscale crystal. Actually the spot width is considered to be composed of the crystal size effect and other factors. Here we took the distortion and instrumental factors into account, and assumed that these factors are independent of the delay time. By substituting the characteristic length τ in Eq. 2-56 with the cube root of the particle volume $(4\pi r^3(t)/3)$, the size factor of the spot width, β_{size}, can be expressed as

$$\beta_{size}(t) = \frac{2\lambda}{3r(t)\cos\theta}. \tag{5-11}$$

The model for the spot width is written by

$$\beta(t) = \beta_{size}(t) + \beta_{distort} + \beta_{inst} \tag{5-12}$$

where $\beta_{distort}$ and β_{inst} are the distortion and instrumental factors, respectively.

A trend line of the temporal evolution of the spot intensity was derived by fitting with an exponential curve and is shown in Fig. 5.22(b), from which the time scale of the intensity decrease was estimated to be around 100 fs. The Bragg spot width calculated by combining the trend line of the spot intensity and the above model is shown in Fig. 5.22(c) as a solid magenta line. The modeled spot width agrees well with the measured evolution of the spot width, which shows that there was a clear correlation between the spot intensity and the spot width. The data show that the superheated clusters lose crystalline order from their surface with an ever shrinking crystal core.

From the data and with Eq. 5-12, the average radius of the crystalline particle core as a function of delay can be inferred. Fig. 5.23(a) shows the temporal development of the core radius. The crystalline core radius is stable around 60 nm in the neutral state but shrinks rapidly upon the excitation by NIR laser pulses. The present result is qualitatively similar to an earlier ultrafast

imaging experiment using SAXS which is sensitive to the envelope of the particle [48]. This previous experiment revealed that the nanoplasma expansion proceeds via a developing density gradient at the surface of a nanoparticle alike non-thermal surface melting. However, no information about the inner structure could be obtained in the previous experiment, for the SAXS imaging is less sensitive to the modulation of the local order in the samples. The present data show that the cluster core in the nanoplasma maintains a crystalline bulk-like structure long after the NIR pump pulse is over, but the crystalline fraction is reduced over time from the surface (hereafter defined shrinkage). From Fig. 5.23(a) and the above model, the speed of the core shrinkage can be estimated to be 7×10^4 m/s. The process inferred from the comparison between the data and the model is depicted in Fig. 5.23(b).

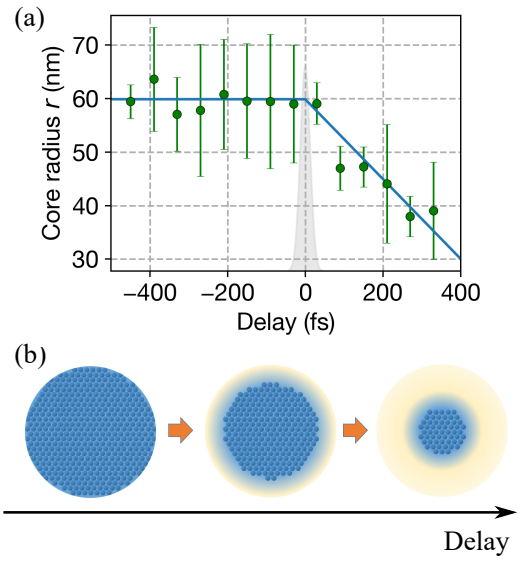

Figure 5.23: Temporal evolution of the core radius of a Xe crystal and a scheme of cluster disordering. (a) Temporal evolution of the core radius of a Xe crystal. The solid line is a guide for the eyes that expresses a linear decrease. The error bars show standard deviations. (b) A scheme of cluster disordering that proceeds from the surface and is consistent with our experiments.

5.4.9 Interpretation of the experimental results

With the knowledge from previous studies about non-linear NIR laser–cluster interactions and nanoplasma formation [26, 27, 70] and based on the observed results, it can be discussed what proceeded in the present experiment. At the early stage of laser–cluster interaction, many electrons are emitted via TI or BSI, and the nanoscale cluster becomes positively charged. Electrons subsequently released are confined by the developing Coulomb potential, which results in the formation of a non-equilibrium nanoplasma. During the laser irradiation, electrons gain energy from the laser field and the cluster is heated via inverse Bremsstrahlung processes. The nanoplasma expands into vacuum due to the internal pressure of the electron gas in the nanoplasma (hydrodynamic expansion) as well as the Coulomb forces (Coulombic expansion). In general, the nanoplasma expansion

is Coulombic for small clusters, and hydrodynamic for large clusters [26, 70, 79]. In the present situation where very large clusters were irradiated by NIR laser pulses, hydrodynamic expansion with the plasma speed of sound is predicted [26, 46, 138].

The relevant plasma parameters could allow giving insight into the present results. From fitting to the ion spectrum observed under the condition where Xe clusters were irradiated only by the NIR laser (as shown in a previous section), an average charge state Z was estimated to be 30 and a resulting electron density n_e was $4 \times 10^{23}/\mathrm{cm}^3$. Using the experimentally determined Z and n_e in full plasma simulations with FLYCHK [139], an electron temperature T_e was also estimated to be ~300 eV. With these parameters, an electron-ion equilibrium time τ_{e-i} [73] of ~350 fs, and the plasma speed of sound, described by Eq.2-57, was on the order of 8×10^4 m/s.

The plasma sound speed determines the speed of hydrodynamic expansion, and interestingly are close to the measured core shrinking speed (7×10^4 m/s). So far the interior dynamics of the non-equilibrium nanoplasmas have remained elusive. With the data obtained in the present experiment, one can connect the previous imaging studies on the surface dynamics in nanoplasma [48] to the structural dynamics in the nanoplasma core. The imaging studies showed an expansion of nanoplasma from its surface, and the present results show a continuous shrinking of the volume of the crystalline core. By connecting the previous data set of surface expansion/softening (exterior dynamics) to the core shrinking and loss of the crystalline order from the surface (interior dynamics), it can be concluded that the local disordering starts on the surface and propagates to the internal core with a speed compatible with the plasma sound speed. This interpretation is consistent with the results from ion TOF studies on shell expansion in core-shell-structure clusters [29, 43] and theoretical modeling of laser-driven hydrogen clusters [55]. In particular, the experimentally determined core shrinking speed is in good agreement with a theoretical study on the expansion dynamics of hydrogen nanoplasma in intense laser fields [55]. However, the present data set can give further insight that even in the highly excited non-equilibrium state, the nanoplasma core retains its crystalline bulk structure and density beyond the initially driving NIR pulse and even beyond τ_{e-i}. One can interpret from the present data set that the local disordering in nanoplasma proceeds from the surface towards the core, and that the core structure is initially protected and the bulk lattice configuration of the nanoplasma is maintained until the surface disordering has propagated into the core. For a full understanding of the complex laser-induced dynamics, theoretical studies including the full ionization processes and plasma dynamics [55, 140] will need to be performed and compared to the present data set.

5.5 Summary of results and discussion II

In this chapter, ultrafast and atomic-scale structural changes in nanoplasma have been investigated with the time-resolved WAXS experiment at SACLA. It was revealed that the crystalline order in a Xe cluster to nanoplasma transition is maintained long after the driving laser pulse is over. Based on the diffraction data in conjunction with previous studies, it can be concluded that the local disordering in nanoplasma proceeds from the surface to the core with a speed compatible with the plasma speed of sound. The findings provide new insight into the structural dynamics of highly non-equilibrium nanoplasma states, their formation, and their evolution.

Chapter 6

Summary and outlook

6.1 Review of the present work

The present work consists of two major topics: development of experimental schemes combining multiple spectroscopy with coherent diffractive imaging using XFEL pulses provided from SACLA, and investigation of static structure and dynamic structural changes of nanoscale particles. Intense and ultrashort laser pulses in the hard X-ray spectral regime have given opportunities to investigate the structure of nanoscale samples regardless of its crystallinity under the principle of diffraction before destruction [20]. This ensures that coherent diffractive imaging (CDI) can take snapshots of changes in the structure of samples exposed to a laser field. Experimental schemes combining CDI with spectroscopies allow one to explore the laser–matter interaction by correlating structural changes with the benefits of the existing abundant knowledge obtained from other spectroscopic signals such as ion spectra [47, 48, 61, 82]. The present work provides and validates an experimental scheme for such multispectroscopic measurements of nanoparticles with XFEL pulses at SACLA. As applications of the experimental scheme presented, this work investigates the morphology and the local order of pristine Xe nanoclusters, and furthermore ultrafast structural changes in nanoplasma induced by intense NIR laser pulses.

For the first experiment of this work (chapter 4), an experimental scheme to collect SAXS signals in coincidence with ion TOF spectra and fluorescence spectra on the shot-by-shot basis was developed. By using the scheme with coherent X-ray pulses available at SACLA, the envelopes of single sub-micron Xe clusters generated in adiabatic expansion was investigated. The observed diffraction patterns reflected on the morphological characteristics of Xe clusters. While most of the observed Xe clusters had spherical shapes, there were also non-spherical shaped Xe clusters indicating the occurrence of the cluster–cluster coagulation [129]. This observation is well consistent with precedent studies using CDI with soft X-ray pulses [44, 45, 47]. Other than structural features of Xe clusters, Diffraction patterns also provide the cluster sizes and the actual fluences at the interaction point for each XFEL shot. By sorting the ion and fluorescence signals according to the extracted cluster sizes

and fluences, clear correlations between these observables could be found. Firstly, the amount of fluorescence photons shows a clear correlation between the scattering intensity, which confirms that fluorescence and scattering signals came from the same targets for each XFEL shot. The photon energy of fluorescence photons corresponding to the fluorescence energy of Xe atomic L_α and L_β lines was not changed with the XFEL fluence. These photons can be attributed to fluorescence from core-ionized Xe atoms. Secondly, both the maximum charge state and the apparent mean charge state of Xe ions increased as the XFEL fluence got higher. The result agrees well with the precedent studies [46, 49] but less steeply compared to the soft X-ray excited cases, which might come from the difference of the absorption cross-section and the efficiency of heating following ionization. With these results, the first experiment substantiated the effectiveness of the multispectroscopic approach that enables to elucidate laser–matter interaction in the hard X-ray spectral regime without data averaging due to the sample size distribution and the laser intensity profile [125].

In the second experiment (chapter 5), another experimental scheme utilizing the shot-by-shot multispectroscopy validated by the first experiment and a pump-and-probe WAXS technique was developed at SACLA. The scheme was applied to the investigation of the static structure and structural changes in Xe nanoscale clusters induced by intense NIR laser field. NIR laser pulses heated Xe clusters, and scattering signals of XFEL pulses irradiating the clusters with temporal delays against the NIR pulses were collected by an SWD MPCCD sensor for each shot. Irradiation of NIR laser pulses did change the local structure of crystalline Xe clusters and the structural changes reflected on the profiles of Bragg spots. After irradiation of NIR pulses, the probability of observation of Bragg spots from each reflection plane decreased drastically within a few hundred fs, which indicated a prompt decrease of the crystalline volume in the heated Xe clusters. For a clear discussion, a data filtering was applied which focuses on the signals taken under the condition where larger clusters are irradiated by the most intense part of the XFEL laser profile. The spot intensity decreased with the temporal delay and simultaneously the spot width got broader. These behaviors can be certainly attributed to a loss of the crystalline order in a Xe cluster. Using a numerical simulation and modeling shows the crystalline order got lost from the surficial part of the cluster into the core part. Furthermore, it was clarified that the core shrinkage proceeded with the speed on the same order as the plasma sound speed, consistent with the observations in the preceding SAXS studies [49, 82]. Even though theoretical studies are necessary to fully understand the physics in the dynamics, this second experiment provides new insight into the structural dynamics in nanoplasma formation and its development on the atomic scale [132].

6.2 Future perspectives

The experimental schemes presented in this work have a possibility to study the structure of any type of samples with various spatial scale ranging from the overall morphology to the local order. The schemes can be applied to transient structural changes of samples in their excited states with the high temporal resolution up to a few ten femtoseconds[1]. The usefulness of the schemes has been proven at SACLA, and similar configurations of experimental setups can be used at other XFEL facilities.

The findings of this work have implications in various fields such as cluster science and studies on dynamics in non-equilibrium states including nanoplasma. As for the nanoplasma dynamics, investigations of structural changes focusing on the following viewpoints need to be performed to get a more profound insight into the physics in nanoplasma: wavelength dependence, laser intensity dependence, and structural changes in complicate systems. As mentioned in chapter 2 and shown in Fig. 2.5, ionization mechanism and following heating processes depend on both the wavelength and intensity of the excitation laser [70], from which one can easily guess that the way of disordering of atomic configuration also depends on the properties of the excitation laser. Additionally, these processes are also dependent on the components of a target and its surroundings. The WAXS experiments [61, 132] report that the local order of a Xe crystal under a NIR pulse behaves differently from that under a hard X-ray pulse while SAXS experiments [48, 82] report that a Xe nanoplasma gets its electron density heavily changed from its surface in both the NIR and the hard X-ray regimes. Only a few experiments on the structural changes in nanoplasma by using coherent diffractive imaging were performed and further investigation is expected.

[1] The temporal resolution depends on facilities and apparatuses.

References

[1] W. C. Röntgen. Nobel Prize for "his discoveries and research in the field of X-ray spectroscopy", 1901.

[2] M. v. Laue. Nobel Prize for "his discovery of the diffraction of X-rays by crystals", 1914.

[3] S. W. H. Bragg and W. L. Bragg. Nobel Prize for "their services in the analysis of crystal structure by means of X-rays", 1915.

[4] A. H. Zewail. Femtochemistry. Past, present, and future. Pure and Applied Chemistry, 72(12):2219–2231, 2019 2000. ISSN 13653075. doi: 10.1351/pac200072122219. URL https://www.degruyter.com/view/j/pac.2000.72.issue-12/pac200072122219/pac200072122219.xml.

[5] P. B. Corkum and F. Krausz. Attosecond science. Nature Physics, 3(6):381–387, 2007. ISSN 1745–2481. doi: 10.1038/nphys620. URL https://doi.org/10.1038/nphys620.

[6] L. Young, E. P. Kanter, B. Krässig, Y. Li, A. M. March, S. T. Pratt, R. Santra, S. H. Southworth, N. Rohringer, L. F. DiMauro, G. Doumy, C. A. Roedig, N. Berrah, L. Fang, M. Hoener, P. H. Bucksbaum, J. P. Cryan, S. Ghimire, J. M. Glownia, D. A. Reis, J. D. Bozek, C. Bostedt, and M. Messerschmidt. Femtosecond electronic response of atoms to ultra-intense x-rays. Nature, 466(7302):56–61, 2010. ISSN 1476–4687. doi: 10.1038/nature09177. URL https://doi.org/10.1038/nature09177.

[7] B. Rudek, S.-K. Son, L. Foucar, S. W. Epp, B. Erk, R. Hartmann, M. Adolph, R. andritschke, a. Aquila, N. Berrah, C. Bostedt, J. Bozek, N. Coppola, F. Filsinger, H. Gorke, T. Gorkhover, H. Graafsma, L. Gumprecht, a. Hartmann, G. Hauser, S. Herrmann, H. Hirsemann, P. Holl, a. Hömke, L. Journel, C. Kaiser, N. Kimmel, F. Krasniqi, K.-U. Kühnel, M. Matysek, M. Messerschmidt, D. Miesner, T. Möller, R. Moshammer, K. Nagaya, B. Nilsson, G. Potdevin, D. Pietschner, C. Reich, D. Rupp, G. Schaller, I. Schlichting, C. Schmidt, F. Schopper, S. Schorb, C.-D. Schröter, J. Schulz, M. Simon, H. Soltau, L. Strüder, K. Ueda, G. Weidenspointner, R. Santra, J. Ullrich, A. Rudenko, and D. Rolles. Ultra-efficient ionization of heavy atoms by intense X-ray free-electron laser pulses. Nature Photonics, 6:858–865, Nov 2012. URL https://doi.org/10.1038/nphoton.2012.261.

[8] K. Motomura, H. Fukuzawa, S.-K. Son, S. Mondal, T. Tachibana, Y. Ito, M. Kimura, K. Nagaya, T. Sakai, K. Matsunami, S. Wada, H. Hayashita, J. Kajikawa, X.-J. Liu, R. Feifel, P. Johnsson, M. Siano, E. Kukk, B. Rudek, B. Erk, L. Foucar, E. Robert, C. Miron, K. Tono, Y. Inubushi, T. Hatsui, M. Yabashi, M. Yao, R. Santra, and K. Ueda. Sequential multiphoton multiple ionization of atomic argon and xenon irradiated by x-ray free-electron laser pulses from SACLA. Journal of Physics B: Atomic, Molecular and Optical Physics, 46(16):164024, aug 2013. doi: 10.1088/0953-4075/46/16/164024. URL https://doi.org/10.1088%2F0953-4075%2F46%2F16%2F164024.

[9] H. Fukuzawa, S.-K. Son, K. Motomura, S. Mondal, K. Nagaya, S. Wada, X.-J. Liu, R. Feifel, T. Tachibana, Y. Ito, M. Kimura, T. Sakai, K. Matsunami, H. Hayashita, J. Kajikawa, P. Johnsson, M. Siano, E. Kukk, B. Rudek, B. Erk, L. Foucar, E. Robert, C. Miron, K. Tono, Y. Inubushi, T. Hatsui, M. Yabashi, M. Yao, R. Santra, and K. Ueda. Deep Inner-Shell Multiphoton Ionization by Intense X-Ray Free-Electron Laser Pulses. Phys. Rev. Lett., 110:173005, Apr 2013. doi: 10.1103/PhysRevLett.110.173005. URL https://link.aps.org/doi/10.1103/PhysRevLett.110.173005.

[10] B. Erk, R. Boll, S. Trippel, D. Anielski, L. Foucar, B. Rudek, S. W. Epp, R. Coffee, S. Carron, S. Schorb, K. R. Ferguson, M. Swiggers, J. D. Bozek, M. Simon, T. Marchenko, J. Küpper, I. Schlichting, J. Ullrich, C. Bostedt, D. Rolles, and A. Rudenko. Imaging charge transfer in iodomethane upon x-ray photoabsorption. Science, 345(6194):288–291, 2014. ISSN 0036–8075. doi: 10.1126/science.1253607. URL https://science.sciencemag.org/content/345/6194/288.

[11] T. Takanashi, N. V. Golubev, C. Callegari, H. Fukuzawa, K. Motomura, D. Iablonskyi, Y. Kumagai, S. Mondal, T. Tachibana, K. Nagaya, T. Nishiyama, K. Matsunami, P. Johnsson, P. Piseri, G. Sansone, A. Dubrouil, M. Reduzzi, P. Carpeggiani, C. Vozzi, M. Devetta, M. Negro, D. Faccialà, F. Calegari, A. Trabattoni, M. C. Castrovilli, Y. Ovcharenko, M. Mudrich, F. Stienkemeier, M. Coreno, M. Alagia, B. Schütte, N. Berrah, O. Plekan, P. Finetti, C. Spezzani, E. Ferrari, E. Allaria, G. Penco, C. Serpico, G. De Ninno, B. Diviacco, S. Di Mitri, L. Giannessi, G. Jabbari, K. C. Prince, L. S. Cederbaum, P. V. Demekhin, A. I. Kuleff, and K. Ueda. Time-Resolved Measurement of Interatomic Coulombic Decay Induced by Two-Photon Double Excitation of Ne_2. Phys. Rev. Lett., 118:033202, Jan 2017. doi: 10.1103/PhysRevLett.118.033202. URL https://link.aps.org/doi/10.1103/PhysRevLett.118.033202.

[12] T. Takanashi, K. Nakamura, E. Kukk, K. Motomura, H. Fukuzawa, K. Nagaya, S.-i. Wada, Y. Kumagai, D. Iablonskyi, Y. Ito, Y. Sakakibara, D. You, T. Nishiyama, K. Asa, Y. Sato, T. Umemoto, K. Kariyazono, K. Ochiai, M. Kanno, K. Yamazaki, K. Kooser, C. Nicolas, C. Miron, T. Asavei, L. Neagu, M. Schöffler, G. Kastirke, X.-J. Liu, A. Rudenko, S. Owada, T. Katayama, T. Togashi, K. Tono, M. Yabashi, H. Kono, and K. Ueda. Ultrafast Coulomb explosion of a diiodomethane molecule induced by an X-ray free-electron laser pulse. Phys.

Chem. Chem. Phys., 19:19707–19721, 2017. doi: 10.1039/C7CP01669G. URL http://dx.doi.org/10.1039/C7CP01669G.

[13] H. Fukuzawa, T. Takanashi, E. Kukk, K. Motomura, S.-i. Wada, K. Nagaya, Y. Ito, T. Nishiyama, C. Nicolas, Y. Kumagai, D. Iablonskyi, S. Mondal, T. Tachibana, D. You, S. Yamada, Y. Sakakibara, K. Asa, Y. Sato, T. Sakai, K. Matsunami, T. Umemoto, K. Kariyazono, S. Kajimoto, H. Sotome, P. Johnsson, M. S. Schöffler, G. Kastirke, K. Kooser, X.-J. Liu, T. Asavei, L. Neagu, S. Molodtsov, K. Ochiai, M. Kanno, K. Yamazaki, S. Owada, K. Ogawa, T. Katayama, T. Togashi, K. Tono, M. Yabashi, A. Ghosh, K. Gokhberg, L. S. Cederbaum, A. I. Kuleff, H. Fukumura, N. Kishimoto, A. Rudenko, C. Miron, H. Kono, and K. Ueda. Real-time observation of X-ray-induced intramolecular and interatomic electronic decay in CH_2I_2. Nature Communications, 10(1):2186, 2019. ISSN 2041–1723. doi: 10.1038/s41467-019-10060-z. URL https://doi.org/10.1038/s41467-019-10060-z.

[14] S. M. Vinko, O. Ciricosta, B. I. Cho, K. Engelhorn, H.-K. Chung, C. R. D. Brown, T. Burian, J. Chalupský, R. W. Falcone, C. Graves, V. Hájková, A. Higginbotham, L. Juha, J. Krzywinski, H. J. Lee, M. Messerschmidt, C. D. Murphy, Y. Ping, A. Scherz, W. Schlotter, S. Toleikis, J. J. Turner, L. Vysin, T. Wang, B. Wu, U. Zastrau, D. Zhu, R. W. Lee, P. A. Heimann, B. Nagler, and J. S. Wark. Creation and diagnosis of a solid-density plasma with an X-ray free-electron laser. Nature, 482(7383):59–62, 2012. ISSN 1476–4687. doi: 10.1038/nature10746. URL https://doi.org/10.1038/nature10746.

[15] O. Ciricosta, S. M. Vinko, H.-K. Chung, B.-I. Cho, C. R. D. Brown, T. Burian, J. Chalupský, K. Engelhorn, R. W. Falcone, C. Graves, V. Hájková, A. Higginbotham, L. Juha, J. Krzywinski, H. J. Lee, M. Messerschmidt, C. D. Murphy, Y. Ping, D. S. Rackstraw, A. Scherz, W. Schlotter, S. Toleikis, J. J. Turner, L. Vysin, T. Wang, B. Wu, U. Zastrau, D. Zhu, R. W. Lee, P. Heimann, B. Nagler, and J. S. Wark. Direct Measurements of the Ionization Potential Depression in a Dense Plasma. Phys. Rev. Lett., 109:065002, Aug 2012. doi: 10.1103/PhysRevLett.109.065002. URL https://link.aps.org/doi/10.1103/PhysRevLett.109.065002.

[16] K. Tamasaku, E. Shigemasa, Y. Inubushi, T. Katayama, K. Sawada, H. Yumoto, H. Ohashi, H. Mimura, M. Yabashi, K. Yamauchi, and T. Ishikawa. X-ray two-photon absorption competing against single and sequential multiphoton processes. Nature Photonics, 8:313–316, Feb 2014. URL https://doi.org/10.1038/nphoton.2014.10.

[17] J. Feldhaus, J. Arthur, and J. B. Hastings. X-ray free-electron lasers. Journal of Physics B: Atomic, Molecular and Optical Physics, 38(9):S799–S819, apr 2005. doi: 10.1088/0953-4075/38/9/023. URL https://doi.org/10.1088%2F0953-4075%2F38%2F9%2F023.

[18] J. R. Schneider. FLASH—from accelerator test facility to the first single-pass soft x-ray free-electron laser. Journal of Physics B: Atomic, Molecular and Optical Physics, 43(19):

194001, sep 2010. doi: 10.1088/0953-4075/43/19/194001. URL https://doi.org/10.1088%2F0953-4075%2F43%2F19%2F194001.

[19] P. Emma, R. Akre, J. Arthur, R. Bionta, C. Bostedt, J. Bozek, A. Brachmann, P. Bucksbaum, R. Coffee, F.-J. Decker, Y. Ding, D. Dowell, S. Edstrom, A. Fisher, J. Frisch, S. Gilevich, J. Hastings, G. Hays, P. Hering, Z. Huang, R. Iverson, H. Loos, M. Messerschmidt, A. Miahnahri, S. Moeller, H.-D. Nuhn, G. Pile, D. Ratner, J. Rzepiela, D. Schultz, T. Smith, P. Stefan, H. Tompkins, J. Turner, J. Welch, W. White, J. Wu, G. Yocky, and J. Galayda. First lasing and operation of an ångstrom-wavelength free-electron laser. Nature Photonics, 4(9):641–647, 2010. ISSN 1749–4893. doi: 10.1038/nphoton.2010.176. URL https://doi.org/10.1038/nphoton.2010.176.

[20] R. Neutze, R. Wouts, D. van der Spoel, E. Weckert, and J. Hajdu. Potential for biomolecular imaging with femtosecond X-ray pulses. Nature, 406(6797):752–757, 2000. ISSN 1476–4687. doi: 10.1038/35021099. URL https://doi.org/10.1038/35021099.

[21] H. N. Chapman, P. Fromme, A. Barty, T. A. White, R. A. Kirian, a. Aquila, M. S. Hunter, J. Schulz, D. P. DePonte, U. Weierstall, R. B. Doak, F. R. N. C. Maia, a. V. Martin, I. Schlichting, L. Lomb, N. Coppola, R. L. Shoeman, S. W. Epp, R. Hartmann, D. Rolles, A. Rudenko, L. Foucar, N. Kimmel, G. Weidenspointner, P. Holl, M. Liang, M. Barthelmess, C. Caleman, S. Boutet, M. J. Bogan, J. Krzywinski, C. Bostedt, S. Bajt, L. Gumprecht, B. Rudek, B. Erk, C. Schmidt, a. Hömke, C. Reich, D. Pietschner, L. Strüder, G. Hauser, H. Gorke, J. Ullrich, S. Herrmann, G. Schaller, F. Schopper, H. Soltau, K.-U. Kühnel, M. Messerschmidt, J. D. Bozek, S. P. Hau-Riege, M. Frank, C. Y. Hampton, R. G. Sierra, D. Starodub, G. J. Williams, J. Hajdu, N. Timneanu, M. M. Seibert, J. andreasson, a. Rocker, O. Jönsson, M. Svenda, S. Stern, K. Nass, R. andritschke, C.-D. Schröter, F. Krasniqi, M. Bott, K. E. Schmidt, X. Wang, I. Grotjohann, J. M. Holton, T. R. M. Barends, R. Neutze, S. Marchesini, R. Fromme, S. Schorb, D. Rupp, M. Adolph, T. Gorkhover, I. andersson, H. Hirsemann, G. Potdevin, H. Graafsma, B. Nilsson, and J. C. H. Spence. Femtosecond X-ray protein nanocrystallography. Nature, 470(7332):73–77, 2011. ISSN 1476–4687. doi: 10.1038/nature09750. URL https://doi.org/10.1038/nature09750.

[22] M. M. Seibert, T. Ekeberg, F. R. N. C. Maia, M. Svenda, J. andreasson, O. Jönsson, D. Odic, B. Iwan, a. Rocker, D. Westphal, M. Hantke, D. P. DePonte, A. Barty, J. Schulz, L. Gumprecht, N. Coppola, a. Aquila, M. Liang, T. A. White, a. Martin, C. Caleman, S. Stern, C. Abergel, V. Seltzer, J.-M. Claverie, C. Bostedt, J. D. Bozek, S. Boutet, A. A. Miahnahri, M. Messerschmidt, J. Krzywinski, G. Williams, K. O. Hodgson, M. J. Bogan, C. Y. Hampton, R. G. Sierra, D. Starodub, I. andersson, S. Bajt, M. Barthelmess, J. C. H. Spence, P. Fromme, U. Weierstall, R. Kirian, M. Hunter, R. B. Doak, S. Marchesini, S. P. Hau-Riege, M. Frank, R. L. Shoeman, L. Lomb, S. W. Epp, R. Hartmann, D. Rolles, A. Rudenko, C. Schmidt, L. Foucar, N. Kimmel, P. Holl, B. Rudek, B. Erk, A. Hömke, C. Reich, D. Pietschner, G. Weidenspointner, L. Strüder, G. Hauser, H. Gorke, J. Ullrich, I. Schlichting, S. Herrmann,

G. Schaller, F. Schopper, H. Soltau, K.-U. Kühnel, R. andritschke, C.-D. Schröter, F. Krasniqi, M. Bott, S. Schorb, D. Rupp, M. Adolph, T. Gorkhover, H. Hirsemann, G. Potdevin, H. Graafsma, B. Nilsson, H. N. Chapman, and J. Hajdu. Single mimivirus particles intercepted and imaged with an X-ray laser. Nature, 470(7332):78–81, 2011. ISSN 1476–4687. doi: 10.1038/nature09748. URL https://doi.org/10.1038/nature09748.

[23] S. Kassemeyer, J. Steinbrener, L. Lomb, E. Hartmann, andrew Aquila, A. Barty, andrew V. Martin, C. Y. Hampton, S. Bajt, M. Barthelmess, T. R. Barends, C. Bostedt, M. Bott, J. D. Bozek, N. Coppola, M. Cryle, D. P. DePonte, R. B. Doak, S. W. Epp, B. Erk, H. Fleckenstein, L. Foucar, H. Graafsma, L. Gumprecht, andreas Hartmann, R. Hartmann, G. Hauser, H. Hirsemann, andré Hömke, P. Holl, O. Jönsson, N. Kimmel, F. Krasniqi, M. Liang, F. R. Maia, S. Marchesini, K. Nass, C. Reich, D. Rolles, B. Rudek, A. Rudenko, C. Schmidt, J. Schulz, R. L. Shoeman, R. G. Sierra, H. Soltau, J. C. H. Spence, D. Starodub, F. Stellato, S. Stern, G. Stier, M. Svenda, G. Weidenspointner, U. Weierstall, T. A. White, C. Wunderer, M. Frank, H. N. Chapman, J. Ullrich, L. Strüder, M. J. Bogan, and I. Schlichting. Femtosecond free-electron laser x-ray diffraction data sets for algorithm development. Opt. Express, 20(4):4149–4158, Feb 2012. doi: 10.1364/OE.20.004149. URL http://www.opticsexpress.org/abstract.cfm?URI=oe-20-4-4149.

[24] T. Kimura, Y. Joti, A. Shibuya, C. Song, S. Kim, K. Tono, M. Yabashi, M. Tamakoshi, T. Moriya, T. Oshima, T. Ishikawa, Y. Bessho, and Y. Nishino. Imaging live cell in micro-liquid enclosure by X-ray laser diffraction. Nature Communications, 5(1):3052, 2014. ISSN 2041–1723. doi: 10.1038/ncomms4052. URL https://doi.org/10.1038/ncomms4052.

[25] G. van der Schot, M. Svenda, F. R. N. C. Maia, M. Hantke, D. P. DePonte, M. M. Seibert, a. Aquila, J. Schulz, R. Kirian, M. Liang, F. Stellato, B. Iwan, J. andreasson, N. Timneanu, D. Westphal, F. N. Almeida, D. Odic, D. Hasse, G. H. Carlsson, D. S. D. Larsson, A. Barty, a. V. Martin, S. Schorb, C. Bostedt, J. D. Bozek, D. Rolles, A. Rudenko, S. Epp, L. Foucar, B. Rudek, R. Hartmann, N. Kimmel, P. Holl, L. Englert, N.-T. Duane Loh, H. N. Chapman, I. andersson, J. Hajdu, and T. Ekeberg. Imaging single cells in a beam of live cyanobacteria with an X-ray laser. Nature Communications, 6(1):5704, 2015. ISSN 2041–1723. doi: 10.1038/ncomms6704. URL https://doi.org/10.1038/ncomms6704.

[26] T. Ditmire, T. Donnelly, A. M. Rubenchik, R. W. Falcone, and M. D. Perry. Interaction of intense laser pulses with atomic clusters. Phys. Rev. A, 53:3379–3402, May 1996. doi: 10.1103/PhysRevA.53.3379. URL https://link.aps.org/doi/10.1103/PhysRevA.53.3379.

[27] T. Ditmire, J. W. G. Tisch, E. Springate, M. B. Mason, N. Hay, R. A. Smith, J. Marangos, and M. H. R. Hutchinson. High-energy ions produced in explosions of superheated atomic clusters. Nature, 386(6620):54–56, 1997. ISSN 1476-4687. doi: 10.1038/386054a0. URL https://doi.org/10.1038/386054a0.

[28] H. Wabnitz, L. Bittner, A. R. B. de Castro, R. Döhrmann, P. Gürtler, T. Laarmann, W. Laasch, J. Schulz, A. Swiderski, K. von Haeften, T. Möller, B. Faatz, A. Fateev, J. Feldhaus, C. Gerth, U. Hahn, E. Saldin, E. Schneidmiller, K. Sytchev, K. Tiedtke, R. Treusch, and M. Yurkov. Multiple ionization of atom clusters by intense soft X-rays from a free-electron laser. Nature, 420(6915):482–485, 2002. ISSN 1476–4687. doi: 10.1038/nature01197. URL https://doi.org/10.1038/nature01197.

[29] M. Hoener, C. Bostedt, H. Thomas, L. Landt, E. Eremina, H. Wabnitz, T. Laarmann, R. Treusch, A. R. B. de Castro, and T. Möller. Charge recombination in soft x-ray laser produced nanoplasmas. Journal of Physics B: Atomic, Molecular and Optical Physics, 41(18): 181001, sep 2008. doi: 10.1088/0953-4075/41/18/181001. URL https://doi.org/10.1088%2F0953-4075%2F41%2F18%2F181001.

[30] C. Bostedt, H. Thomas, M. Hoener, E. Eremina, T. Fennel, K.-H. Meiwes-Broer, H. Wabnitz, M. Kuhlmann, E. Plönjes, K. Tiedtke, R. Treusch, J. Feldhaus, A. R. B. de Castro, and T. Möller. Multistep Ionization of Argon Clusters in Intense Femtosecond Extreme Ultraviolet Pulses. Phys. Rev. Lett., 100:133401, Apr 2008. doi: 10.1103/PhysRevLett.100.133401. URL https://link.aps.org/doi/10.1103/PhysRevLett.100.133401.

[31] H. Iwayama, K. Nagaya, M. Yao, H. Fukuzawa, X.-J. Liu, G. Prümper, K. Motomura, K. Ueda, N. Saito, A. Rudenko, L. Foucar, M. Nagasono, A. Higashiya, M. Yabashi, T. Ishikawa, H. Ohashi, and H. Kimura. Frustration of photoionization of Ar nanoplasma produced by extreme ultraviolet FEL pulses. Journal of Physics B: Atomic, Molecular and Optical Physics, 46(16):164019, aug 2013. doi: 10.1088/0953-4075/46/16/164019. URL https://doi.org/10.1088%2F0953-4075%2F46%2F16%2F164019.

[32] K. Nagaya, A. Sugishima, H. Iwayama, H. Murakami, M. Yao, H. Fukuzawa, X.-J. Liu, K. Motomura, K. Ueda, N. Saito, L. Foucar, A. Rudenko, M. Kurka, K.-U. Kühnel, J. Ullrich, A. Czasch, R. Dörner, R. Feifel, M. Nagasono, A. Higashiya, M. Yabashi, T. Ishikawa, T. Togashi, H. Kimura, and H. Ohashi. Unusual under-threshold ionization of neon clusters studied by ion spectroscopy. Journal of Physics B: Atomic, Molecular and Optical Physics, 46(16):164023, aug 2013. doi: 10.1088/0953-4075/46/16/164023. URL https://doi.org/10.1088%2F0953-4075%2F46%2F16%2F164023.

[33] S. Yase, K. Nagaya, Y. Mizoguchi, M. Yao, H. Fukuzawa, K. Motomura, A. Yamada, R. Ma, K. Ueda, N. Saito, M. Nagasono, T. Togashi, K. Tono, M. Yabashi, T. Ishikawa, H. Ohashi, and Y. Senba. Crossover in the photoionization processes of neon clusters with increasing EUV free-electron-laser intensity. Phys. Rev. A, 88:043203, Oct 2013. doi: 10.1103/PhysRevA.88.043203. URL https://link.aps.org/doi/10.1103/PhysRevA.88.043203.

[34] B. Schütte, M. Arbeiter, T. Fennel, M. J. J. Vrakking, and A. Rouzée. Rare-Gas Clusters in Intense Extreme-Ultraviolet Pulses from a High-Order Harmonic Source. Phys. Rev. Lett.,

112:073003, Feb 2014. doi: 10.1103/PhysRevLett.112.073003. URL https://link.aps.org/doi/10.1103/PhysRevLett.112.073003.

[35] B. Schütte, F. Campi, M. Arbeiter, T. Fennel, M. J. J. Vrakking, and A. Rouzée. Tracing Electron-Ion Recombination in Nanoplasmas Produced by Extreme-Ultraviolet Irradiation of Rare-Gas Clusters. Phys. Rev. Lett., 112:253401, Jun 2014. doi: 10.1103/PhysRevLett.112.253401. URL https://link.aps.org/doi/10.1103/PhysRevLett.112.253401.

[36] D. Iablonskyi, K. Nagaya, H. Fukuzawa, K. Motomura, Y. Kumagai, S. Mondal, T. Tachibana, T. Takanashi, T. Nishiyama, K. Matsunami, P. Johnsson, P. Piseri, G. Sansone, A. Dubrouil, M. Reduzzi, P. Carpeggiani, C. Vozzi, M. Devetta, M. Negro, F. Calegari, A. Trabattoni, M. C. Castrovilli, D. Faccialà, Y. Ovcharenko, T. Möller, M. Mudrich, F. Stienkemeier, M. Coreno, M. Alagia, B. Schütte, N. Berrah, A. I. Kuleff, G. Jabbari, C. Callegari, O. Plekan, P. Finetti, C. Spezzani, E. Ferrari, E. Allaria, G. Penco, C. Serpico, G. De Ninno, I. Nikolov, B. Diviacco, S. Di Mitri, L. Giannessi, K. C. Prince, and K. Ueda. Slow Interatomic Coulombic Decay of Multiply Excited Neon Clusters. Phys. Rev. Lett., 117:276806, Dec 2016. doi: 10.1103/PhysRevLett.117.276806. URL https://link.aps.org/doi/10.1103/PhysRevLett.117.276806.

[37] K. Nagaya, D. Iablonskyi, N. V. Golubev, K. Matsunami, H. Fukuzawa, K. Motomura, T. Nishiyama, T. Sakai, T. Tachibana, S. Mondal, S. Wada, K. C. Prince, C. Callegari, C. Miron, N. Saito, M. Yabashi, P. V. Demekhin, L. S. Cederbaum, A. I. Kuleff, M. Yao, and K. Ueda. Interatomic Coulombic decay cascades in multiply excited neon clusters. Nature Communications, 7(1):13477, 2016. ISSN 2041–1723. doi: 10.1038/ncomms13477. URL https://doi.org/10.1038/ncomms13477.

[38] Y. Kumagai, Z. Jurek, W. Xu, H. Fukuzawa, K. Motomura, D. Iablonskyi, K. Nagaya, S.-i. Wada, S. Mondal, T. Tachibana, Y. Ito, T. Sakai, K. Matsunami, T. Nishiyama, T. Umemoto, C. Nicolas, C. Miron, T. Togashi, K. Ogawa, S. Owada, K. Tono, M. Yabashi, S.-K. Son, B. Ziaja, R. Santra, and K. Ueda. Radiation-Induced Chemical Dynamics in Ar Clusters Exposed to Strong X-Ray Pulses. Phys. Rev. Lett., 120:223201, May 2018. doi: 10.1103/PhysRevLett.120.223201. URL https://link.aps.org/doi/10.1103/PhysRevLett.120.223201.

[39] Y. Kumagai, H. Fukuzawa, K. Motomura, D. Iablonskyi, K. Nagaya, S.-i. Wada, Y. Ito, T. Takanashi, Y. Sakakibara, D. You, T. Nishiyama, K. Asa, Y. Sato, T. Umemoto, K. Kariyazono, E. Kukk, K. Kooser, C. Nicolas, C. Miron, T. Asavei, L. Neagu, M. S. Schöffler, G. Kastirke, X.-j. Liu, S. Owada, T. Katayama, T. Togashi, K. Tono, M. Yabashi, N. V. Golubev, K. Gokhberg, L. S. Cederbaum, A. I. Kuleff, and K. Ueda. Following the Birth of a Nanoplasma Produced by an Ultrashort Hard-X-Ray Laser in Xenon Clusters. Phys. Rev. X, 8:031034, Aug 2018. doi: 10.1103/PhysRevX.8.031034. URL https://link.aps.org/doi/10.1103/PhysRevX.8.031034.

[40] A. Niozu, N. Yokono, T. Nishiyama, H. Fukuzawa, T. Sakurazawa, K. Matsuda, T. Takanashi, D. You, Y. Li, T. Ono, T. Gaumnitz, M. Schöffler, S. Grundmann, S.-i. Wada, P. Carpeggiani, W. Q. Xu, X. J. Liu, S. Owada, K. Tono, T. Togashi, M. Yabashi, N. V. Kryzhevoi, K. Gokhberg, A. I. Kuleff, L. S. Cederbaum, K. Ueda, and K. Nagaya. Electron spectroscopic study of nanoplasma formation triggered by intense soft x-ray pulses. The Journal of Chemical Physics, 151(18):184305, 2019. doi: 10.1063/1.5115053. URL https://doi.org/10.1063/1.5115053.

[41] L. Schroedter, M. Müller, A. Kickermann, A. Przystawik, S. Toleikis, M. Adolph, L. Flückiger, T. Gorkhover, L. Nösel, M. Krikunova, T. Oelze, Y. Ovcharenko, D. Rupp, M. Sauppe, D. Wolter, S. Schorb, C. Bostedt, T. Möller, and T. Laarmann. Hidden Charge States in Soft-X-Ray Laser-Produced Nanoplasmas Revealed by Fluorescence Spectroscopy. Phys. Rev. Lett., 112:183401, May 2014. doi: 10.1103/PhysRevLett.112.183401. URL https://link.aps.org/doi/10.1103/PhysRevLett.112.183401.

[42] H. Iwayama, J. R. Harries, and E. Shigemasa. Transient charge dynamics in argon-cluster nanoplasmas created by intense extreme-ultraviolet free-electron-laser irradiation. Phys. Rev. A, 91:021402, Feb 2015. doi: 10.1103/PhysRevA.91.021402. URL https://link.aps.org/doi/10.1103/PhysRevA.91.021402.

[43] C. Bostedt, M. Adolph, E. Eremina, M. Hoener, D. Rupp, S. Schorb, H. Thomas, A. R. B. de Castro, and T. Möller. Clusters in intense FLASH pulses: ultrafast ionization dynamics and electron emission studied with spectroscopic and scattering techniques. Journal of Physics B: Atomic, Molecular and Optical Physics, 43(19):194011, sep 2010. doi: 10.1088/0953-4075/43/19/194011. URL https://doi.org/10.1088%2F0953-4075%2F43%2F19%2F194011.

[44] C. Bostedt, E. Eremina, D. Rupp, M. Adolph, H. Thomas, M. Hoener, A. R. B. de Castro, J. Tiggesbäumker, K.-H. Meiwes-Broer, T. Laarmann, H. Wabnitz, E. Plönjes, R. Treusch, J. R. Schneider, and T. Möller. Ultrafast X-Ray Scattering of Xenon Nanoparticles: Imaging Transient States of Matter. Phys. Rev. Lett., 108:093401, Feb 2012. doi: 10.1103/PhysRevLett.108.093401. URL https://link.aps.org/doi/10.1103/PhysRevLett.108.093401.

[45] D. Rupp, M. Adolph, T. Gorkhover, S. Schorb, D. Wolter, R. Hartmann, N. Kimmel, C. Reich, T. Feigl, A. R. B. de Castro, R. Treusch, L. Strüder, T. Möller, and C. Bostedt. Identification of twinned gas phase clusters by single-shot scattering with intense soft x-ray pulses. New Journal of Physics, 14(5):055016, may 2012. doi: 10.1088/1367-2630/14/5/055016. URL https://doi.org/10.1088%2F1367-2630%2F14%2F5%2F055016.

[46] T. Gorkhover, M. Adolph, D. Rupp, S. Schorb, S. W. Epp, B. Erk, L. Foucar, R. Hartmann, N. Kimmel, K.-U. Kühnel, D. Rolles, B. Rudek, A. Rudenko, R. andritschke, A. Aquila, J. D. Bozek, N. Coppola, T. Erke, F. Filsinger, H. Gorke, H. Graafsma, L. Gumprecht, G. Hauser, S. Herrmann, H. Hirsemann, A. Hömke, P. Holl, C. Kaiser, F. Krasniqi, J.-H.

Meyer, M. Matysek, M. Messerschmidt, D. Miessner, B. Nilsson, D. Pietschner, G. Potdevin, C. Reich, G. Schaller, C. Schmidt, F. Schopper, C. D. Schröter, J. Schulz, H. Soltau, G. Weidenspointner, I. Schlichting, L. Strüder, J. Ullrich, T. Möller, and C. Bostedt. Nanoplasma Dynamics of Single Large Xenon Clusters Irradiated with Superintense X-Ray Pulses from the Linac Coherent Light Source Free-Electron Laser. Phys. Rev. Lett., 108:245005, Jun 2012. doi: 10.1103/PhysRevLett.108.245005. URL https://link.aps.org/doi/10.1103/PhysRevLett.108.245005.

[47] D. Rupp, M. Adolph, L. Flückiger, T. Gorkhover, J. P. Müller, M. Müller, M. Sauppe, D. Wolter, S. Schorb, R. Treusch, C. Bostedt, and T. Möller. Generation and structure of extremely large clusters in pulsed jets. The Journal of Chemical Physics, 141(4):044306, 2014. doi: 10.1063/1.4890323. URL https://doi.org/10.1063/1.4890323.

[48] T. Gorkhover, S. Schorb, R. Coffee, M. Adolph, L. Foucar, D. Rupp, a. Aquila, J. D. Bozek, S. W. Epp, B. Erk, L. Gumprecht, L. Holmegaard, a. Hartmann, R. Hartmann, G. Hauser, P. Holl, a. Hömke, P. Johnsson, N. Kimmel, K.-U. Kühnel, M. Messerschmidt, C. Reich, A. Rouzée, B. Rudek, C. Schmidt, J. Schulz, H. Soltau, S. Stern, G. Weidenspointner, B. White, J. Küpper, L. Strüder, I. Schlichting, J. Ullrich, D. Rolles, A. Rudenko, T. Möller, and C. Bostedt. Femtosecond and nanometre visualization of structural dynamics in superheated nanoparticles. Nature Photonics, 10:93, Jan 2016. URL https://doi.org/10.1038/nphoton.2015.264.

[49] D. Rupp, L. Flückiger, M. Adolph, T. Gorkhover, M. Krikunova, J. P. Müller, M. Müller, T. Oelze, Y. Ovcharenko, B. Röben, M. Sauppe, S. Schorb, D. Wolter, R. Mitzner, M. Wöstmann, S. Roling, M. Harmand, R. Treusch, M. Arbeiter, T. Fennel, C. Bostedt, and T. Möller. Recombination-Enhanced Surface Expansion of Clusters in Intense Soft X-Ray Laser Pulses. Phys. Rev. Lett., 117:153401, Oct 2016. doi: 10.1103/PhysRevLett.117.153401. URL https://link.aps.org/doi/10.1103/PhysRevLett.117.153401.

[50] B. Langbehn, K. Sander, Y. Ovcharenko, C. Peltz, a. Clark, M. Coreno, R. Cucini, M. Drabbels, P. Finetti, M. Di Fraia, L. Giannessi, C. Grazioli, D. Iablonskyi, A. C. LaForge, T. Nishiyama, V. Oliver Álvarez de Lara, P. Piseri, O. Plekan, K. Ueda, J. Zimmermann, K. C. Prince, F. Stienkemeier, C. Callegari, T. Fennel, D. Rupp, and T. Möller. Three-Dimensional Shapes of Spinning Helium Nanodroplets. Phys. Rev. Lett., 121:255301, Dec 2018. doi: 10.1103/PhysRevLett.121.255301. URL https://link.aps.org/doi/10.1103/PhysRevLett.121.255301.

[51] U. Saalmann and J.-M. Rost. Ionization of Clusters in Intense Laser Pulses through Collective Electron Dynamics. Phys. Rev. Lett., 91:223401, Nov 2003. doi: 10.1103/PhysRevLett.91.223401. URL https://link.aps.org/doi/10.1103/PhysRevLett.91.223401.

[52] C. Siedschlag and J.-M. Rost. Small Rare-Gas Clusters in Soft X-Ray Pulses. Phys. Rev.

Lett., 93:043402, Jul 2004. doi: 10.1103/PhysRevLett.93.043402. URL https://link.aps.org/doi/10.1103/PhysRevLett.93.043402.

[53] U. Saalmann, C. Siedschlag, and J. M. Rost. Mechanisms of cluster ionization in strong laser pulses. Journal of Physics B: Atomic, Molecular and Optical Physics, 39(4):R39–R77, jan 2006. doi: 10.1088/0953-4075/39/4/r01. URL https://doi.org/10.1088%2F0953-4075%2F39%2F4%2Fr01.

[54] M. Arbeiter and T. Fennel. Rare-gas clusters in intense VUV, XUV and soft x-ray pulses: signatures of the transition from nanoplasma-driven cluster expansion to coulomb explosion in ion and electron spectra. New Journal of Physics, 13(5):053022, may 2011. doi: 10.1088/1367-2630/13/5/053022. URL https://doi.org/10.1088%2F1367-2630%2F13%2F5%2F053022. CC BY-NC-SA 3.0.

[55] C. Peltz, C. Varin, T. Brabec, and T. Fennel. Time-Resolved X-Ray Imaging of Anisotropic Nanoplasma Expansion. Phys. Rev. Lett., 113:133401, Sep 2014. doi: 10.1103/PhysRevLett.113.133401. URL https://link.aps.org/doi/10.1103/PhysRevLett.113.133401.

[56] J. Zimmermann, B. Langbehn, R. Cucini, M. Di Fraia, P. Finetti, A. C. LaForge, T. Nishiyama, Y. Ovcharenko, P. Piseri, O. Plekan, K. C. Prince, F. Stienkemeier, K. Ueda, C. Callegari, T. Möller, and D. Rupp. Deep neural networks for classifying complex features in diffraction images. Phys. Rev. E, 99:063309, Jun 2019. doi: 10.1103/PhysRevE.99.063309. URL https://link.aps.org/doi/10.1103/PhysRevE.99.063309.

[57] M. R. Islam, U. Saalmann, and J. M. Rost. Kinetic energy of ions after Coulomb explosion of clusters induced by an intense laser pulse. Phys. Rev. A, 73:041201, Apr 2006. doi: 10.1103/PhysRevA.73.041201. URL https://link.aps.org/doi/10.1103/PhysRevA.73.041201.

[58] H. Thomas, C. Bostedt, M. Hoener, E. Eremina, H. Wabnitz, T. Laarmann, E. Plönjes, R. Treusch, A. R. B. de Castro, and T. Möller. Shell explosion and core expansion of xenon clusters irradiated with intense femtosecond soft x-ray pulses. Journal of Physics B: Atomic, Molecular and Optical Physics, 42(13):134018, jun 2009. doi: 10.1088/0953-4075/42/13/134018. URL https://doi.org/10.1088%2F0953-4075%2F42%2F13%2F134018.

[59] I. Barke, H. Hartmann, D. Rupp, L. Flückiger, M. Sauppe, M. Adolph, S. Schorb, C. Bostedt, R. Treusch, C. Peltz, S. Bartling, T. Fennel, K.-H. Meiwes-Broer, and T. Möller. The 3D-architecture of individual free silver nanoparticles captured by X-ray scattering. Nature Communications, 6(1):6187, 2015. ISSN 2041–1723. doi: 10.1038/ncomms7187. URL https://doi.org/10.1038/ncomms7187.

[60] S. P. Hau-Riege and H. N. Chapman. Modeling of the damage dynamics of nanospheres exposed to x-ray free-electron-laser radiation. Phys. Rev. E, 77:041902, Apr 2008. doi: 10.1103/PhysRevE.77.041902. URL https://link.aps.org/doi/10.1103/PhysRevE.77.041902.

[61] K. R. Ferguson, M. Bucher, T. Gorkhover, S. Boutet, H. Fukuzawa, J. E. Koglin, Y. Kumagai, A. Lutman, A. Marinelli, M. Messerschmidt, K. Nagaya, J. Turner, K. Ueda, G. J. Williams, P. H. Bucksbaum, and C. Bostedt. Transient lattice contraction in the solid-to-plasma transition. Science Advances, 2(1):e1500837, 2016. doi: 10.1126/sciadv.1500837. URL https://advances.sciencemag.org/content/2/1/e1500837. CC BY-NC 4.0.

[62] K. R. Ferguson. Crystal structure determinations of xenon nanoparticles and x-ray induced transient lattice contraction in the solid-to-plasma transition. PhD thesis, Stanford University, Feb. 2016. URL https://purl.stanford.edu/qk328xg1417. CC BY-NC 3.0.

[63] A. Thompson, I. Lindau, D. Attwood, Y. Liu, E. Gullikson, P. Pianetta, M. Howells, A. Robinson, K.-J. Kim, J. Scofield, J. Kirz, J. Underwood, J. Kortright, G. Williams, and H. Winick. X-ray data booklet. Lawrence Berkeley National Laboratory, 2009.

[64] C. Bohren and D. Huffman. Absorption and Scattering of Light by Small Particles. John Wiley, 1983.

[65] J. Als-Nielsen and D. McMorrow. Elements of Modern X-ray Physics. John Wiley & Sons, 2nd edition, 2011.

[66] W. Veigele. Photon cross sections from 0.1 keV to 1 MeV for elements Z = 1 to Z = 94. Atomic Data and Nuclear Data Tables, 5(1):51–111, 1973. ISSN 0092–640X. doi: https://doi.org/10.1016/S0092-640X(73)80015-4. URL http://www.sciencedirect.com/science/article/pii/S0092640X73800154.

[67] J. H. Hubbell, H. A. Gimm, and I. Øverbø. Pair, Triplet, and Total Atomic Cross Sections (and Mass Attenuation Coefficients) for 1 MeV-100 GeV Photons in Elements Z=1 to 100. Journal of Physical and Chemical Reference Data, 9(4):1023–1148, 1980. doi: 10.1063/1.555629. URL https://doi.org/10.1063/1.555629.

[68] B. Henke, E. Gullikson, and J. Davis. X-Ray Interactions: Photoabsorption, Scattering, Transmission, and Reflection at E = 50-30,000 eV, Z = 1-92. Atomic Data and Nuclear Data Tables, 54(2):181–342, 1993. ISSN 0092-640X. doi: https://doi.org/10.1006/adnd.1993.1013. URL http://www.sciencedirect.com/science/article/pii/S0092640X83710132.

[69] M. O. Krause. Atomic radiative and radiationless yields for K and L shells. Journal of Physical and Chemical Reference Data, 8(2):307–327, 1979. doi: 10.1063/1.555594. URL https://doi.org/10.1063/1.555594.

[70] T. Fennel, K.-H. Meiwes-Broer, J. Tiggesbäumker, P.-G. Reinhard, P. M. Dinh, and E. Suraud. Laser-driven nonlinear cluster dynamics. Rev. Mod. Phys., 82:1793–1842, Jun 2010. doi: 10.1103/RevModPhys.82.1793. URL https://link.aps.org/doi/10.1103/RevModPhys.82.1793.

[71] L. V. Keldysh. Ionization in the field of a strong electromagnetic wave. Soviet Physics JETP, 20(5):1307–1314, 1965. URL http://jetp.ac.ru/cgi-bin/dn/e_020_05_1307.pdf.

[72] U. Saalmann and J.-M. Rost. Ionization of Clusters in Strong X-Ray Laser Pulses. Phys. Rev. Lett., 89:143401, Sep 2002. doi: 10.1103/PhysRevLett.89.143401. URL https://link.aps.org/doi/10.1103/PhysRevLett.89.143401.

[73] V. Krainov and M. Smirnov. Cluster beams in the super-intense femtosecond laser pulse. Physics Reports, 370(3):237–331, 2002. ISSN 0370-1573. doi: https://doi.org/10.1016/S0370-1573(02)00272-7. URL http://www.sciencedirect.com/science/article/pii/S0370157302002727.

[74] A. Guinier. X-Ray Diffraction in Crystals, Imperfect Crystals, and Amorphous Bodies. Dover Publications, 1994. ISBN 0486680118.

[75] A. L. Patterson. The Scherrer Formula for X-Ray Particle Size Determination. Phys. Rev., 56:978–982, Nov 1939. doi: 10.1103/PhysRev.56.978. URL https://link.aps.org/doi/10.1103/PhysRev.56.978.

[76] J. I. Langford and A. J. C. Wilson. Scherrer after sixty years: A survey and some new results in the determination of crystallite size. Journal of Applied Crystallography, 11(2):102–113, apr 1978. doi: 10.1107/s0021889878012844. URL https://doi.org/10.1107%2Fs0021889878012844.

[77] Definitions of Solar Irradiance Spectral Categories. URL http://www.spacewx.com/pdf/SET_21348_2004.pdf. accessed on October 29th, 2019.

[78] M. Lezius, S. Dobosz, D. Normand, and M. Schmidt. Explosion Dynamics of Rare Gas Clusters in Strong Laser Fields. Phys. Rev. Lett., 80:261–264, Jan 1998. doi: 10.1103/PhysRevLett.80.261. URL https://link.aps.org/doi/10.1103/PhysRevLett.80.261.

[79] S. P. Hau-Riege, R. A. London, and A. Szoke. Dynamics of biological molecules irradiated by short x-ray pulses. Phys. Rev. E, 69:051906, May 2004. doi: 10.1103/PhysRevE.69.051906. URL https://link.aps.org/doi/10.1103/PhysRevE.69.051906.

[80] H. M. Quiney and K. A. Nugent. Biomolecular imaging and electronic damage using X-ray free-electron lasers. Nature Physics, 7(2):142–146, 2011. ISSN 1745–2481. doi: 10.1038/nphys1859. URL https://doi.org/10.1038/nphys1859.

[81] E. K. Curwood, H. M. Quiney, and K. A. Nugent. Determining electronic damage to biomolecular structures in x-ray free-electron-laser imaging experiments. Phys. Rev. A, 87:053407, May 2013. doi: 10.1103/PhysRevA.87.053407. URL https://link.aps.org/doi/10.1103/PhysRevA.87.053407.

[82] M. J. Bucher. Ultrafast Dynamics of Nanoparticles in Highly Intense X-Ray Pulses. PhD thesis, Technische Universität Berlin, Dec. 2017. URL http://dx.doi.org/10.14279/depositonce-6598. CC BY 4.0.

[83] J. Blau, K. Cohn, W. B. Colson, and R. Vigil. Free electron lasers in 2013. Proceedings of FEL2013, pages 486–490, 2013. URL https://accelconf.web.cern.ch/accelconf/FEL2013/papers/wepso01.pdf.

[84] L. R. Elias, W. M. Fairbank, J. M. J. Madey, H. A. Schwettman, and T. I. Smith. Observation of Stimulated Emission of Radiation by Relativistic Electrons in a Spatially Periodic Transverse Magnetic Field. Phys. Rev. Lett., 36:717–720, Mar 1976. doi: 10.1103/PhysRevLett.36.717. URL https://link.aps.org/doi/10.1103/PhysRevLett.36.717.

[85] Z. Huang. Brightness and Coherence of Synchrotron Radiation and FELs. In Proceedings, 4th International Particle Accelerator Conference (IPAC 2013): Shanghai, China, May 12-17, 2013, page MOYCB101, 2013. URL http://JACoW.org/IPAC2013/papers/moycb101.pdf. CC BY 3.0.

[86] K. Zhukovsky. Undulators for Short Pulse X-Ray Self-Amplified Spontaneous Emission-Free Electron Lasers. In R. Viskup, editor, High Energy and Short Pulse Lasers, chapter 8. InteChOpen, Rijeka, 2016. doi: 10.5772/64439. URL https://doi.org/10.5772/64439. CC BY 3.0.

[87] E. Saldin, E. V. Schneidmiller, and M. V. Yurkov. The Physics of Free Electron Lasers. Springer-Verlag Berlin Heidelberg, 2000.

[88] K.-J. Kim. Angular distribution of undulator power for an arbitrary deflection parameter K. Nuclear Instruments and Methods in Physics Research Section A: Accelerators, Spectrometers, Detectors and Associated Equipment, 246(1):67–70, 1986. ISSN 0168–9002. doi: https://doi.org/10.1016/0168-9002(86)90047-1. URL http://www.sciencedirect.com/science/article/pii/0168900286900471.

[89] Z. Huang and K.-J. Kim. Review of x-ray free-electron laser theory. Phys. Rev. ST Accel. Beams, 10:034801, Mar 2007. doi: 10.1103/PhysRevSTAB.10.034801. URL https://link.aps.org/doi/10.1103/PhysRevSTAB.10.034801. CC BY 3.0.

[90] T. Ishikawa, H. Aoyagi, T. Asaka, Y. Asano, N. Azumi, T. Bizen, H. Ego, K. Fukami, T. Fukui, Y. Furukawa, S. Goto, H. Hanaki, T. Hara, T. Hasegawa, T. Hatsui, A. Higashiya, T. Hirono, N. Hosoda, M. Ishii, T. Inagaki, Y. Inubushi, T. Itoga, Y. Joti, M. Kago, T. Kameshima, H. Kimura, Y. Kirihara, A. Kiyomichi, T. Kobayashi, C. Kondo, T. Kudo, H. Maesaka, X. M. Maréchal, T. Masuda, S. Matsubara, T. Matsumoto, T. Matsushita, S. Matsui, M. Nagasono, N. Nariyama, H. Ohashi, T. Ohata, T. Ohshima, S. Ono, Y. Otake, C. Saji, T. Sakurai, T. Sato, K. Sawada, T. Seike, K. Shirasawa, T. Sugimoto, S. Suzuki, S. Takahashi, H. Takebe, K. Takeshita, K. Tamasaku, H. Tanaka, R. Tanaka, T. Tanaka,

T. Togashi, K. Togawa, A. Tokuhisa, H. Tomizawa, K. Tono, S. Wu, M. Yabashi, M. Yamaga, A. Yamashita, K. Yanagida, C. Zhang, T. Shintake, H. Kitamura, and N. Kumagai. A compact X-ray free-electron laser emitting in the sub-ångström region. Nature Photonics, 6(8):540–544, 2012. ISSN 1749-4893. doi: 10.1038/nphoton.2012.141. URL https://doi.org/10.1038/nphoton.2012.141.

[91] K. Togawa, T. Shintake, T. Inagaki, K. Onoe, T. Tanaka, H. Baba, and H. Matsumoto. CeB_6 electron gun for low-emittance injector. Phys. Rev. ST Accel. Beams, 10:020703, Feb 2007. doi: 10.1103/PhysRevSTAB.10.020703. URL https://link.aps.org/doi/10.1103/PhysRevSTAB.10.020703.

[92] K. Tono, T. Hara, M. Yabashi, and H. Tanaka. Multiple-beamline operation of SACLA. Journal of Synchrotron Radiation, 26(2):595–602, Mar 2019. doi: 10.1107/S1600577519001607. URL https://doi.org/10.1107/S1600577519001607. CC BY 3.0.

[93] T. Hara, Y. Inubushi, T. Katayama, T. Sato, H. Tanaka, T. Tanaka, T. Togashi, K. Togawa, K. Tono, M. Yabashi, and T. Ishikawa. Two-colour hard X-ray free-electron laser with wide tunability. Nature Communications, 4(1):2919, 2013. ISSN 2041–1723. doi: 10.1038/ncomms3919. URL https://doi.org/10.1038/ncomms3919.

[94] I. Inoue, T. Osaka, T. Hara, T. Tanaka, T. Inagaki, T. Fukui, S. Goto, Y. Inubushi, H. Kimura, R. Kinjo, H. Ohashi, K. Togawa, K. Tono, M. Yamaga, H. Tanaka, T. Ishikawa, and M. Yabashi. Generation of narrow-band X-ray free-electron laser via reflection self-seeding. Nature Photonics, 13(5):319–322, 2019. ISSN 1749–4893. doi: 10.1038/s41566-019-0365-y. URL https://doi.org/10.1038/s41566-019-0365-y.

[95] T. Katayama, S. Owada, T. Togashi, K. Ogawa, P. Karvinen, I. Vartiainen, A. Eronen, C. David, T. Sato, K. Nakajima, Y. Joti, H. Yumoto, H. Ohashi, and M. Yabashi. A beam branching method for timing and spectral characterization of hard X-ray free-electron lasers. Structural Dynamics, 3(3):034301, 2016. doi: 10.1063/1.4939655. URL https://doi.org/10.1063/1.4939655.

[96] K. Tamasaku, Y. Inubushi, I. Inoue, K. Tono, M. Yabashi, and T. Ishikawa. Inline spectrometer for shot-by-shot determination of pulse energies of a two-color X-ray free-electron laser. Journal of synchrotron radiation, 23(1):331–333, Jan 2016. ISSN 1600–5775. doi: 10.1107/S1600577515020196. URL https://www.ncbi.nlm.nih.gov/pubmed/26698081.

[97] K. Tono, T. Togashi, Y. Inubushi, T. Sato, T. Katayama, K. Ogawa, H. Ohashi, H. Kimura, S. Takahashi, K. Takeshita, H. Tomizawa, S. Goto, T. Ishikawa, and M. Yabashi. Beamline, experimental stations and photon beam diagnostics for the hard x-ray free electron laser of SACLA. New Journal of Physics, 15(8):083035, aug 2013. doi: 10.1088/1367-2630/15/8/083035. URL https://doi.org/10.1088%2F1367-2630%2F15%2F8%2F083035. CC BY 3.0.

[98] T. Katayama, T. Hirano, Y. Morioka, Y. Sano, T. Osaka, S. Owada, T. Togashi, and M. Yabashi. X-ray optics for advanced ultrafast pump–probe X-ray experiments at SACLA. Journal of Synchrotron Radiation, 26(2):333–338, Mar 2019. doi: 10.1107/S1600577518018362. URL https://doi.org/10.1107/S1600577518018362. CC BY 4.0.

[99] P. Kirkpatrick and A. V. Baez. Formation of Optical Images by X-Rays. J. Opt. Soc. Am., 38(9):766–774, Sep 1948. doi: 10.1364/JOSA.38.000766. URL http://www.osapublishing.org/abstract.cfm?URI=josa-38-9-766.

[100] H. Yumoto, H. Mimura, T. Koyama, S. Matsuyama, K. Tono, T. Togashi, Y. Inubushi, T. Sato, T. Tanaka, T. Kimura, H. Yokoyama, J. Kim, Y. Sano, Y. Hachisu, M. Yabashi, H. Ohashi, H. Ohmori, T. Ishikawa, and K. Yamauchi. Focusing of X-ray free-electron laser pulses with reflective optics. Nature Photonics, 7:43–47, 2013. URL https://doi.org/10.1038/nphoton.2012.306.

[101] H. Haberland. Clusters of Atoms and Molecules, volume 52. Springer-Verlag Berlin Heidelberg, 1994.

[102] H. Pauly. Fundamental Principles of Gas Dynamics. In: Atom, Molecule, and Cluster Beams I, volume 28. Springer, Berlin, Heidelberg, 2000. doi: https://doi.org/10.1007/978-3-662-04213-7_3.

[103] E. Wilhelm and R. Battino. Estimation of Lennard-Jones (6,12) Pair Potential Parameters from Gas Solubility Data. The Journal of Chemical Physics, 55(8):4012–4017, 1971. doi: 10.1063/1.1676694. URL https://doi.org/10.1063/1.1676694.

[104] W. Miehle, O. Kandler, T. Leisner, and O. Echt. Mass spectrometric evidence for icosahedral structure in large rare gas clusters: Ar, Kr, Xe. The Journal of Chemical Physics, 91(10):5940–5952, 1989. doi: 10.1063/1.457464. URL https://doi.org/10.1063/1.457464.

[105] B. W. van de Waal. Icosahedral, decahedral, fcc, and defect-fcc structural models for ArN clusters, N≥500: How plausible are they? The Journal of Chemical Physics, 98(6):4909–4919, 1993. doi: 10.1063/1.464946. URL https://doi.org/10.1063/1.464946.

[106] N. V. Krainyukova. 'the crystal structure problem' in noble gas nanoclusters. Thin Solid Films, 515(4):1658–1663, 2006. ISSN 0040–6090. doi: https://doi.org/10.1016/j.tsf.2006.05.041. URL http://www.sciencedirect.com/science/article/pii/S0040609006006857.

[107] D. Lippmann, W. C. Schieve, and C. Canestaro. Clustering time dependence in molecular dynamics: A kinetic model. The Journal of Chemical Physics, 81(11):4969–4974, 1984. doi: 10.1063/1.447481. URL https://doi.org/10.1063/1.447481.

[108] O. F. Hagena. Cluster ion sources (invited). Review of Scientific Instruments, 63(4):2374–2379, 1992. doi: 10.1063/1.1142933. URL https://doi.org/10.1063/1.1142933.

[109] O. F. Hagena and W. Obert. Cluster Formation in Expanding Supersonic Jets: Effect of Pressure, Temperature, Nozzle Size, and Test Gas. The Journal of Chemical Physics, 56(5): 1793–1802, 1972. doi: 10.1063/1.1677455. URL https://doi.org/10.1063/1.1677455.

[110] O. F. Hagena. Nucleation and growth of clusters in expanding nozzle flows. Surface Science, 106(1):101–116, 1981. ISSN 0039–6028. doi: https://doi.org/10.1016/0039-6028(81)90187-4. URL http://www.sciencedirect.com/science/article/pii/0039602881901874.

[111] O. F. Hagena. Condensation in free jets: Comparison of rare gases and metals. Zeitschrift für Physik D Atoms, Molecules and Clusters, 4:291–299, 1987. ISSN 1431–5866. doi: doi.org/10.1007/BF01436638. URL https://doi.org/10.1007/BF01436638.

[112] F. Dorchies, F. Blasco, T. Caillaud, J. Stevefelt, C. Stenz, A. S. Boldarev, and V. A. Gasilov. Spatial distribution of cluster size and density in supersonic jets as targets for intense laser pulses. Phys. Rev. A, 68:023201, Aug 2003. doi: 10.1103/PhysRevA.68.023201. URL https://link.aps.org/doi/10.1103/PhysRevA.68.023201.

[113] U. Buck and R. Krohne. Cluster size determination from diffractive He atom scattering. The Journal of Chemical Physics, 105(13):5408–5415, 1996. doi: 10.1063/1.472406. URL https://doi.org/10.1063/1.472406.

[114] a. M. Bush, a. J. Bell, J. G. Frey, and J.-M. Mestdagh. Rayleigh Scattering of Laser and Synchrotron Radiation from Pulsed Free Jets of Ar_n and $(N_2O)_n$ Clusters. The Journal of Physical Chemistry A, 102(32):6457–6463, 1998. doi: 10.1021/jp9814810. URL https://doi.org/10.1021/jp9814810.

[115] R. Karnbach, M. Joppien, J. Stapelfeldt, J. Wörmer, and T. Möller. CLULU: An experimental setup for luminescence measurements on van der Waals clusters with synchrotron radiation. Review of Scientific Instruments, 64(10):2838–2849, 1993. doi: 10.1063/1.1144371. URL https://doi.org/10.1063/1.1144371.

[116] W. H. Zurek and W. C. Schieve. Multistep clustering and nucleation. The Journal of Physical Chemistry, 84(12):1479–1482, 1980. doi: 10.1021/j100449a010. URL https://doi.org/10.1021/j100449a010.

[117] J. M. Soler, N. García, O. Echt, K. Sattler, and E. Recknagel. Microcluster Growth: Transition from Successive Monomer Addition to Coagulation. Phys. Rev. Lett., 49:1857–1860, Dec 1982. doi: 10.1103/PhysRevLett.49.1857. URL https://link.aps.org/doi/10.1103/PhysRevLett.49.1857.

[118] M. Lewerenz, B. Schilling, and J. Toennies. A new scattering deflection method for determining and selecting the sizes of large liquid clusters of ^{4}He. Chemical Physics Letters, 206(1): 381–387, 1993. ISSN 0009–2614. doi: https://doi.org/10.1016/0009-2614(93)85569-A. URL http://www.sciencedirect.com/science/article/pii/000926149385569A.

[119] J. Farges, M. de Feraudy, B. Raoult, and G. Torchet. Structure and temperature of rare gas clusters in a supersonic expansion. Surface Science, 106(1):95–100, 1981. ISSN 0039–6028. doi: https://doi.org/10.1016/0039-6028(81)90186-2. URL http://www.sciencedirect.com/science/article/pii/0039602881901862.

[120] M. Arbeiter and T. Fennel. Ionization heating in rare-gas clusters under intense xuv laser pulses. Phys. Rev. A, 82:013201, Jul 2010. doi: 10.1103/PhysRevA.82.013201. URL https://link.aps.org/doi/10.1103/PhysRevA.82.013201.

[121] W. C. Wiley and I. H. McLaren. Time-of-Flight Mass Spectrometer with Improved Resolution. Review of Scientific Instruments, 26(12):1150–1157, 1955. doi: 10.1063/1.1715212. URL https://doi.org/10.1063/1.1715212.

[122] SIMION homepage. URL https//simion.com. accessed on October 29th, 2019.

[123] D. A. Dahl, J. E. Delmore, and A. D. Appelhans. SIMION PC/PS2 electrostatic lens design program. Review of Scientific Instruments, 61(1):607–609, 1990. doi: 10.1063/1.1141932. URL https://doi.org/10.1063/1.1141932.

[124] T. Kameshima, S. Ono, T. Kudo, K. Ozaki, Y. Kirihara, K. Kobayashi, Y. Inubushi, M. Yabashi, T. Horigome, a. Holland, K. Holland, D. Burt, H. Murao, and T. Hatsui. Development of an X-ray pixel detector with multi-port charge-coupled device for X-ray free-electron laser experiments. Review of Scientific Instruments, 85(3):033110, 2014. doi: 10.1063/1.4867668. URL https://doi.org/10.1063/1.4867668.

[125] T. Nishiyama, C. Bostedt, K. R. Ferguson, C. Hutchison, K. Nagaya, H. Fukuzawa, K. Motomura, S.-i. Wada, T. Sakai, K. Matsunami, K. Matsuda, T. Tachibana, Y. Ito, W. Xu, S. Mondal, T. Umemoto, C. Miron, C. Nicolas, T. Kameshima, Y. Joti, K. Tono, T. Hatsui, M. Yabashi, and K. Ueda. Multispectroscopic Study of Single Xe Clusters Using XFEL Pulses. Applied Sciences, 9(22), 2019. ISSN 2076-3417. doi: 10.3390/app9224932. URL https://www.mdpi.com/2076-3417/9/22/4932. CC BY 4.0.

[126] A. Savitzky and M. J. E. Golay. Smoothing and Differentiation of Data by Simplified Least Squares Procedures. Analytical Chemistry, 36(8):1627–1639, Jul 1964. ISSN 0003–2700. doi: 10.1021/ac60214a047. URL https://doi.org/10.1021/ac60214a047.

[127] A. Kobayashi, Y. Sekiguchi, Y. Takayama, T. Oroguchi, and M. Nakasako. Dark-field phase retrieval under the constraint of the Friedel symmetry in coherent X-ray diffraction imaging. Opt. Express, 22(23):27892–27909, Nov 2014. doi: 10.1364/OE.22.027892. URL http://www.opticsexpress.org/abstract.cfm?URI=oe-22-23-27892.

[128] T. Mooney, E. Lindroth, P. Indelicato, E. G. Kessler, and R. D. Deslattes. Precision measurements of K and L transitions in xenon: Experiment and theory for the K,L, and M levels. Phys. Rev. A, 45:1531–1543, Feb 1992. doi: 10.1103/PhysRevA.45.1531. URL https://link.aps.org/doi/10.1103/PhysRevA.45.1531.

[129] T. Nishiyama, A. Niozu, C. Bostedt, K. R. Ferguson, Y. Sato, C. Hutchison, K. Nagaya, H. Fukuzawa, K. Motomura, S.-i. Wada, T. Sakai, K. Matsunami, K. Matsuda, T. Tachibana, Y. Ito, W. Xu, S. Mondal, T. Umemoto, C. Nicolas, C. Miron, T. Kameshima, Y. Joti, K. Tono, T. Hatsui, M. Yabashi, and K. Ueda. Refinement for single-nanoparticle structure determination from low-quality single-shot coherent diffraction data. IUCrJ, 7(1):10–17, Jan 2020. doi: 10.1107/S2052252519014222. URL https://doi.org/10.1107/S2052252519014222. CC BY 4.0.

[130] R. Jansen, I. Wysong, S. Gimelshein, M. Zeifman, and U. Buck. Nonequilibrium numerical model of homogeneous condensation in argon and water vapor expansions. The Journal of Chemical Physics, 132(24):244105, 2010. doi: 10.1063/1.3447379. URL https://doi.org/10.1063/1.3447379.

[131] S. M. Vinko, O. Ciricosta, and J. S. Wark. Density functional theory calculations of continuum lowering in strongly coupled plasmas. Nature Communications, 5(1):3533, 2014. ISSN 2041-1723. doi: 10.1038/ncomms4533. URL https://doi.org/10.1038/ncomms4533.

[132] T. Nishiyama, Y. Kumagai, A. Niozu, H. Fukuzawa, K. Motomura, M. Bucher, Y. Ito, T. Takanashi, K. Asa, Y. Sato, D. You, Y. Li, T. Ono, E. Kukk, C. Miron, L. Neagu, C. Callegari, M. Di Fraia, G. Rossi, D. E. Galli, T. Pincelli, A. Colombo, T. Kameshima, Y. Joti, T. Hatsui, S. Owada, T. Katayama, T. Togashi, K. Tono, M. Yabashi, K. Matsuda, C. Bostedt, K. Nagaya, and K. Ueda. Ultrafast Structural Dynamics of Nanoparticles in Intense Laser Fields. Phys. Rev. Lett., 123:123201, Sep 2019. doi: 10.1103/PhysRevLett.123.123201. URL https://link.aps.org/doi/10.1103/PhysRevLett.123.123201.

[133] T. Katayama, S. Nozawa, Y. Umena, S. Lee, T. Togashi, S. Owada, and M. Yabashi. A versatile experimental system for tracking ultrafast chemical reactions with X-ray free-electron lasers. Structural Dynamics, 6(5):054302, 2019. doi: 10.1063/1.5111795. URL https://doi.org/10.1063/1.5111795. CC BY 4.0.

[134] OpenCV homepage. URL https://opencv.org/. accessed on October 29th, 2019.

[135] K. Nakajima, Y. Joti, T. Katayama, S. Owada, T. Togashi, T. Abe, T. Kameshima, K. Okada, T. Sugimoto, M. Yamaga, T. Hatsui, and M. Yabashi. Software for the data analysis of the arrival-timing monitor at SACLA. Journal of Synchrotron Radiation, 25(2):592–603, Mar 2018. doi: 10.1107/S1600577517016654. URL https://doi.org/10.1107/S1600577517016654.

[136] D. R. Sears and H. P. Klug. Density and Expansivity of Solid Xenon. The Journal of Chemical Physics, 37(12):3002–3006, 1962. doi: 10.1063/1.1733133. URL https://doi.org/10.1063/1.1733133.

[137] P. N. Pusey, W. van Megen, P. Bartlett, B. J. Ackerson, J. G. Rarity, and S. M. Underwood. Structure of crystals of hard colloidal spheres. Phys. Rev. Lett., 63:2753–2756,

Dec 1989. doi: 10.1103/PhysRevLett.63.2753. URL https://link.aps.org/doi/10.1103/PhysRevLett.63.2753.

[138] D. D. Hickstein, F. Dollar, J. A. Gaffney, M. E. Foord, G. M. Petrov, B. B. Palm, K. E. Keister, J. L. Ellis, C. Ding, S. B. Libby, J. L. Jimenez, H. C. Kapteyn, M. M. Murnane, and W. Xiong. Observation and Control of Shock Waves in Individual Nanoplasmas. Phys. Rev. Lett., 112:115004, Mar 2014. doi: 10.1103/PhysRevLett.112.115004. URL https://link.aps.org/doi/10.1103/PhysRevLett.112.115004.

[139] H.-K. Chung, M. Chen, W. Morgan, Y. Ralchenko, and R. Lee. FLYCHK: Generalized population kinetics and spectral model for rapid spectroscopic analysis for all elements. High Energy Density Physics, 1(1):3–12, 2005. ISSN 1574-1818. doi: https://doi.org/10.1016/j.hedp.2005.07.001. URL http://www.sciencedirect.com/science/article/pii/S1574181805000029.

[140] P. J. Ho, C. Knight, M. Tegze, G. Faigel, C. Bostedt, and L. Young. Atomistic three-dimensional coherent x-ray imaging of nonbiological systems. Phys. Rev. A, 94:063823, Dec 2016. doi: 10.1103/PhysRevA.94.063823. URL https://link.aps.org/doi/10.1103/PhysRevA.94.063823.

Acknowledgements

My Master's years, Ph.D. years and successive two society years were the most enjoyable and precious years of my life, and I am sure what I learned and obtained in these years and the memories I got with my collaborators and my precious persons are my treasures of life. The path of my Ph.D. was challenging and to some extent in difficulty but gave me the ultimate rewards.

First and foremost, I want to thank Makoto Yao, Kazuhiro Matsuda, and Kiyonobu Naygaya, who have been great mentors through my Bachelor's years to my Ph.D. years. Makoto Yao led me to the study of physics and gave various ideas for the understanding of "what happened in the experiments" with his sophisticated sense. Unfortunately, he was deceased in my second Ph.D. year, but what he left to me is very profound and the base of my thinking on physics. Kazuhiro Matsuda has greatly supported not only my studies but also my life. With his instructive supports, I grew my skills in education and communication with junior colleagues and students. Kiyonobu Nagaya has been a great supporter for me to carry out experiments, presentations, and discussions. His prominent techniques on the apparatus and substantial volume of knowledge have been greatly helpful to experiments and all the discussions. My way of thinking and behavior to the experiments are greatly attributed to those of him.

I also want to thank my advisors and dissertation committee at Kyoto University. Takeaki Araki (my Principle Advisor in my Master's degree), Kenji Ishida (my Principle Advisor in my Ph.D. degree) and Hikaru Kitamura (my Academic Advisor) have all been supportive and open throughout my studies. Koichiro Tanaka, Shin-ichi Sasa, Jun Yamamoto, and Yoichi Takanishi have been great dissertation committee members and given instructive and suggestive opinions on my studies.

During my Master's and Ph.D. years, I had an enjoyable and educative time with my colleagues at Kyoto University. They have been friendly subjected to listening to many practices and private talks I have given. Tsukasa Sakai has been a good senior colleagues and helped me obtain the fundamental ability to operate a cluster jet source and analyze the ion TOF spectra. Kenji Matsunami has also been my good senior colleague and helped me obtain the fundamental ability to construct scripts for analysis. Christopher Hutchison, who was moved to Imperial College London, supported the experiments with his excellent ability to construct a GUI software. He also inspired

me to learn one of the programming language Python. Hagiya Toru has been a good friend I think and collaborated in the open labs and other laboratory events greatly. Kazuki Asa and Yuhiro Sato have helped me prepare and carry out the experiments and sometimes given me ideas that I have not conceived. I truly thank Akinobu Niozu, who has not only helped the experiments but also the compilation and analysis of the experimental results. I had an excellent time with them during my Master's and Ph.D. days.

My collaborators at Tohoku University are of importance for the experiments and I thank them very much. Kiyoshi Ueda has been a great coordinator of the project related to the experiments, and he has given me excellent opportunities to join experiments using FELs and synchrotrons in Japan and in Italy. These opportunities enabled me to collaborate with scientists and staff having prominent techniques. I want to thank him for giving the precious time of collaboration. Hironobu Fukuzawa has been a great collaborator and offered his technical ability, especially of the ion detector, to lead the experiments to the success. I want to thank him for his support in the experiments, proofreading my manuscript, and an enjoyable journey in Toledo in a conference ICPEAC XXIX. Koji Motomura has offered his prominent knowledge and techniques in computation and signal processing. I want to thank him for his collaboration and his kind supports and lectures. Grow in my computational ability is owing to him. Yoshiaki Kumagai has been a good senior colleague and offered his knowledge, way of thinking and physical strength for the experiments. He has been also a great mood maker and I had a good time in communicating with him. Yuta Ito has offered his prominent ability to operating the optical laser system. The success of the experiments was greatly owing to him. I also want to thank Tetsuya Tachibana, Daehyun You, Subhenudu Mondal, Weiquing Xu, Yiwen Li, Taishi Ono, and other colleagues, who have offered their powerful supports to lead the experiments to success.

I cannot avoid giving many thanks to Tsukasa Takanashi, one of the great collaborators at Tohoku University. He has been a good colleague and shown his knowledge and ability to What I thank most is his friendly communication; he has always tried to make smooth communication among the collaborators, which surely has removed stubborn mood in the group. He has also been tolerantly subjected to many practices and private talks I have given and often given nice, educative and meaningful talks and discussions, which led to the release of my stress in my Master's and Ph.D. days. I honestly say that he is one of my precious friends, and I always have a good time talking and collaborating with him.

I also want to thank my collaborators at Hiroshima University. Shin-ichi Wada has offered his ability to operating the sample sources in the experiments. He has also been a senior in life; he has kindly accepted consultation from me about my way of living. Takayuki Umemoto has offered supports to the experiments and friendly communication. These were necessary for the smooth progression of the experiments.

The experiments and my publications would have not been successful without my collaborators from SLAC national laboratory and Argonne National Laboratory. Christoph Bostedt, who currently works for Paul Scherrer Institute, has been a great professor as well as a great coordinator of the experiments. I am sure that the experiments would not have been successful without his profound thinking, prominent techniques, and experience. I truly thank him for his kind offer of the above abilities and supports. Improvement of my language editing is surely owing to his instructive supports throughout my publications. I want to thank Ken Ferguson and Max Bucher, who have shown their sophisticated experimental techniques. I had an enjoyable time in the experiments with their friendly communication.

My collaborators from other foreign institutes have given their incredibly great supports to my experimental studies. I would love to thank them. From Extreme Light Infrastructure - Nuclear Physics, Catalin Miron has offered his supports to lead the experiments and to language editing of my publication. I truly thank him for his kind and instructive supports. Liviu Neagu has offered technical supports on the optical laser system. From Synchrotron SOLEIL, Christophe Nicolas has offered technical supports on the detector. These supports are essential to the achievement of the experiments and publications. From Turku University, Edwin Kukk has been a good collaborator and offered his prominent ability to analyze the experimental data during the experiments. His supports have made the discussion smooth during the experiments. From Elettra-Sincrotone Trieste, Carlo Callegari has offered technical supports and a very meaningful discussion in my first publication. Michele Di Fraia has offered great supports in the preparation of the experiments. From Universitá degli Milano, Giorgio Rossi has offered suggestive supports on discussion and language editing for my first publication. Davide Galli, Tommaso Pincelli and Alessandro Colombo have great supports in the preparation of the experiments. I thank them very much again for their kind and friendly supports.

The experiments that led to this dissertation were performed in the experimental hutches 2 and 3 on beamline 3 at SACLA, but support from the RIKEN and JASRI staff was crucial. In particular, I was indebted to Makina Yabashi, Kensuke Tono, and Tadashi Togashi for their help conducting the experiments, Yasumasa Joti and Takaki Hatsui for their help on data processing and networks of the HPC system, Takashi Kameshima for his help on the MPCCD detectors, Tetsuo Katayama for his help on the arrival-timing monitor for the time-resolved experiments, and Shigeki Owada for his support as a main supporter on the experiments and on the preparation of the optical laser system. While not directly involved in the experiments presented in this work, the rest of RIKEN and JASRI staff have made the many beamtimes I have participated in exciting and joyful.

I want to thank my boss and colleagues at Systemroad Co., Ltd. They have offered me flexible schedules to study for my Ph.D.

Lastly, I thank my family: my mother and father, younger brothers. I want to thank my parents for raising me and supporting my studies with their love. I want to thank my younger brothers, Takayuki and Mitsuyuki, who have always been the friends I needed throughout my life. I truly thank my precious, Rika Hiraki. She has been always next to me and encouraged me to keep studying for my Ph.D. I truly give many thanks to her for her irreplaceable honor, love, and enthusiasm throughout my Ph.D. days.

Toshiyuki Nishiyama

Kyoto University
March 2020